

Structure and dynamics of a 1,4-Polybutadiene melt in confinement: A Molecular Dynamics study

Dissertation

zur Erlangung des Doktorgrades der Naturwissenschaften
(Dr. rer. nat.)

der

Naturwissenschaftlichen Fakultät II
Chemie, Physik und Mathematik

der Martin-Luther-Universität Halle-Wittenberg

vorgelegt von

Frau M. Sc. Lama Tannoury

Gutachter: Prof. Dr. Wolfgang Paul
Prof. Dr. Kay Saalwächter
Prof. Dr. Alexey Lyulin

Datum der öffentlichen Verteidigung: 14.12.2023

Abstract

The study of the structure and dynamics of polymers confined by solid surfaces, enhances our knowledge about the properties of composite materials. The topic has been a desired area of study given the development of its applications. In such systems, the macromolecules are responsible for the general performance of the whole system. Therefore, understanding the effect of the confinement on the structure and dynamics of polymers is crucial for the advancement of the field. It has been shown that conformations and dynamics of polymer melts confined to thin films and flat surfaces as well as cylindrical pores are altered in comparison with the bulk. The change in properties depends on several factors including but not limited to the geometry of confinement. In our research, we study the effects of both the nanoscopic confinement and curvature on the dynamics and properties of a chemically realistic united atom model of a 1,4-Polybutadiene (PBD) melt using Molecular Dynamics (MD) simulations. Therefore, we divide our work into two systems: one with a PBD melt confined in a cylindrical nanopore and the other with a PBD melt surrounding a cylindrical nanorod. In both systems, the effects induced by the confinement on the melt's structure and dynamics on several scales are examined and compared.

Zusammenfassung

Die Untersuchung der Struktur und Dynamik von Polymeren, die von festen Oberflächen eingeschlossen sind, erweitert unser Wissen über die Eigenschaften von Verbundwerkstoffen. Das Thema ist ein wichtiger Untersuchungsgegenstand angesichts des weitreichenden Anwendungsfeldes. In solchen Systemen sind die Makromoleküle für die allgemeinen Eigenschaften des Gesamtsystems verantwortlich. Ein Verständnis der Auswirkungen von Einschlüssen auf die Struktur und die Dynamik von Polymeren ist von entscheidender Bedeutung für den Fortschritt auf diesem Gebiet. Es wurde gezeigt, dass die Konformationen und die Dynamik von Polymerschmelzen, die in dünnen Filmen und flachen Oberflächen sowie in zylindrischen Poren eingeschlossen sind, sich im Vergleich zur Masse verändern. Die Veränderung der Eigenschaften hängt von verschiedenen Faktoren ab, unter anderem von der Geometrie des Einschlusses. In unserer Forschungsarbeit untersuchen wir die Auswirkungen sowohl des nanoskopischen Einschlusses als auch der Krümmung auf die Dynamik und die Eigenschaften eines chemisch realistischen united atom models einer 1,4-Polybutadien (PBD)-Schmelze mit Hilfe von Molekulardynamiksimulationen (MD). Daher unterteilen wir unsere Arbeit in zwei Systeme: eines mit einer PBD-Schmelze, die in einer zylindrischen Pore eingeschlossen ist, und das andere mit einer PBD-Schmelze, die einen zylindrischen Nanostab umgibt. In beiden Systemen werden die Auswirkungen des Einschlusses auf die Struktur und Dynamik der Schmelze auf verschiedenen Skalen untersucht und verglichen.

Contents

1	Introduction	1
1.1	Polymers under confinement	2
1.2	Polybutadiene and Alumina	6
1.3	Structure of the dissertation	8
2	Molecular Dynamics Simulations	9
2.1	Newton’s Equation of Motion	9
2.2	Integration scheme	10
2.2.1	Leapfrog Algorithm	11
2.3	The Nosé-Hoover thermostat	11
3	Model, Preparation and Simulations	14
3.1	Levels of modeling	14
3.2	Force field	16
3.2.1	Bonded interactions	17
3.2.2	Non-bonded interactions	19
3.2.3	Validation of the Model: MD simulations vs. Experiments .	20
3.3	Preparations and simulations	21
3.3.1	Alumina	21
3.3.2	PBD in a nano-pore and the resist cylinder	21
	Resist cylinder	23
	Alumina nanopore	25
	Simulations	25
3.3.3	PBD surrounding a nanorod	26
	Alumina nanorod	26
	PBD preparation	27
	Simulations	28

4	Polybutadiene confined in an alumina nanopore	29
4.1	Structure across the nanopore	30
4.1.1	Density layering	30
4.1.2	Double bond orientational ordering	33
4.1.3	Chain ordering and orientation	34
	Gyration Tensor	34
4.1.4	Nematic Order	39
4.2	Dynamics across the nanopore	41
4.2.1	Mean squared displacement (MSD)	42
4.2.2	Adsorption Autocorrelation Function	49
4.2.3	Incoherent Neutron Scattering Function	51
	Case 1: \mathbf{q} along $\hat{\mathbf{e}}_z$	53
	Case 2: \mathbf{q} perpendicular to $\hat{\mathbf{e}}_z$	54
4.2.4	Segmental Orientational Correlation Function	64
5	Polybutadiene surrounding an alumina nanorod	71
5.1	Structure of the melt	72
5.1.1	Density layering	73
5.1.2	Double bond orientational ordering	74
5.1.3	Chain ordering and orientation	76
	Gyration Tensor	76
5.1.4	Nematic Order	80
5.2	Dynamics of the melt	81
5.2.1	Mean Squared Displacement	82
5.2.2	Incoherent Neutron Scattering Function	86
5.2.3	Segmental Orientational Correlation Function	93
6	Conclusion and Outlook	98
A	GROMACS Topology File	I
B	Supplementary Figures - PBD inside an alumina nanopore	VIII
C	Supplementary Figures - PBD surrounding an alumina nanorod	XIII
	Bibliography	XIX
	Acknowledgments	XL

List of Abbreviations

PBD	Polybutadiene
MD	Molecular Dynamics
PNC	Polymer NanoComposites
NP	NanoParticles
R_g	Radius of gyration
T_g	Glass transition temperature
CG	Coarse Grained
AA	All Atom
UA	United Atom
GROMACS	GRONingen MACHine for Chemical Simulations
LJ	Lennard-Jones
RIS	Rotational Isomeric State
RC	Resist Cylinder
RB	Repulsive Beads
COM	Center of Mass
MSD	Mean Square Displacement
INSF	Incoherent Neutron Scattering Function
ACF	AutoCorrelation Function
OACF	Orientalional AutoCorrelation Function

Chapter 1

Introduction

Polymers have become the raw materials for essential products that we utilize every day. Synthetic and natural polymers play a major role in the facilitation of our daily lives and in the case of biological polymers, are responsible for life itself. Their impact encompasses several aspects of human life such as medication, clothing, electronics, packaging, etc. All the benefits of polymer materials would not have been possible without the scientists who have worked on their synthesis and investigated their properties. The use and synthesis of polymers is dated prior to 20th century; however, their nature was not fully understood. In 1920, Hermann Staudinger was the first to identify a polymer as a long chain made up of repeating units held together by covalent bonds. Later in the 1950s, as Staudinger's work started to gain acceptance, Karl Ziegler and Giulio Natta discovered a new process for polymerisation that enhanced the synthesis of several plastics such as polyethylene. Afterwards came the work of several scientists including Paul J. Flory and Pierre-Gilles de Gennes who were responsible for developing the basics of polymer theory.

These breakthroughs lead to the commercialization of polymers and polymeric materials and their extensive use in our daily lives. Scientists then started producing composite materials by mixing polymers with other materials. Polymer nanocomposites (PNC) or nano-filled polymer composites, an example of such new materials, are made up of nano-sized particles incorporated into a polymeric matrix. The addition of the nanoparticles (NPs) results in an improvement of the properties of the new material and has a wide range of applications such as high-tech electronics, biotechnology and the automotive industry. As the fabrication of nanomaterials advanced and varied so did the circumstances in which they were studied such as the case of strongly confined states. The confinement

also alters the properties of the confined material, broadening their applications and drawing a lot of research interest to the subject [1–11]. Yet more research is needed to strengthen our understanding of the topic. The most common types of confinement are thin films, nanostructures, nanofillers, and nanopores. Figure 1.1 shows some examples of these types of confinements.

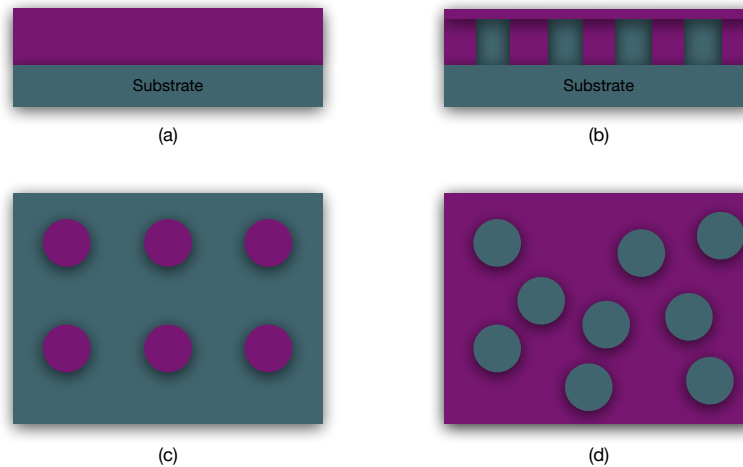


Figure 1.1: Schematic of different types of confinement: **(a)** supported thin films, **(b)** nanostructure, **(c)** nanopores and **(d)** nanoparticles.

1.1 Polymers under confinement

The study of the structure and dynamics of polymers confined by solid surfaces, e.g. [12–17], enhances our knowledge about the properties of composite materials. The topic has been a desired area of study given the development of its applications. In such systems, the macromolecules are responsible for the general performance of the whole system. Therefore, understanding the effect of the confinement on the structure and dynamics of polymers is crucial for the advancement of the field.

It has been shown, both by experimental and computational studies, that conformations and dynamics of polymers in confinement are altered in comparison with the bulk. The change in properties depends on several factors including but not limited to the geometry and dimensionality of the confinement as well as the

type of interaction between the melt and its confining environment. The degree by which these factors affect the system is still under investigation and computer simulations can assist us in discovering them and in demonstrating in detail and from a microscopic view specific quantities that are related to the structure, dynamics and relaxation of the polymer. Studies using simulations have addressed the effects on the polymer (entangled and unentangled) structure and dynamics induced by thin films/flat wall confinement e.g. [18–26], and by nanoparticles e.g. [27–33]. Fewer studies have addressed polymer melts under cylindrical confinement. However, experimentally, cylindrical confinement has been of growing interest since it became possible to manufacture nanopores of size of 10s of nm in diameter into which polymers can be infiltrated. These systems offer an unprecedented control over the confinement geometry. Different techniques have been used to examine the effects of pore confinement at various time and length scales. For example, the structure and dynamics were studied using dielectric spectroscopy [12], nuclear magnetic resonance (NMR) [34, 35] and neutron scattering experiments (NSE) [13, 36–42].

Understanding the change in the structure of confined polymer melts provides a comprehensive view of how the dynamics of the system are altered. One of the most well known structural effects of confinement, seen in experiments and simulations, is the close packing and density layering at the wall-melt interface [14, 15, 20, 22, 24, 39, 43–47]. This has been observed in thin film and cylindrical geometries and for both the monomer and center-of-mass densities with the former having a length scale of $\sim \sigma$, where σ is the size of the monomer and the width of the chain. For repulsive surfaces [20, 48] the effect is weak but the stratified structure could still be observed. The question of chain and segmental orientation has also been addressed in simulations [14, 20–23] as well as experiments on polymer chains confined in cylindrical nanochannels [37, 49]. All the research points out that there exists a monomer as well as a chain orientation parallel to the confining walls. Studies tackling the chain conformation of confined melts [20–23, 37, 49–51] show that the component of the radius of gyration R_g perpendicular to the confining surface (wall or cylinder) is significantly reduced compared to its bulk value while the opposite applies to the component parallel to the confining surface.

For both, slit and cylindrical confinement, it has been established by simulations that chains with their center of mass closer to the wall than the typical chain size (measured either by the gyration radius R_g or the end-to-end vector R_e)

get oriented with the longest axis of their gyration ellipsoid parallel to the wall. This can be understood by applying Silberberg's reflection hypothesis [52] for unperturbed random walk chains [53]. As the confinement size becomes smaller than the extension of the chains, $D < R_e$, deviations from chain ideality are enhanced [54] leading eventually to the segregation of chains predicted a long time ago by Brochard and De Gennes [55]. For entangled systems, the orientation of the long axis of the gyration ellipsoid along the pore axis for cylindrical confinement reduces the entanglement density for motion along the pore [53]. This results in a speedup of the motion and diffusion of chains which has been found experimentally [34,36,41] and in simulations [39,53].

Many of the confined polymer applications depend on the polymer-surface interaction and the dynamics occurring there. The structure of the confinement and the polymer-surface interaction can affect the dynamics of the polymer melt in several ways [56,57]. Concerning repulsive or neutral polymer-surface interactions, experiments by Krutyeva *et al.* [58] used time of flight spectroscopy (TOF) and backscattering (BS) techniques to reveal that the segmental dynamics are not affected and that the relaxation times of the confined polymer are identical to those in the bulk [59] of the same polymer. On the other hand, in simulations [60,61] on repulsive interactions it was observed that the polymer in the layer close to the surface exhibits faster segmental motion compared to the interior of the melt. The case of attractive polymer-surface interactions shows a different effect on the polymer dynamics. Dielectric spectroscopy measurements [62] address a slowing down of the segmental dynamics at the surface and mention that the inherent length scale found in the experiments are relevant for glassy dynamics. NSE [16] of Poly(ethylene oxide) (PEO) in anodic aluminum oxide (AAO) membranes show that for attractive surfaces, the dynamics of polymer segments close to the confining wall slow down in the direction perpendicular to the surface. No such observation was made for the direction parallel to the wall. The NSE also indicate that there is no glassy layer at the surface. Similarly, NSE measurements on PEO in nanoporous silica [38,63] show that the chains close to the pore walls are adsorbed and display significantly slower dynamics than in the center where the free chains have bulk-like dynamics. The adsorbed layer was found to be approximately the size of the radius of gyration (R_g) of the chains whose centers-of-mass are immobile. Simulations [43,44] on the segmental dynamics of a polybutadiene melt confined between graphite walls has also shown a strong slowing down of the α -relaxation at the polymer-surface layer.

NMR experiments on polybutadiene in AAO nanopores [42,49] found two components in the model: a bulk-like core and a surface region with a thickness of a few nanometers.

As mentioned before, one type of confinement is induced by spherical NPs/nanofillers. NP filled polymers was primarily an interest in the car tires industry since NPs added to rubber increase strength, traction and wear resistance [64]. Similar properties are also present in other applications making polymer nanocomposites desirable in other fields as well and making them good candidates for further research. So far, we have focused mostly on thin film and cylindrical confinement; therefore, an overview of studies on spherical NP follows. A study by Starr et al. of a polymer melt with a nanoscopic particle displays results similar to ultra thin films [65,66] and shows comparable results for 1D and 2D confinements. Even though this system does not fully depict the confinement, interaction or the geometries induced by several NPs, it presents the effect near the surface. For an attractive polymer-particle interaction, the density layering is present along with an elongation of the polymer and an orientation along the particle surface. The study recovers the same effects for a particle with double the initial attraction allowing Starr et al. to argue that the change in the chain structure and the shape of the polymer is mainly influenced by the geometric constraints of chain packing close to the surface. Similar simulations on polymers around a NP [67] also show a density layering around the NP and that the dynamics of the monomers in the layers close to the surface is slowed down by the crowded environment as well as the strength of the attraction of the NP that results in the adsorption of monomers to the surface [68]. As the system becomes more resembling of nanocomposites and more NPs are added [69–72], it also becomes difficult to identify the origins of the effects on the chains; however, some conclusions could be made. R_g of the chains increases for chains in the vicinity of the NP and in the vicinity of the NP surface the chains tend to be elongated and align their longest axis along the surface as seen in previous studies. The change in chain size is also dependent on the size of the particles relative to the bulk R_g of the chain. Dynamic non-Gaussianity is observed [71] where the dynamics of the confined polymer is found to be slower than that of the bulk-like region. With moving NPs several variables must be taken into account such as the NP-polymer interaction, NP-NP interaction, the varying distance between the NP and others. Experiments using neutron scattering, x-ray scattering and other methods [33,73,74] study the effect of the dispersed NPs on the chain dimensions and mainly the

effect of the ratio of polymer size (R_g) to NP size (R_{NP}) on the swelling of the chains. While some experiments argue that this ratio does not control the size of the confined chains, others state that when $R_g > R_{NP}$ the NPs behave like a good solvent where dispersion and swelling of the chains occur. Experimental studies concerning the dynamics of polymers with NPs also give varying results. There is a consensus that the layer at the interface is slower than the bulk and dependent on filler size and concentration [75–77]; however, some studies [78] report that the interfacial layer is not a "dead layer" while others [32,79] discuss an immobilized polymer layer.

An ample amount of the literature also tackles the effect induced by the confinement on the glass transition temperature T_g of the melt e.g. [6]. Experimental studies with varying approaches have tried to determine T_g in thin films for different thicknesses [15,80–86]. The results on the glass transition vary and are sometimes incompatible. T_g of a confined melt differs from that of the bulk; however, the effects of interfaces, the confining substrate and the interaction of the polymer with the substrate have been proven difficult to separate in experimental measurements. Computer simulations [87,88] on supported and free standing polymer films document that T_g is reduced when compared to its value in the bulk and decreases with decreasing thickness of the film. Simulations on the effect of the confinement on T_g in polystyrene films [14] have also tried calculating T_g for different layers across the melt based on the density layering across the confinement. Their results suggest that the change in T_g with film thickness is not related to the average density or the strength of the substrate's attraction. Understanding the effect of the surface and geometry of confinement on the glass transition would help with improving the mechanical properties of nanocomposites and other applications.

1.2 Polybutadiene and Alumina

In 1910, the chemist Sergei Vasilyevich Lebedev [89] was the first to polymerize butadiene and convert 1,3-butadiene to a rubberlike product. Later on he was able to develop a method to produce polybutadiene PBD which became essential in the production of synthetic rubbers. Based on Lebedev's work and with the help of later developments and improvements, polybutadiene became the leading synthetic general-purpose alternative to natural rubber.

PBD, as mentioned before, is produced through the polymerization of 1,3-butadiene and when the latter enters the growing polymer chain, it can yield three different structural isomers: *cis*-1,4, *trans*-1,4 and vinyl-1,2 as seen in Figure 1.2.

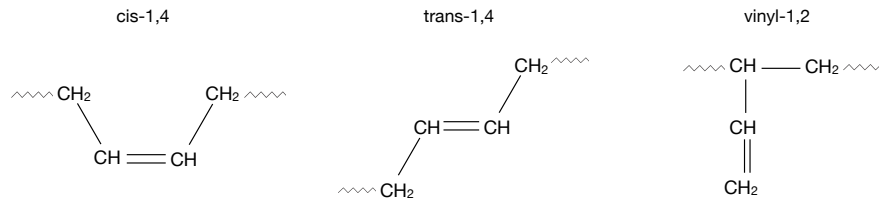


Figure 1.2: Structural isomers as a result of the polymerization of 1,3-butadiene.

The *cis* and *trans* isomers have similar glass transition temperatures (T_g) [90], where the *cis*-1,4 T_g ranges from 167K to 178K and the *trans*-1,4 T_g ranges from 166K to 171K. On the other hand the 1,2-vinyl has a much higher T_g of around 245 – 269K making it unsuitable for elastomer applications. The two former isomers have different properties and applications and a mixture of both creates a new polymer with different properties as well. For example, *cis*-1,4-PBD has high tensile strength and can be compounded with fillers and other polymers and is usually used in tires, belts, gloves and others. *Trans*-1,4-PBD has good low-temperature properties, good adhesion to metals and abrasion resistance and can be used for protective coatings, seals and other applications. The most commonly used types of PBD are high-*cis* PBD with $\sim 95\%$ *cis* content and low-*cis* PBD with around 38% *cis*, 51% *trans* and 11% vinyl content.

In some cases PBD is usually combined with other elastomers and sometimes with NPs/ nanofillers leading to polymer nanocomposites with appealing properties. Despite the latter, a lot remains unknown regarding PNCs. Several studies, experimental and computational, have tackled the confinement of PBD in slab or thin film geometry. The latter gives us more information on polymer melts in 1D confinement yet it does not bring us closer to comprehending the effect of curvature and confinement combined in PNCs and particularly those with PBD. Consequently, the role of experiments on PBD in cylindrical confinement and PNCs has been essential to detect the effects on polymers yet simulations are still needed to predict and provide explanations of structural and dynamical properties observed in experiments. The simulations of NP infiltrating polymer melts in the literature are primarily those of coarse grained bead-spring models. A chem-

ically realistic model of such composites would have length and times scales that would exceed those of realistic molecular dynamics simulations; therefore, an attempt to model realistic filler networks would not be the correct approach to answer our questions. Since we would like to keep the nano-size of the filler and the effects of surface curvatures on the structure and dynamics of the polymer melt, we simulate two model systems: one with a PBD melt infiltrated in an alumina pore of 10 nm diameter size and another of a PBD melt surrounding an alumina cylinder. The two systems together would allow us to study the different types of curvatures as well as the confinement enforced by the NPs on the polymer melt. The former system has also been experimentally investigated [91, 92] allowing for a comparison and validation of our system and simulations to the experimental data.

The properties of PNC materials depend on many aspects of their composition and structure which are barely or not at all controllable. To gain a fundamental understanding of their properties one would then need well controlled systems which is why we perform our simulations with alumina. The invention of microporous alumina [93] with pore diameters in order of tens of nanometers was a big step forward to generate a controlled confined environment.

A spatially resolved analysis of the structural properties of the melt in confinement is very hard to achieve experimentally but it underlies the effects observed in dynamic experiments. Consequently, the need for polymer simulations arises.

1.3 Structure of the dissertation

The dissertation is structured as follows. The second chapter goes into the details of Molecular Dynamics (MD) simulations while the third chapter describes the Polybutadiene model and the preparation steps taken to create the systems analyzed. The discussion of the results is divided into two chapters, the fourth and fifth, where the first one is dedicated to the PBD melt in alumina pores and the second to the PBD melt surrounding an alumina cylinder. Chapter 4 and Chapter 5 are in turn divided into two parts that go into the details of the structure (part 1) and the dynamics (part 2) of the systems. The final chapter is dedicated to the discussion and summary of the findings as well as a short outlook to future projects.

Chapter 2

Molecular Dynamics Simulations

Computer simulations are a powerful numerical technique for modeling many-body systems, from gases and liquids to polymers. They are carried out to further understand the structural properties of molecules as well as how they interact with each other. More importantly, simulations accompany and add to the knowledge acquired from experiments and sometimes allow us to understand certain things that cannot be observed otherwise. They act as a link between theory and experiments and can be carried out using a model predicted by theory. In turn, the computational model is evaluated by comparing to experiments.

The main branches of simulation techniques are Molecular Dynamics (MD) and Monte Carlo (MC) with a mixture of techniques combining features from both. MD simulations present us with the evolution of the system under study by generating the configurations along its trajectory. This allows us to study dynamics and time-dependent properties such as mean squared displacements, dynamic structure factors, diffusion coefficients and others. Starting with a few atoms for the first simulations of proteins [94] in the 70s, MD simulations have improved immensely to include complex systems with hundreds of thousands of atoms. This improvement can be attributed to the continuous development and enhancement of high performance computing (HPC) as well as the simple nature of the basic MD algorithm.

2.1 Newton's Equation of Motion

The backbone of MD simulations is the numerical integration of Newton's equation of motion. By calculating the force acting on each atom in the system, we

can subsequently calculate their respective velocities and accelerations. Thus integrating the equation of motion results in a trajectory of the system which conveys information about the positions, velocities and accelerations of the atoms in time. The state of the system can be predicted at any time given the atoms' positions and velocities. It is essential; however, to define the initial positions and velocities. In addition, static and dynamic properties can be calculated using these trajectories. For a system made of N atoms interacting via a potential U , the classical equation of motion can be written in a simplified form as follows,

$$\mathbf{f}_i = -\frac{\partial U}{\partial \mathbf{r}_i} \quad m_i \frac{d^2 \mathbf{r}_i}{dt^2} = \mathbf{f}_i, \quad (2.1)$$

where \mathbf{r} and \mathbf{f} are the position and force vectors respectively and m is the mass.

2.2 Integration scheme

To solve the second order differential equation in eq.(2.1), several numerical schemes have been developed. The most widely used scheme is known as the Verlet method, which is simple and time reversible, and encompasses the Velocity Verlet as well as the Leapfrog algorithms. The main Verlet method starts by using a Taylor expansion of the position vector $\mathbf{r}(t)$ at $(t - \delta t)$ and $(t + \delta t)$ as follows,

$$\mathbf{r}(t + \delta t) = \mathbf{r}(t) + \frac{d\mathbf{r}(t)}{dt}\delta t + \frac{1}{2} \frac{d^2\mathbf{r}(t)}{dt^2}\delta t^2 + \frac{1}{3!} \frac{d^3\mathbf{r}(t)}{dt^3}\delta t^3 + \mathcal{O}(\delta t^4) \quad (2.2)$$

$$\mathbf{r}(t - \delta t) = \mathbf{r}(t) - \frac{d\mathbf{r}(t)}{dt}\delta t + \frac{1}{2} \frac{d^2\mathbf{r}(t)}{dt^2}\delta t^2 - \frac{1}{3!} \frac{d^3\mathbf{r}(t)}{dt^3}\delta t^3 + \mathcal{O}(\delta t^4). \quad (2.3)$$

Adding eq.(2.2) and eq.(2.3) and simplifying results in an expression of the position at time $t + \delta t$ not involving the velocity of the atom results in the following expression,

$$\mathbf{r}(t + \delta t) = 2\mathbf{r}(t) - \mathbf{r}(t - \delta t) + \frac{d^2\mathbf{r}(t)}{dt^2}\delta t^2 + \mathcal{O}(\delta t^4). \quad (2.4)$$

In the Verlet method, velocities are not solved for explicitly; however, they can be calculated if we take eq.(2.2) - (2.3),

$$\mathbf{v}(t) = \frac{\mathbf{r}(t + \delta t) - \mathbf{r}(t - \delta t)}{2\delta t} + \mathcal{O}(\delta t^2). \quad (2.5)$$

The Velocity Verlet and the Leapfrog algorithms are very similar. In our simulations, the Leapfrog method is used; therefore, the next section will focus mainly on it.

2.2.1 Leapfrog Algorithm

A good algorithm has to conserve energy, provide accuracy for large times steps δt and as mentioned before, be time reversible. The Leap-frog algorithm is one that fulfills these categories and its integration cycle starts with using a Taylor expansion for the velocity about half steps of t as follow:

$$\mathbf{v}(t + \frac{1}{2}\delta t) = \mathbf{v}(t) + \frac{1}{2}\mathbf{a}(t)\delta t \quad (2.6)$$

$$\mathbf{v}(t - \frac{1}{2}\delta t) = \mathbf{v}(t) - \frac{1}{2}\mathbf{a}(t)\delta t \quad (2.7)$$

and the combination of these two expressions is,

$$\mathbf{v}(t + \frac{1}{2}\delta t) = \mathbf{v}(t - \frac{1}{2}\delta t) + \mathbf{a}(t)\delta t. \quad (2.8)$$

Rewriting eq.(2.4) in terms of (2.6) we obtain a term to update the positions,

$$\mathbf{r}(t + \delta t) = \mathbf{r}(t) + \mathbf{v}(t + \frac{1}{2}\delta t)\delta t. \quad (2.9)$$

According to this scheme, one would initially need $\mathbf{r}(t)$, $\mathbf{a}(t)$ and $\mathbf{v}(t - \frac{1}{2}\delta t)$. One first computes the half step ($t + \frac{1}{2}\delta t$) velocity and then updates the new positions. The velocities and positions are not calculated for the same moment in time thus one is constantly leaping over the other by half a step.

2.3 The Nosé-Hoover thermostat

Our simulations are conducted at constant temperature in a canonical ensemble (NVT); therefore, to modulate the temperature in the system, a thermostat is

needed. The idea behind a thermostat is to ensure that the average temperature of the system is the desired and allocated one. One of the popular thermostats used and the one we utilize in our simulations is the Nosé-Hoover [95,96] thermostat. The latter introduces a thermal reservoir and fictitious friction term ζ that is time dependent to the equations of motion. The reservoir is coupled to our system such that they can exchange energy and has a mass defined as Q . Q essentially determines the intensity of the coupling. A small value of Q results in strong coupling and vice versa. Q can also be observed as a quantity that determines the time scale of fluctuations of the temperature of the system. It is important to note that the energy is now conserved for the system and the heat bath combined. The updated equations of motion are:

$$m_i \frac{d^2 \mathbf{r}_i}{dt^2} = \mathbf{f}_i - \zeta m_i \mathbf{v}_i \quad (2.10)$$

$$Q \frac{d\zeta}{dt} = \sum m_i \frac{\mathbf{v}_i^2}{2} - N_{df} k_B T \quad (2.11)$$

where N_{df} is the total number of degrees of freedom, T is the temperature and k_B is the Boltzmann constant. The Nosé-Hoover equations of motion can be then implemented in the Leap-frog algorithm explained previously.

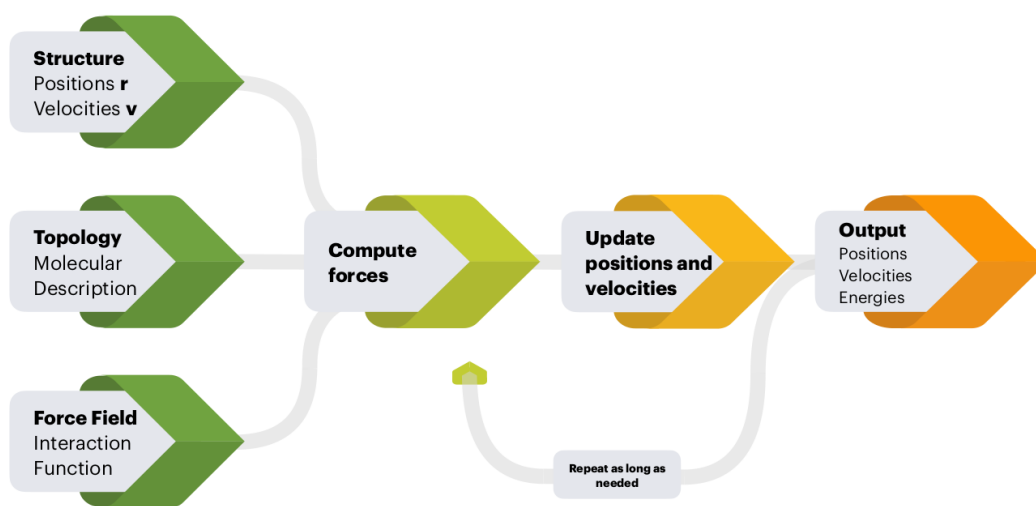


Figure 2.1: Schematic of an MD simulation program process.

Finally, a typical MD simulation program works according to the schematic in Figure (2.1) . Details on the topology and the force field specific to our model will follow in Chapter 3. Starting with the initial structure and model dependent topology and force fields (the latter two will be further discussed for our model in the following chapter), the software calculates the forces and subsequently the updated positions and velocities by solving the equation of motion. Afterwards, any necessary boundary conditions, temperature or pressure control are applied. This process is repeated as long as needed with an output of the needed physical quantities.

Chapter 3

Model, Preparation and Simulations

Computer simulations, and in this case Molecular Dynamics (MD) simulations, are merely a means by which an algorithm provides a set of rules to conduct calculations pertaining to a specific model. The model then is a major constituent in the success of the simulations and contains all the information needed to represent and reproduce the system under study. In this work a model of 1,4-Polybutadiene (PBD), developed by Smith and Paul in 1998 [97–100], was used in the MD simulations. The latter were introduced in chapter 2. This chapter will focus on the model, starting with the different types of polymer modeling and then going into details of our PBD model and its corresponding force field. This is followed by a brief overview on the comparison of previously conducted MD simulations on a PBD melt with experiments. The second part of the chapter describes the steps taken to prepare the PBD melt and the alumina for the simulations of our two systems.

3.1 Levels of modeling

There are several levels of detail for modeling a polymer chain while preserving its chemical properties. These levels differ mainly by how detailed they model a specific system and by how efficient they are in terms of computational resources. A comparison of the modeling methods for poly(ethylene oxide) can be found in [101]. The first, is the coarse-grained (CG) model. The main idea behind the coarse grained model is to incorporate several atoms into one single CG bead. That could occur at different granularity levels, for example, a CG model could group a few atoms, molecules, and sometimes whole chains into one bead. The

degree of graining varies according to the goal of the simulations. When the study requires representing specific polymer chemistries, a fine grained model is more appropriate. On the other hand, a coarser model is more efficient when the aim is to study universal properties such as scaling laws. In the CG model, the degrees of freedom are decreased which helps with achieving long simulation times; however, this is met at the expense of molecular detail. To capture the full molecular detail of a system, an all atom (AA) model is needed where all atoms, including hydrogen, are treated as separate beads. Having an "accurate" atomic-level description of our system is not always necessary; however, an AA would be a good option if the problem at hand requires an understanding of, for example, local monomer-level interactions or methyl group rotations. Given that level of detail, the AA model is not efficient enough to handle large systems and large simulation timescales. The third model is known as a united atom (UA) model and it reduces the computation time compared to the AA model. A united atom is a particle that groups the carbon atoms with their respective hydrogen atoms when the latter need not be explicitly represented. Force fields for AA and UA models are quite similar and are usually obtained from ab initio quantum chemistry calculations and/or tuning the parameters to known experimental quantities.

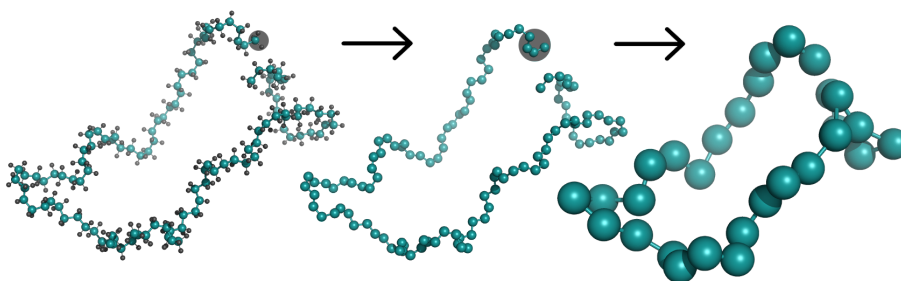


Figure 3.1: Schematic of the different levels of modeling. The left most chain is a representation of an all atom (AA) model. The chain in the center is a united atom (UA) model with each bead representing a carbon atom and its corresponding hydrogen atoms. The right chain is one example of coarse graining (CG) with each bead containing four molecules of the UA chain. The atom and bond sizes are not to scale.

Figure (3.1) shows the three levels of modeling for the same chain starting with an AA model (left) that includes the hydrogen atoms. If the hydrogen atoms

are incorporated with their respective carbon atom we get the UA in the center. Finally, if the atoms making up one molecule (4 atoms in this case) are combined together then we end up with one example of a CG model (right).

3.2 Force field

For the model [97] used in this project, Smith and Paul, developed a united atom force field for simulations of 1,4-polybutadiene using *ab initio* quantum chemistry calculations. As mentioned before, in a UA model the hydrogen atoms are grouped with their respective carbon atoms thus the atoms in this system consist of CH, CH₂ and CH₃. Since the model is intended for the study of the bulk for different temperatures, confinements and geometries, the reduction in the computational effort due to the UA model is crucial. Smith and Paul argue that for a non-polar hydrocarbon polymer like 1,4-polybutadiene, non-bonded electrostatic interactions between hydrogen and carbon atoms do not influence the conformational energies or the structure of the PBD. Not including these interactions would not then come at a loss for the reliability of the UA representation of the model. Therefore, such a model accurately represents the intermolecular interactions and the conformations that would allow us to study the static and dynamic properties of the melt.

The force field is a set of equations and their corresponding parameters designed to reproduce the molecular geometry, energy and properties of the studied polymers. Together with the equations of motion, they describe the time evolution of bond lengths, angles and torsions along the chain as well as non-bonded interactions such as the van der Waals and electrostatic interactions. For our model, prior to parameterize the force field, quantum chemistry studies were performed on model molecules and the resulting conformer energies were used in a Rotational Isomeric State [102] (RIS) analysis that was later extended to the representation of 1,4-polybutadiene. Quantum chemistry calculations work with the RIS model to map the energies and geometries of possible conformations for a given molecule. The RIS model incorporates several structural details including the differences in energy for conformations produced by rotation about a bond or pair of bonds and it makes accessible various conformation-dependent properties. Once the RIS representation of the model molecules' conformations is done, it can be extended to formulate the energy of different possible conformers and geometry parameters, including the bond lengths, angles and dihedral angles of

the studied polymer. The results are then employed to proceed with the force field parameterization. The force field of this UA model of 1,4-PBD includes bonded and non-bonded parameters.

3.2.1 Bonded interactions

The bonded parameters include three different types of interactions as shown in Figure (3.2).

This model makes no distinction between CH₂ and CH₃ thus the chain ends are treated as CH₂ united atoms. The force field only distinguishes between CH and CH₂. The stretching potential is generally defined as follows where i and j represent combinations of consecutive atoms that form a bond,

$$U^{stretch}(r_{ij}) = \frac{1}{2}k^{stretch}(r_{ij} - r_{ij}^o)^2; \quad (3.1)$$

however, Smith and Paul describe two-center bonded interactions by a fixed bond length as seen in Table (3.1).

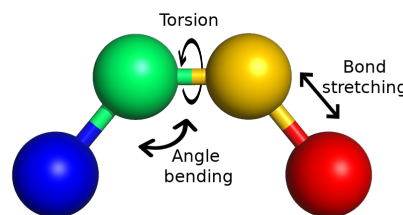


Figure 3.2: Schematic showing the different bonded potentials within a molecule.

Table 3.1: Stretching potential parameters of the parameterized force field of 1,4-polybutadiene.

Bonds (ij)	$k^{stretch}$ (kcal/(mol Å ²))	r_{ij}^o (Å)
CH ₂ -CH ₂	fixed	1.53
CH-CH	fixed	1.34
CH ₂ -CH	fixed	1.50

Therefore, $k^{stretch}$ (kcal/(mol Å²)) and the bond lengths are fixed and chosen such that they best reproduce the values obtained in quantum chemistry calculations. The three center bonded interactions are defined by a harmonic angle bending potential function,

$$U^{bend}(\theta_{ijk}) = \frac{1}{2}k_{ijk}^{bend}(\theta_{ijk} - \theta_{ijk}^o)^2 \quad (3.2)$$

where θ_{ijk} is the angle defined by three consecutive bonded UA along the chain with a defined k_{ijk} (kcal/mol) seen below in Table (3.2).

Table 3.2: Angle bending potential parameters of the parameterized force field of 1,4-polybutadiene.

Atoms(<i>ijk</i>)	k_{ijk}^{bend} (kcal/mol)	θ_{ijk}^o (rad)
CH ₂ -CH ₂ -CH	115	1.9487
CH ₂ -CH-CH	89.4	2.1973

The bending potential only contributes in case of a deviation from the desired equilibrium bend angle θ_{ijk}^o between the atoms *i*, *j* and *k*.

The final contributing bonded potential is the four-center interaction, also known as the torsional or dihedral potential. A dihedral angle is between the plane formed by the first three atoms and the last three atoms of four consecutive bonded atoms along the chain. The potential is defined by a six-term cosine series given by,

$$U^{tors}(\phi_{ijkl}) = \frac{1}{2} \sum_n k_{ijkl}^{tors}(n) [1 - \cos(n\phi_{ijkl})]. \quad (3.3)$$

Table 3.3: Parameters of the torsional potential of the parametrized force field of 1,4-polybutadiene. The α and β are rotations around CH=CH-CH₂-CH₂ and CH-CH₂-CH₂-CH bonds respectively.

Dihedral	k_1	k_2	k_3	k_4	k_5	k_6
CH ₂ -CH-CH-CH ₂		24.2				
$\alpha(cis)$	1.033	-0.472	0.544	0.263	0.346	0.164
$\alpha(trans)$	-0.240	-0.730	1.978	0.082	0.091	-0.056
β	-0.888	-0.619	-3.639	-0.066	-0.247	-0.190

The quantum chemistry calculations produce a unique value of $k_{ijkl}^{tors}(n)$ (included in Table (3.3)) for different torsional angles and different values of *n* (going from 1 to 6). Figure (3.3a) shows the torsional potential energy for the several values of *n* for the $\alpha(cis)$ dihedral angle where the values of k_{ijkl}^{tors} can be found in Table (3.3). The figure is zoomed in and only shows values for ϕ_{ijkl} up to $\simeq 6^\circ$ so that the curves appear clearly.

3.2.2 Non-bonded interactions

For the non-bonded interactions, the model only has the van der Waals interaction and an overlap repulsive term defined by the Lennard-Jones (LJ) potential [103]. As mentioned at the beginning of this section, the partial charges of the atoms are not included in the force field thus there is no Coulomb interaction. These charges are small and including them would slow down the MD simulations but will eventually not lead to any significant change in the atoms' positions. The intramolecular non-bonded interactions are taken into account only for atoms separated by four bonds or more and are defined by,

$$U^{LJ}(r_{ij}) = \sum_{i,j} 4\varepsilon_{ij} \left[\left(\frac{\sigma_{ij}}{r_{ij}} \right)^{12} - \left(\frac{\sigma_{ij}}{r_{ij}} \right)^6 \right] \quad (3.4)$$

with the parameters shown in Table (3.4).

Table 3.4: Lennard-Jones potential parameters of the parameterized force field of 1,4-polybutadiene for non-bonded interactions.

Non-bonded Atoms(<i>ij</i>)	ε_{ij} (kcal/mol)	$r_{min,ij}$ (Å)
CH ₂ -CH ₂	0.0936	4.500
CH-CH	0.1000	3.800
CH ₂ -CH	0.1015	4.257

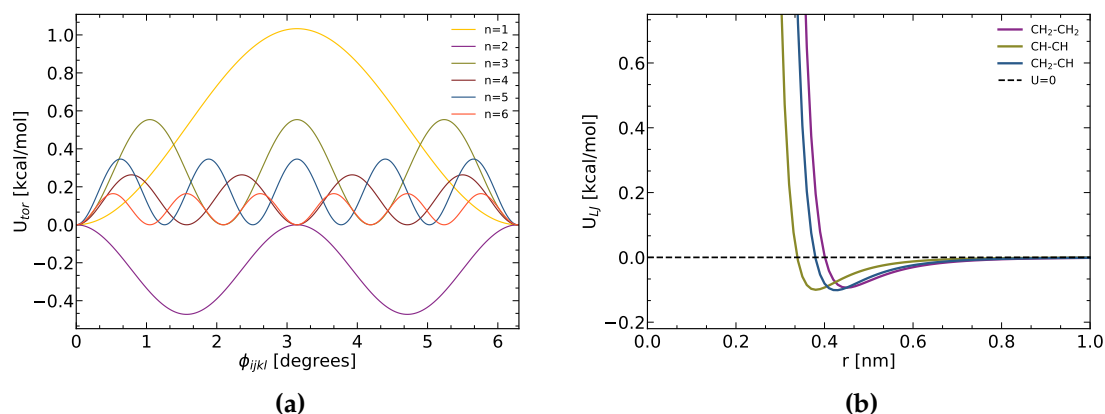


Figure 3.3: (a) Torsional potential energy for different values of n for the $\alpha(cis)$ dihedral angle zoomed in from 0 to 6 degrees. The sum over all these would give the total torsional potential energy for the $\alpha(cis)$ dihedral and (b) the Lennard-Jones potential for all three defined non-bonded interactions between different atoms.

¹In the simulations the parameters found in Tables (3.1),(3.2), (3.3), (3.4) were converted to nm and kJ/mol

The LJ potential is depicted in Figure (3.3b) for all three types of non-bonded interactions. ϵ_{ij} is the well depth of the potential and can measure the attraction strength between two atoms. σ_{ij} is the distance at which the potential is zero and is referred to as the 'size' of the atom. Table (3.4) gives the value of r_{min} which is the distance at which the $U_{LJ} = -\epsilon$ and is given by $r_{min} = 2^{1/6}\sigma$. From Figure (3.3b) one can see a slight difference in the potential well depth while the van der Waals radius is smallest for the CH-CH interactions given that the size and mass of the CH united atom is smaller compared to CH₂.

Ultimately, the complete expression of the force field interactions is the following

$$U = U^{LJ}(r_{ij}) + \sum_{ij} U^{stretch}(r_{ij}) + \sum_{ijk} U^{bend}(\theta_{ijk}) + \sum_{ijkl} U^{tor}(\phi_{ijkl}) \quad (3.5)$$

with θ and ϕ indicating the bend and torsional angles respectively and i, j, k , and l refer to different atoms along the chain. Eq.(3.5) is used to calculate the forces acting on the atoms in the MD integration scheme (refer to chapter 2) when solving the equation of motion.

The molecular topology including masses, LJ parameters and all the bonded interaction parameters are described for each chain in the GROMACS [104–106] topology file (.top file format). Appendix A includes an example of the topology for one PBD chain with *cis* and *trans* configuration stated on line 385 of the topology file.

3.2.3 Validation of the Model: MD simulations vs. Experiments

The model [97–100] described above has been studied in simulations of the bulk [91,92,99,107] and it has been validated against experiments performed on melts of the same microstructure (chain lengths and *cis/trans* configurations) [91,108]. Furthermore, it has also been studied in slit confinement [22,23,43,45] and for a supported film [109].

The density calculated in the simulations [91,92] is in good agreement with the experimental value. NMR spin lattice relaxation studies [92] show that the spin lattice relaxation time T_1 obtained from the simulations by fitting the orientational autocorrelation functions (OACF) of C-H bonds for different conformations, is in agreement with the experimental values except for the resonances concerning the carbons in the vinyl group. The latter is due to the fact that the vinyl

groups are not considered explicitly in the simulations but rather represented by a CH₂ atom. Furthermore, neutron spin echo (NSE) studies [98] demonstrate excellent agreement between the experimental measurements and the calculations from MD results for the single chain intermediate coherent dynamics structure factor. This further validates Smith and Paul's model and sets a foundation for additional research on PBD in more complex systems, for e.g. [22,23,43,45].

3.3 Preparations and simulations

3.3.1 Alumina

We have mentioned before that the invention of microporous alumina [93] was significant to the research of polymer melts in controlled confined environments and thus also an essential part of our simulations. The work on the alumina was done by our collaborator M. Solar and its force field was taken from literature [110,111]. From a unit cell, a crystal bulk sample was built then the latter was heated to a high temperature (3000 K) in 500 ps followed by an equilibration run at that temperature for 25 ns. Finally the bulk sample was quenched from 3000 to 294 K with a cooling rate of 2.706 K/ps. Our publication [112] contains a more detailed description of the alumina bulk sample preparation process. The process of constructing the nano-pore and nanorod from the alumina bulk sample will follow in the respective sections below along with the melt preparation.

3.3.2 PBD in a nano-pore and the resist cylinder

One of the systems that we study involves confining a PBD melt in a 10 nm diameter pore. The melt that was used was prepared and used before for several studies concerning flat wall confinement [22,23,43,45,113]. The simulation box size of the bulk system was $x_{box} = 14.91$ nm, $y_{box} = 13.0192$ nm and $z_{box} = 10.393$ nm with a total of 720 chains. To confine and fit the melt into the pore, two main procedures were carried out. The average density in the melt in confinement should converge towards the bulk density and the latter is dependent on the volume of confinement and the mass which in itself is dependent on the total number of chains. Therefore, we can estimate the total number of chains in the

system needed to achieve bulk density. The second procedure is to confine the melt into the desired diameter.

The chains in the melt consist of 29 repeating units; therefore, each chain has 116 united atoms. Given that the chain ends are considered to be CH₂ atoms, then each PBD molecule consists of two CH₁ and two CH₂ atoms and the whole system should have $N_{total} = N_{CH_1} + N_{CH_2}$ where $N_{CH_1} = N_{CH_2}$. The density would then be defined as,

$$\begin{aligned} \rho &= \frac{N_{CH_1}m_{CH_1} + N_{CH_2}m_{CH_2}}{V} \\ &= \frac{N_{CH_1}(m_{CH_1} + m_{CH_2})}{\pi r^2 h} \end{aligned} \quad (3.6)$$

where $r = 5$ nm is the radius of the pore, h is the height and m_{CH_1} and m_{CH_2} are the masses of CH₁ and CH₂ respectively. The volume is that of a cylinder. In MD units, the mass is defined in the unified atomic mass unit $u = 1.660538921 \times 10^{-27}$ kg then $m_{CH_1} = 13.019 \times u = 21.618 \times 10^{-27}$ kg and $m_{CH_2} = 14.027 \times u = 23.292 \times 10^{-27}$ kg. Experiments on the PBD melt have found that at $T = 353$ K the bulk density is $\rho_{353K} = 843$ kg/m³ [91], for $T = 413$ K $\rho_{413K} = 826$ kg/m³ and for $T = 298$ K the density is $\rho_{298K} = 895$ kg/m³ [114]. Previous MD simulations on PBD between graphite walls [24, 43] have used a bulk density of $\rho = 865$ kg/m³ for $T = 353$ K. Given that we are using the same model and melt as the mentioned simulations, for these calculations we assume the density they have used to proceed with an estimate of the number of chains in the system. Using all the above provided information we can calculate the total number of CH₁/CH₂ atoms and subsequently an estimate of the total number of atoms and chains in the system which is $N_c \simeq 270$ chains. A reduction of the total number of chains in the system from 720 to around 270 would result in a reduction in the number of interactions the algorithm has to account for and thus should result in faster simulations when done at the beginning of the preparation. We choose $N_c = 275$, which is greater than 270, for the preparation. We slightly increase the total number of chains since it would later be easier to remove chains to adjust the density than to add extra chains. When adding extra chains one would have to account for any overlaps between the new and existing chains as well as the distance between their atoms that could result in a blow up of the potential if the atoms are too close.

Resist cylinder

After reducing the number of chains, the second process would be to make the melt fit into a 10 nm diameter pore. A simple translation of the atoms to a smaller volume would result in overlaps and in very large values in the non-bonded interactions and is therefore not convenient. A more suitable method would be to have a repulsive "field" surrounding the melt that dynamically pushes the chains closer to each other and shrinks the melt slowly to the desired volume. To achieve that we applied the concept of a resist cylinder. This concept has been used before for preparations of silica nanopores [115,116] for MD simulations. The resist cylinder is made up of beads that apply a repulsive force when interacting with the melt. The repulsive beads (RB) are uniformly placed on circles of a certain diameter and radius r_{RC} (radius of resist cylinder) and the circles are arranged in a vertical stack as seen in Figure (3.4) and only interact with the melt via the Lennard-Jones non-bonded potential. Since we only need the force to be a repulsive one, the LJ parameters were chosen accordingly using the Lorentz-Berthelot [117,118] combining rules. The latter determine how different atom types with their own LJ parameters interact with each other. The Lorentz-Berthelot method defines the combining rules as follows,

$$\sigma_{ij} = \frac{\sigma_i + \sigma_j}{2} \quad \text{and} \quad \varepsilon_{ij} = \sqrt{\varepsilon_i \varepsilon_j} \quad (3.7)$$

where σ and ε are the familiar LJ parameters and the subscript ij describes mixed interactions. σ_{CH_1} and σ_{CH_2} are defined by the model and the values can be calculated from the values of the mixing parameters in Table (3.4) and eq.(3.7) given that the combining rules for a CH-CH or CH₂-CH₂ interaction produce the parameters for CH and CH₂ respectively. To define σ_{RB} (repulsive beads) we calculate its mixed interaction with CH₁. We choose CH₁ since it is the smaller atom compared to CH₂ and we calculate σ_{RB} such that $\frac{\sigma_{RB} + \sigma_{CH_1}}{2} = 0.9$, where 0.9 is the defined cut-off of the potential. This requires the interaction until the cut-off radius to stay a repulsive one with $\sigma_{RB} = 1.461458$ nm. The value of $\varepsilon_{RB} = \varepsilon_{CH_2} = 0.391805$ kJ/mol (similar to ε_{CH_2}) was chosen and did not result in any blow-ups in the non-bonded interaction potential. The final step before

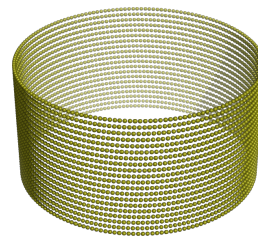
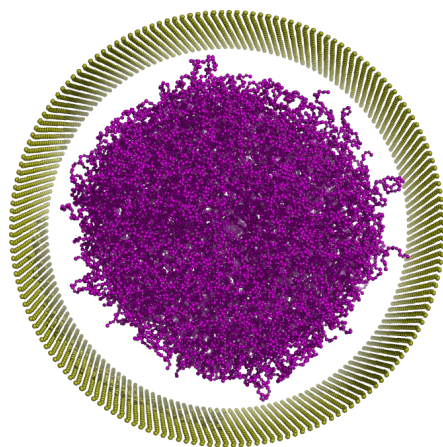
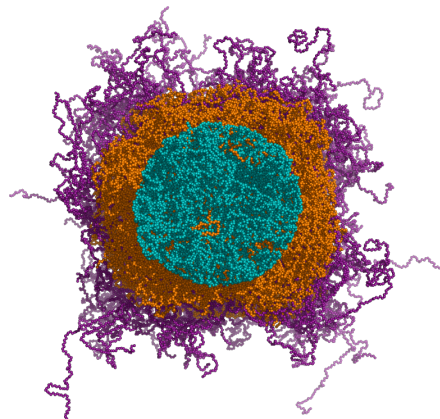


Figure 3.4: Resist cylinder made of the repulsive beads for $D = 20nm$. The bead size is not to scale.

applying the resist cylinder to the melt was to fix the position of the repulsive beads and to exclude any non-bonded interaction between them which prevents any changes in the radius of the cylinder due to the forces applied by the melt and by the beads on each other. Excluding any interaction between them also allows us to keep the number of beads constant and an overlap between them would not cause any unacceptably large forces that result in the failure of the simulations.



(a) A snapshot of the melt with $N_c = 275$ with the resist cylinder diameter of 15 nm.



(b) Three different snapshots of the melt in the preparation process. The purple melt is the starting configuration at $D_{RC} = 35$ nm and the orange melt is for $D_{RC} = 20$ nm with $N_c = 464$. The smallest and teal melt is for $N_c = 275$ for the final diameter $D_{RC} = 10$ nm.

Figure 3.5: Snapshots of (a) melt with the resist cylinder and (b) melt for three different diameters $D_{RC} = 35$ nm, 20 nm and 10 nm.

The PBD melt is placed inside the resist cylinder for short simulation runs. For the first few diameters, starting at 35 nm, the preparation simulations range from 100 ps to 500 ps and are carried out with $N_c = 464$ while decreasing the cylinder diameter by small decrements. For very large diameters with $N_c = 464$, 100 ps were sufficient to reduce the size of the cylinder; however, for smaller diameters and $N_c = 464$, simulations of around 500ps were needed. When the total number of chains was reduced to $N_c = 275$ we had a diameter of 15 nm and then 200 ps simulations were sufficient. In total, 24 short simulation runs were performed to obtain a melt inside a 10 nm diameter. Figure (3.5a) shows a snapshot of the output configuration of the melt and the resist cylinder for a diameter of 15 nm while Figure (3.5b) shows three overlapping different snapshots

for three different diameters. The first snapshot (purple) belongs to the starting configuration at $D_{RB} = 35$ nm while the second (orange) is the snapshot of the melt after applying a resist cylinder of diameter 20 nm (both with $N_c = 464$). The last snapshot (teal) is for $N_c = 275$ and the final diameter of 10nm. This configuration was later used to start the equilibration run for the PBD melt confined in the alumina nanopore.

Alumina nanopore

To prepare the nanopore, a cylinder was cut out of the alumina bulk described briefly in subsection 3.3.1 and in more detail in [112]. The cylinder is of diameter $D = 10$ nm and of thickness of around ~ 5 nm. The cylindrical slab geometry was introduced to reduce the simulation time when calculating the possible neighboring interactions compared to alumina filling a cubic simulation box.

Simulations

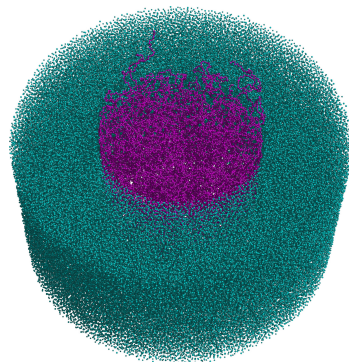


Figure 3.6: Polybutadiene melt inside the alumina nanopore.

We employ the GROMACS (GRONingen MACHine for Chemical Simulations) [104–106] package to perform MD simulations on the, thus, prepared pore-infiltrated PBD melt shown in Figure (3.6) . The software is well documented and is constantly upgraded with further improvements. The software itself has several built in force fields; however, as mentioned before, our model follows the force field described in section 3.2. For each temperature, (293, 323 and 353 K), a single simulation run was performed in the canonical ensemble (NVT) following 40 ns equilibration runs. The atoms of the alumina pore are fixed in space to save computational time. Periodic boundary conditions are imposed along the z-direction (along the axis) of the cylindrical pore.

Table 3.5: Lennard-Jones parameters for the alumina (ALU and OXY), melt (CH₁ and CH₂) and the resist cylinder atoms (RB).

Atoms	σ (nm)	ϵ (kJ/mol)
CH ₁	0.338542	0.418593
CH ₂	0.400904	0.391805
ALU	0.311797	2.360997
OXY	0.323102	0.936000
RB	1.461458	0.391805

Table 3.5 shows the LJ parameters for the melt (CH₁, CH₂), alumina (ALU, OXY) and the resist cylinder (RB) atoms. Standard Lorentz-Berthelot combining rules were used to determine the LJ interactions between the alumina and the united atoms of the PBD model. The PBD model has very small partial charges in the monomers, which have been ignored so far in melt simulations without affecting their ability to reproduce experimental findings. We, therefore, do not take Coulomb interactions with the alumina into account. Finally, the system uses the Nosé-Hoover thermostat and the simulations had an integration time step of $\delta t = 1$ fs and a simulation time of up to 410 ns for each temperature.

3.3.3 PBD surrounding a nanorod

The other system studied is that of a polymer melt surrounding an alumina nanorod. Similarly to the previous system, the PBD melt and alumina had to undergo some preparation before the simulations took place.

Alumina nanorod

From the alumina bulk of subsection 3.3.1, a rod of diameter $D = 10$ nm was cut out by simply removing all oxygen (OXY) and aluminum (ALU) atoms with a radius > 5 nm where the center is placed in the center of the bulk. The melt used in this system is the same one used in the nano-pore geometry; however, in this case the melt has to be placed in a simulation box that fits a nanorod with a 10 nm diameter. The box should also be big enough such that the melt extends far enough from the rod in order for us to observe bulk-like behavior. However, one should keep in mind that the size of the melt should not come at the expense of computational time and power. The way we chose to approach this is described below and a schematic description in Figure (3.7).

PBD preparation

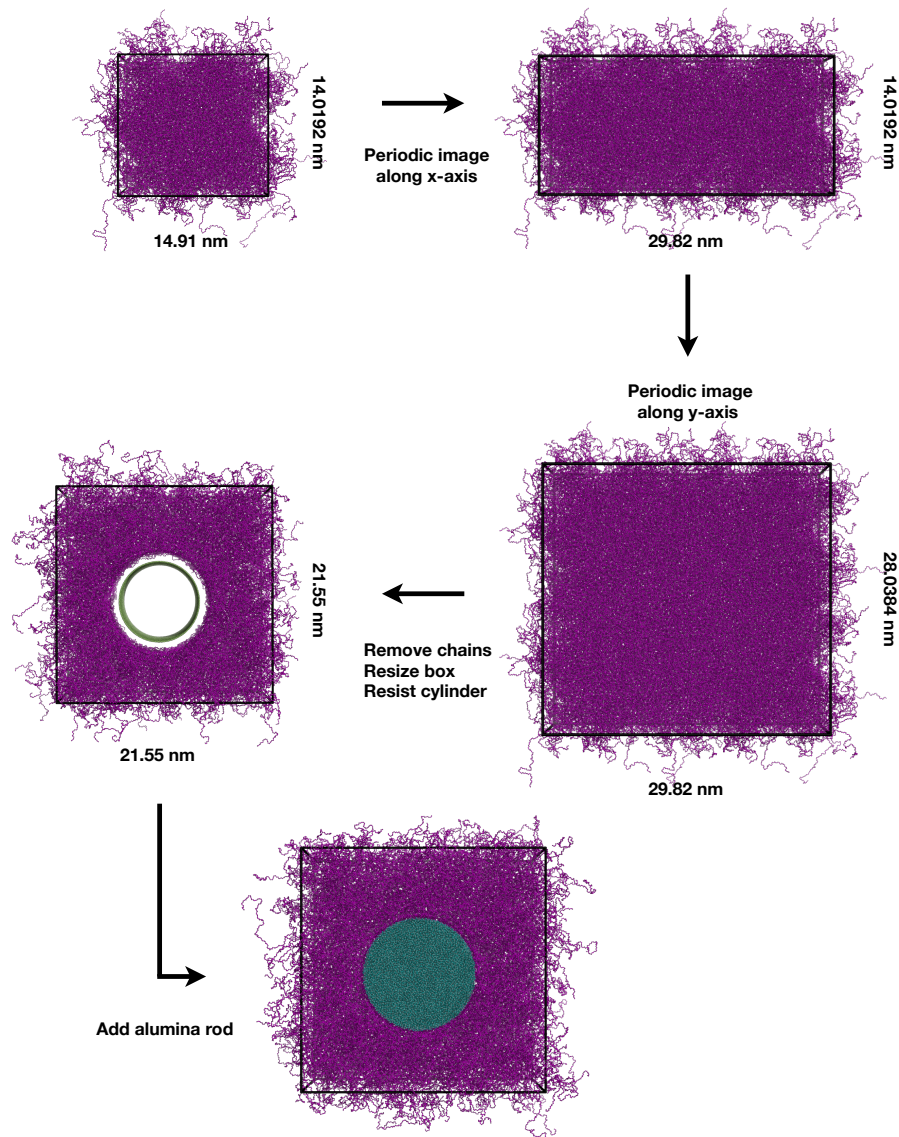


Figure 3.7: Schematic of the preparation process of the polybutadiene melt for the simulations of PBD surrounding an alumina nanorod. Steps 1 \rightarrow 2 show the periodic image of the original melt along the x-axis. Steps 2 \rightarrow 3 is the addition of the periodic image along the y-axis after which the simulation box is resized to the desired size of $x_{box} = 21.55 \text{ nm}$, $y_{box} = 21.55 \text{ nm}$ and $z_{box} = 10.604 \text{ nm}$, the number of chains is reduced to $N_c = 1361$ and the resist cylinder method is applied to expand the melt to fit a 10 nm diameter rod (step 4). The final figure (step 5) shows a configuration of the melt surrounding the nanorod for the production runs at $T = 293 \text{ K}$.

Starting with the original melt with 720 chains and a simulation box of size $x_{box} = 14.91$ nm, $y_{box} = 13.0192$ nm and $z_{box} = 10.393$ nm (z_{box} remains the same unless stated otherwise), we use Avogadro: an open source molecular builder and visualization tool [119] to create a super cell with a copy of one periodic image of the melt along the x-direction resulting in a simulation box with $x_{box} = 29.82$ nm (y_{box} and z_{box} unaltered). This can be seen in Figure (3.7) steps 1 \rightarrow 2. From the latter, a copy of the periodic image in the y-direction is made resulting in $x_{box} = 29.82$ nm and $y_{box} = 28.0384$ nm as seen in Figure (3.7) steps 2 \rightarrow 3. The melt now consists of $720 \times 4 = 2880$ chains in total. It is possible to proceed with the current box size; however, to make the simulations more efficient and faster the dimensions are reduced such that the melt extends at least 5 nm radially away from the rod surface. The new dimensions of the simulation box become $x_{box} = 21.55$ nm, $y_{box} = 21.55$ nm and $z_{box} = 10.604$ nm. With fixed dimensions and volume of the box and the alumina nanorod, the number of chains in the system can be calculated according to eq.(3.6) such that we obtain a density close to its bulk value away from the nanorod. Consequently, the number of chains in this system is calculated to be $N_c \simeq 1361$. To reduce the box size and the number of chains in the system we start by removing chains beyond a radius ~ 10.5 nm (5 nm nanorod and ~ 5.5 nm melt). To maintain the desired number of chains, for the position of the nanorod we remove chains up to ~ 4 nm radius and then proceed with the resist cylinder method described in subsection 3.3.2 seen in step 4 in Figure (3.7). Finally, the prepared alumina rod and the melt are merged as seen in step 5 of Figure (3.7) for the equilibration and production runs.

Simulations

The GROMACS [104–106] package is again used for our simulations of PBD surrounding a nanorod. At each temperature ($T = 293, 323$ and 353 K) a 30 ns equilibration run took place. The production runs' length at each temperature differed slightly depending on the nodes used on the cluster. For $T = 293, 323$ and 353 K the simulations ran for 300, 250 and 220 ns respectively. The atoms of the alumina rod are fixed in space and periodic boundary conditions are applied in all three directions. The Lennard-Jones parameters of the PBD and alumina atoms as well as the resist cylinder can be found in Table 3.5 where standard Lorentz-Berthelot rules were used to determine the interactions between the PBD melt and the alumina. This system, similarly to the previous one, uses the Nosé-Hoover thermostat and an integration time step of $\delta t = 1$ fs.

Chapter 4

Polybutadiene confined in an alumina nanopore

Simulations of chemically realistic polymer melts infiltrated with NPs are expensive computationally and time-wise. The time needed for the NPs to uniformly disperse and for equilibration is beyond the scope of this work. So far, simulations [31, 65–67, 69, 71, 72, 120] concerning PNCs with NPs have been conducted using mostly the bead-spring model with single or few NPs. Therefore, a simplification in one or more factors has to be done in order to proceed. If we wish to study a chemically realistic united atom model's behavior in the vicinity of nanofillers, we need to set up a more efficient method to simulate the curvatures present in a filler network as well as the confinement implemented on the polymer melt. To do so we simulate a fixed nanopore infiltrated with the PBD melt and another system with a fixed nanorod surrounded by the melt. The former will be the focus of this chapter while the next chapter will tackle the simulations on a PBD melt surrounding a nanorod. The PBD model is described briefly in chapter 3 and more details can be found in [91, 97].

A number of simulations [22–24, 43, 44, 113] have used the same model of PBD to study the effects of slab/parallel walls confinement and have shown several structural and dynamical changes to the melt. The results in this chapter will be examined in comparison with the studies of the PBD model in 1D confinement as well as experiments and simulations on melts in cylindrical confinement and melts infiltrated with NPs. The chapter is divided into two main parts where section 4.1 goes into the details of the structural effects imposed by the cylinder and section 4.2 discusses the changes in the dynamics. The two are not disconnected and a change in the structure can predict modifications to the way the chains

and monomers move. Therefore, the sections are separated for organizational purposes but in fact they are very much entwined.

4.1 Structure across the nanopore

The structure and dynamics of polymer melts are correlated; therefore, more knowledge on how the structure of the melt is altered under confinement and certain curvatures could provide a better picture of the changes in the melt's dynamics. The change in the structure is a consequence of the impenetrable walls of the confinement (cylindrical in this case), their size compared to that of the chains' and their interaction with the melt. The structure of melts confined in nanopores has been examined by several experimental techniques including but not restricted to neutron scattering [36, 37, 40] and nuclear magnetic resonance [34]. Before we proceed, it is good to note that for studies on polymer-NP mixtures, it is well recognized that the effect on the structure is the product of the characteristics of the nanoparticle itself (for example: size, shape, surface) as well as the polymer (for example: structure, type of interaction with the NP, molecular weight).

In this section, we focus on the structure of the melt on several scales. We investigate the density layering across the nanopore as well as the orientational ordering in the melt, brought about by the confinement, on both the segmental and chain scales. For the chain scale ordering, the magnitude and orientation of the axes of the gyration tensor ellipsoid of single chains are studied and are found to prefer to align parallel to the pore axis. Even though double bonds near the wall are preferentially oriented along the pore wall and closer to the axis, studying the nematic order parameter indicates that there is no nematic ordering at the melt-wall interface beyond a geometrical constraint enforcing orientation along the pore wall.

4.1.1 Density layering

It is well known that an attractive interaction between the monomers and the confining walls leads to a layering in the density profile of the system. The bulk density is expected to be restored in the center of the melt. As a result, during the preparation of the melt (details found in section 3.3), the total number of chains $N_c = 275$ was chosen such that the density in the center of the cylinder with a

radius of 5 nm is that of PBD at $T = 353$ K.

In our simulations, the monomer density profile was calculated along the radial direction (\hat{e}_r). The pore was divided into cylindrical slabs of constant volume with a slab thickness at the wall of 0.1 \AA . Thus, as we approach the center of the nanopore, the thickness of the slab increases. The spatial locations of the monomers along the radial direction were calculated for each slab and then averaged over the entire trajectory.

The density profile especially at the vicinity of the confining wall is an interplay between the configurational and packing entropic effects.

At high densities and attractive surfaces the monomers pack close to the surface in spite of the fact that their respective chains lose configurational entropy as a result of this approach. Figure (4.2a)¹ shows a strong layering at the interface in the monomer density along the radial direction of the cylindrical nanopore. This is a well known occurrence for melts at surfaces [25] and in confinement [24, 39, 45]. This effect can also be seen for systems with repulsive walls [24, 39]; however, with attractive walls the layering is more prominent and extends slightly further into the melt (5 layers instead of 4). The first peak is at $r \sim 4.7$ nm or

~ 0.35 nm away from the nanopore's surface ($r \sim 5.0865$ nm). Similarly, the peaks are at a distance of ~ 0.43 nm from each other. Thus, the length scale identified in the layering is around the size of the monomer $\sigma \simeq 0.4$ nm. The perturbation extends to about 2.5 nm away from the pore walls after which a constant density agreeing (within 2.1% percentage difference) with the bulk density (865 kg/m^3) at the reference temperature $T = 353$ K is obtained. The layering is comparable to the results seen by Tung et al. [39](CG model) and is similar for all temperatures with slightly higher first and second peaks for lower temperatures. From Figure (4.2a) one can see 5 prominent layers with decreasing densities as we approach the center of the pore. In Figure (4.1) we use the molecular visualization system Pymol [121] to clip a 0.2 nm slab about chain number 90 (which in the configu-

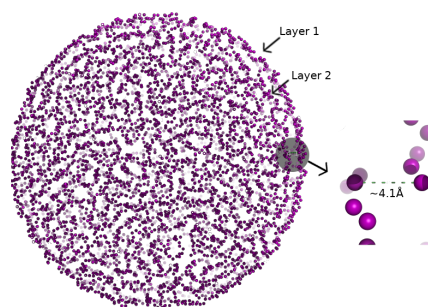


Figure 4.1: Visualization of a slab of thickness 0.2 nm along the axial direction of the nanopore showing the layering effect and the distance between the first two layers.

¹In this figure and all the figures in the current section, r is the radial position with a value of 5 at the wall and 0 is the center of the nanopore.

ration file used lies axially in the center of the pore). The first and second layers are visible in the figure and we were able to use the measurement feature in the software to calculate the distance between an atom in the first layer and another in the second layer. Figure (4.2b) shows very similar results. The latter figure is a 2D monomer density map of the melt at $T = 293$ K averaged over $t = 100$ to 200 ns. The map displays the density along the radial direction (\hat{e}_r) with a grid size of 0.02 nm averaged along the axial direction (\hat{e}_z). The density is normalized to its value in the center; therefore, the darker purple represents areas with high densities especially close to the wall. A layering can be observed and decreases in intensity as we move away from the pore walls until a homogeneous density is reached after $\sim 4 - 5$ layers. The density beyond ~ 5 nm is zero given that there is no melt there but rather the alumina nanopore. Also seen in Figure (4.2a) is the layering in the center of mass (COM) density for $T = 353$ K with a length scale $\simeq R_g$ (radius of gyration) of the PBD chains. A plot including the COM density layering for all three temperatures can be found in Figure (B.1) in Appendix B.

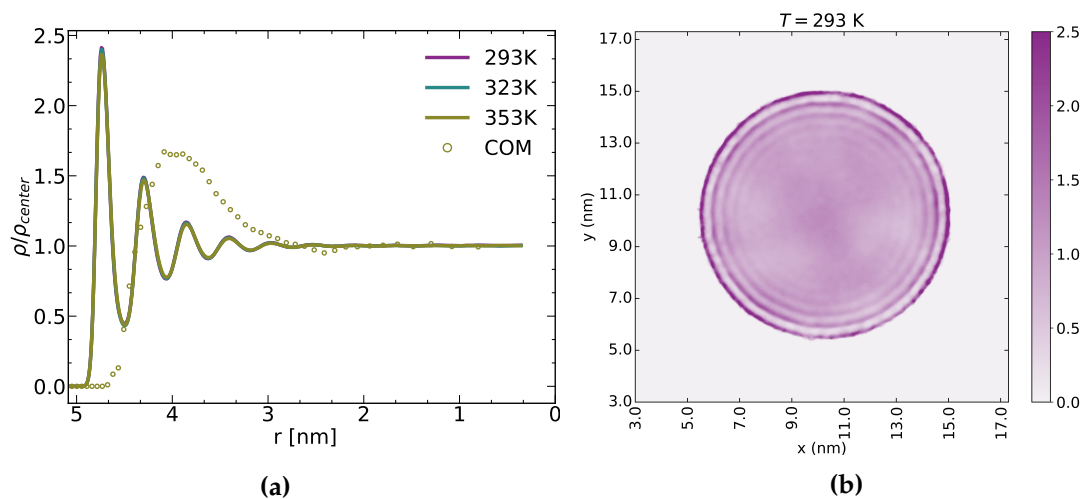


Figure 4.2: (a) Layering effect in the monomer and chain center of mass ($T = 353$ K) density of the confined PBD. The curves for all three temperatures are normalized to their value at the center of the nanopore. The volume of the bins (~ 3.4 nm³) used to calculate the density was kept constant throughout the pore. (b) A 2D monomer density map along the x and y directions showing the layering effect with a grid size of 0.02 nm averaged along the axial direction. The density is calculated at $T = 293$ K and is normalized to the value in the center.

The density profile and the position and height of its layers suggest that there could be an adsorbed layer of monomers at the wall [22–24,45] which we intend to investigate later along with its dynamical implications. Moreover, it also sug-

gests that there exists some type of orientational ordering on both the segmental and chain scales. For the former, the density profiles allow us to predict that the double bonds ($l_{DB} = 0.134$ nm) at the surface do not prefer to lie perpendicular to the cylindrical wall.

4.1.2 Double bond orientational ordering

MD simulations on PBD between graphite walls [23] studied the orientation of the double bonds and their preference to orient parallel to the walls. Our previous results of the density also suggest that such an orientation is possible. If the double bonds preferred to lie perpendicular to the pore walls, then we would expect the second peak in the density layering to be at a distance greater than 0.3-0.4 nm away from the first peak. To address the orientational ordering of the double bonds at the wall-melt interface, we calculate the second Legendre Polynomial of the angle (θ) between the double bonds in the repeating units of the chains with the radial (\hat{e}_r) and axial (\hat{e}_z) directions,

$$\langle P_2 \rangle = \frac{1}{2} [3 \langle \cos^2(\theta) \rangle - 1]. \quad (4.1)$$

Eq.(4.1) has a value of $\langle P_2 \rangle = 1$ for $\theta = 0^\circ$ and 180° which means the double bonds are parallel to the respective direction and $\langle P_2 \rangle = -0.5$ when the double bonds are perpendicular to the respective direction with $\theta = 90^\circ$. For the calculations, the position is determined by the radial position of the center of mass of the double bond.

Figure (4.3) shows the orientational function defined in Eq.(4.1) for three different temperatures ($T = 293, 323$ and 353 K) for the angle with the radial direction \hat{e}_r and for $T = 353$ K for the axial direction \hat{e}_z . The inset of Figure (4.3) shows the decaying phase difference defined in Eq.(4.2) between θ_r and θ_z for all three temperatures. The grey dashed line represents the radial position of the pore wall. We observe a similar behaviour to the density layering that also extends to ~ 2.5 nm from the pore walls.

$$\Psi(r) = |\theta_r(r) - \theta_z(r)| \quad (4.2)$$

With a value of $P_2(\theta_r)$ very close to -0.5 , it is clear that the double bonds have a

preference of orienting themselves perpendicular to the normal to the confining surface. From the value of $P_2(\theta_z)$ at $T=353\text{K}$, we can also deduce that the double bonds do not align parallel to the axial direction either but rather make a $\sim 40^\circ$ angle with \hat{e}_z . This implies that the double bonds lie along the curvature of the surface of the nanopore but not fully along the axial direction. The peaks of the orientational ordering are sharper for lower temperatures especially for the first peak but there is no strong difference in magnitude. This coincides with findings in [23,44] for the same model of PBD confined between graphite walls.

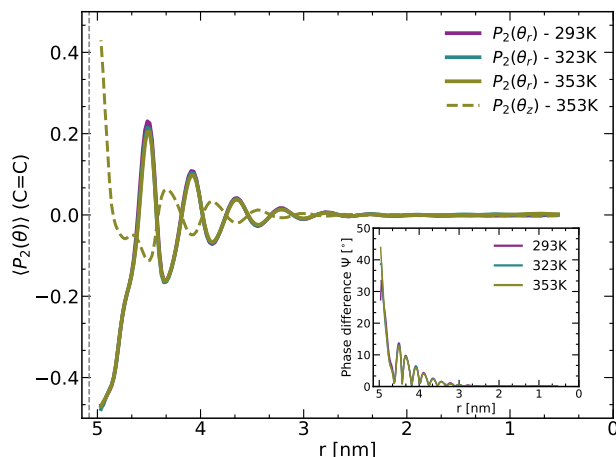


Figure 4.3: Orientational ordering of the double bonds in the chains' repeating units given by the second Legendre polynomial of the angle between the double bonds and the radial and axial directions. The inset is the phase difference Ψ (defined in Eq.(4.2)) between θ_r and θ_z at all three temperatures. The vertical dashed line indicates to radial position of the pore wall at ~ 5.0865 nm.

Supplementary Figure (B.2) shows for all three temperatures ($T = 293, 323$ and 353K) the second Legendre polynomial $\langle P_2 \rangle$ of the angle (θ_z) between the double bonds and the axial direction. The angle between the double bonds and the radial direction, θ_r , is comparable for all three temperatures and that can be seen in Figure (4.3); however, it differs slightly for θ_z . As the temperature increases the double bonds become more aligned with the axial direction.

4.1.3 Chain ordering and orientation

Gyration Tensor

Studies concerning various confinement types [22, 48, 50, 51, 53, 122] have found an ordering of the chains at the surface of confinement as a result of the induced

spatial confinement. To examine the structural effects on the chain scale, we study the gyration tensor (Eq.(4.3)) of the chains in the system,

$$\mathbf{G} = \frac{1}{N} \sum_i (\mathbf{r}_i - \mathbf{r}_{COM})(\mathbf{r}_i - \mathbf{r}_{COM}). \quad (4.3)$$

Here we divide the nanopore into slabs of the same size (5 Å) across the radial direction $\hat{\mathbf{e}}_r$ and a chain belongs to a certain slab if its center of mass (COM) is in that slab at time t . N in Eq.(4.3) is the total number of united atoms in the chain (116 UA) and the gyration tensor is calculated for each chain at each time t (for 41000 frames \equiv 410 ns). Given the matrix \mathbf{G} , with $\mathbf{r}_i = (x_i, y_i, z_i)$ and \mathbf{r}_{COM} the position of the center of mass of the chain, we can calculate several shape descriptors from the eigenvalues where we assume that the eigenvalues are sorted in descending order such that $\lambda_1 \geq \lambda_2 \geq \lambda_3$. The eigenvalues can be thought of as the axes of the gyration ellipsoid illustrated in Figure (4.4), with λ_1 as the longest axis.

The two shape descriptors of importance to us are the trace and the relative shape anisotropy. The former results in the squared radius of gyration of the chains that describes the size of the chain and is expressed as,

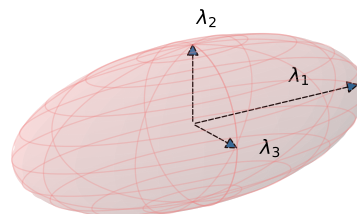


Figure 4.4: Illustration of the gyration ellipsoid with its axes.

$$Tr\mathbf{G} = \lambda_1 + \lambda_2 + \lambda_3 = R_g^2. \quad (4.4)$$

The second shape descriptor, the relative shape anisotropy (κ^2) defined in Eq.(4.5), encodes the dimensionality and symmetry of the polymer conformation. It is limited between 0 and 1 with zero indicating spherical conformations and 1 is for ideal rod-like structures. It converges to 1/4 for planar symmetric conformations.

$$\kappa^2 = 1 - 3 \frac{\lambda_1 \lambda_2 + \lambda_2 \lambda_3 + \lambda_3 \lambda_1}{(\lambda_1 + \lambda_2 + \lambda_3)^2} \quad (4.5)$$

Figure (4.5) and Figure (4.6) show respectively the gyration radius of the

chains and the averaged eigenvalues of the gyration tensor of Eq.(4.3) as a function of the radial distance of the center of mass of the chain. Figure (4.6) also displays the relative shape anisotropy of the chains' gyration ellipsoid. For the lowest temperature $T = 293$ K the chains' anisotropy approaches 1 before it decreases to reach a plateau but never reaches 0 which means that the chains at the center do not have completely symmetric conformations but rather the shape is ellipsoidal as initially suggested by Kuhn [123]. For the higher temperatures $T = 323$ K and $T = 353$ K, the anisotropy has an almost homogeneous value across all of the bins including the one at the wall and takes a value comparable to the bulk value of ~ 0.4 .

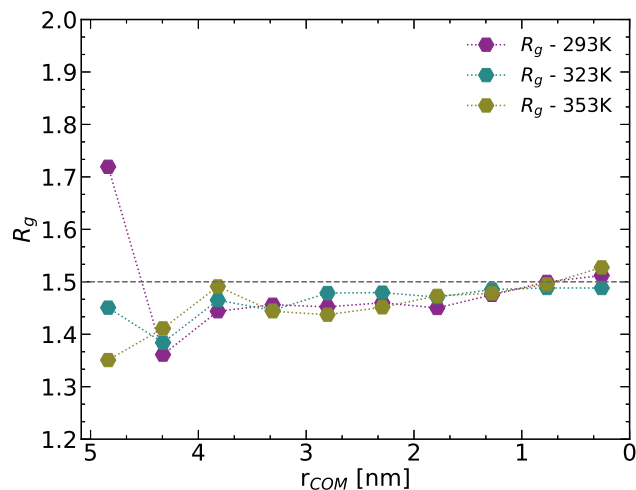


Figure 4.5: Gyration radius ($\sqrt{\text{Tr}\mathbf{G}}$) of the chains across the nanopore for all three temperatures. The dashed grey line is the bulk value of R_g . r is determined by the radial position of the center of mass of the chain.

The shape of the chains can also be seen from the magnitudes of the ellipsoids' axes. λ_1 which is the longest axis, decreases as we move away from the wall ($T = 293$ K); however, for all three temperatures, λ_1 remains much larger than both λ_2 and λ_3 along the whole radial direction. This is in agreement with the literature value [124,125] and the ratio of the principal components of the gyration ellipsoid away from the pore wall is $\langle\lambda_1\rangle:\langle\lambda_2\rangle:\langle\lambda_3\rangle \simeq 1:0.21:0.07$ at $T = 293$ K. The caption of Figure (4.6) contains the ratio for the other two temperatures. Monte Carlo studies [124] and analytical interpretations [125] have shown that the shape of a random flight chain is not symmetric where the ratio of the principal axes is $1:0.23:0.085$. Simulations of bulk 1,4-PBD [126] have also produced the same ratio for the eigenvalues. The plateau value of around 0.4 for the relative

shape anisotropy was also obtained at different temperatures in simulations of a PBD melt [126] and for simulations of bead-spring chains in cylindrical confinement [127] for the center of the pore. The bulk value for R_g is also included in Figure (4.5). The radius of gyration R_g fluctuates around the value 1.46 ± 0.08 nm (2σ error for $T = 293$ K) along \hat{e}_r , comparable to the bulk value of 1.5 nm, except for a distance of 0.5 nm away from the wall especially at $T = 293$ K. For the other two higher temperatures the gyration radius is close to its bulk value away from the wall as well. As we decrease the temperature, the shape of the chains at the cylindrical pore wall deviates from that of slit confinement between graphite walls, where the chains get oriented but not stretched. In our case we observe that for lower temperatures there is stretching and a pancake-like structure (seen also in [127] but to a weaker degree) of the chains at the interface resulting also in a larger radius of gyration and $\langle \kappa^2 \rangle$. The almost rod-like value for the anisotropy for chains with COM at 0.2 nm from the wall suggest that these chains are extended and adsorbed. We will later on link this to the slow desorption process of the monomers that is prominent at $T = 293$ K. This effect is a result of a mixture of geometry, temperature and the attractive pore surface of the alumina. Whether this change in structure is influenced more by either the geometry or by the nature of the interaction is still a matter of investigation.

In cylindrical confinement the chains oriented perpendicular to the radial direction are in the (z, φ) -plane. However, curvature and surface corrugation effects may induce an alignment along the axial direction. To further understand the orientation of the chains, we study the direction of the longest axis, λ_1 , of the gyration ellipsoid of the chains in the melt. To do so, we calculate the eigenvector of λ_1 in cartesian coordinates. Since the ellipsoid has head/tail symmetry the absolute value of the calculated eigenvector was taken i.e. all components are in the first octant of the cylinder. Figures (4.6b), (4.6d) and (4.6f) reveal the orientation of the longest axis of the gyration ellipsoid for all three temperatures. Over a distance of $\simeq 1$ nm from the confining wall there is a noticeable alignment with the axial direction that gets stronger as we decrease the temperature and is most prominent in the first layer of thickness 0.5 nm away from the wall. In the bins beyond that the eigenvector displays a homogeneous behaviour in all three directions. This proves that the confinement affects the orientation on both the segmental and chain scale. Moreover, the configurations transition from three dimensional configurations in the bulk to almost two dimensional and flat at the interface at $T = 293$ K.

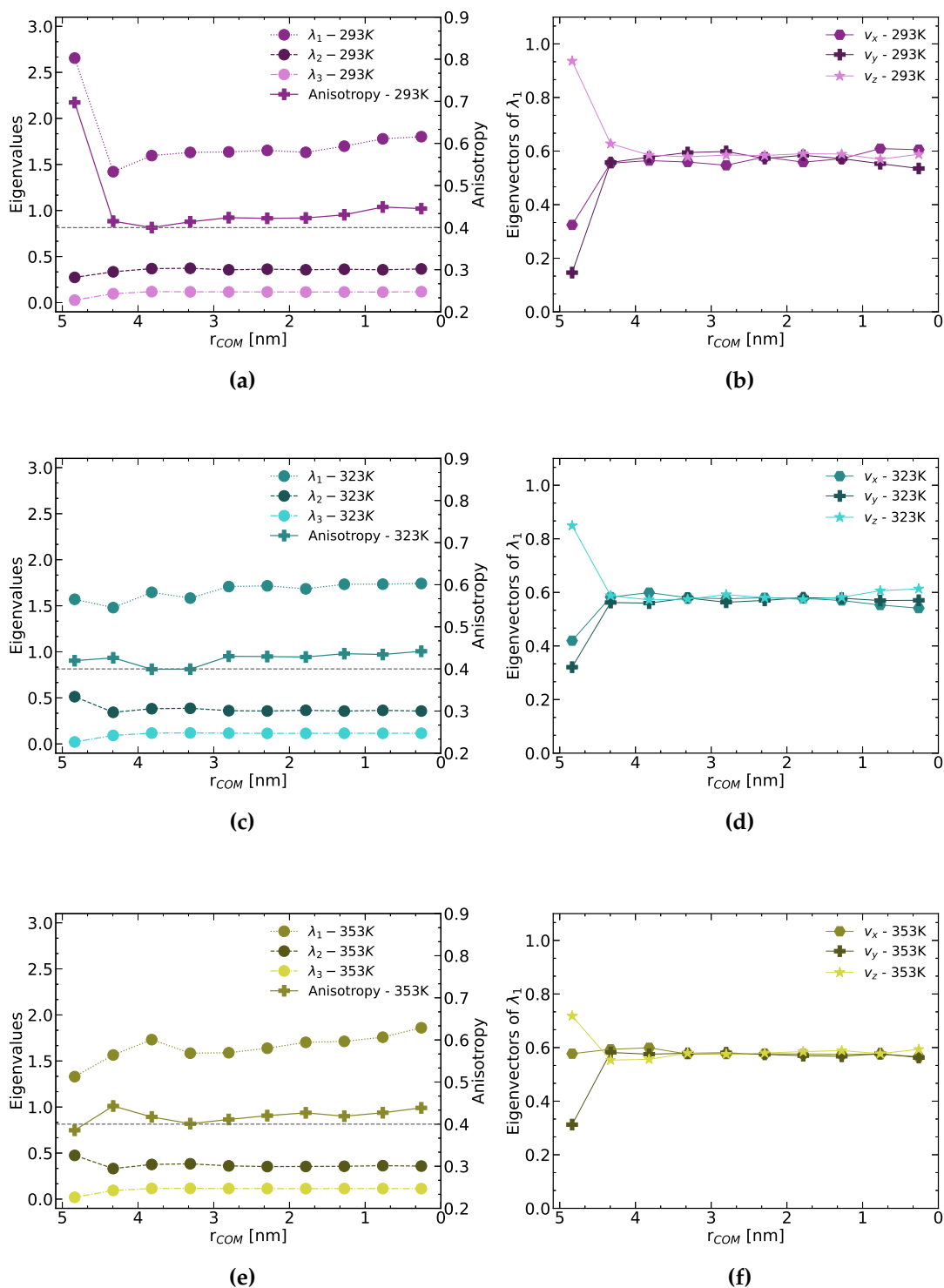


Figure 4.6: (a, c, e) show the eigenvalues of the gyration tensor representing the principal axes of the gyration ellipsoid for all three temperatures. The relative shape anisotropy and its bulk value (grey dashed lines) are also shown. The ratios of the eigenvalues are 1.0 : 0.21 : 0.068 for $T = 293$ K, 1.0 : 0.21 : 0.067 for $T = 323$ K and 1.0 : 0.21 : 0.067 for $T = 353$ K. (b, d, f) show the eigenvectors, indicating the orientation, of the largest eigenvalue λ_1 of the gyration tensor in cartesian coordinates. r , in both, is determined by the distance of the chain's center of mass from the pore wall.

Figure (4.7) shows snapshots of two chains with their COM away from the pore and another two with their COM close to the nanopore at $T=293\text{K}$ from two different perspectives: Figure (4.7a) is the view along \hat{e}_z (xy plane) and Figure (4.7b) is along \hat{e}_r . The snapshots expand on the results of the swelling and orientation of the chains at the pore wall for low temperatures.

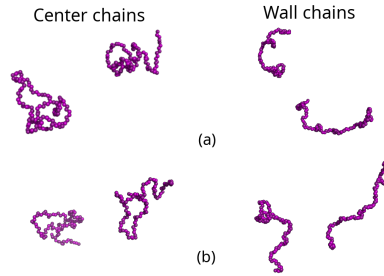


Figure 4.7: Snapshots of chains away from the pore wall (chains 123 and 127) and at the wall (chains 72 and 103) at $T=293\text{K}$. **(a)** is the view along \hat{e}_z (xy plane) and **(b)** along \hat{e}_r .

4.1.4 Nematic Order

The almost rod-like value of the anisotropy for chains with COM close to the wall ($\sim 2\text{\AA}$ from the wall) suggests that the chains are extended along the z-axis. In cylindrical confinement the chains oriented perpendicular to the radial direction can be either along \hat{e}_z or \hat{e}_φ ; however, the curvature effects here induce an alignment along the axial direction. The value of the anisotropy at the pore wall also suggests the possibility of nematic ordering in that layer. We proceed by calculating the nematic order tensor $Q_{\alpha\beta}$ (Eq.(4.6)) for the double bonds in the system. The tensor is given by,

$$Q_{\alpha\beta} = \frac{1}{N_{DB}} \sum_{n=1}^{N_{DB}} \frac{1}{2} (3\hat{b}_{n\alpha}\hat{b}_{n\beta} - \delta_{\alpha\beta}). \quad (4.6)$$

The system is divided into small bins across the nanopore, thus, $\hat{b}_{n\alpha}$, $\hat{b}_{n\beta}$ are the α , β components respectively of the unit vector \hat{b} along the CH double bond n . N_{DB} is the total number of double bonds whose COM is in the bin at time t . To quantify the nematic ordering, we calculate the order parameter S which is the largest eigenvalue of the tensor in Eq.(4.6). In the case of the double bonds being perfectly aligned with the z-axis, known as a prolate nematic

phase, $S = \mu_1 = 3/2(\hat{\mathbf{b}}_{nz}\hat{\mathbf{b}}_{nz}) - 1/2 \simeq 1$ and since the tensor $\mathbf{Q}_{\alpha\beta}$ is traceless then $\mu_2 = \mu_3 \simeq -1/2$ where $\mu_1 \geq \mu_2 \geq \mu_3$ are the eigenvalues of the tensor \mathbf{Q} .

A bin of thickness ~ 0.4 nm is comparable to the size of a united atom and is also the thickness of monomer layering. In that case, we would be considering double bonds which have at least one of their CH beads at the wall. However, for that bin size no ordering is present (as seen in Figure (4.8) for $T = 293$ K); therefore, we exclude the possibility of nematic ordering at the wall. If we consider a bin of size ~ 0.2 nm, which is as close as the double bonds can approach the nanopore wall, we are monitoring double bonds with both CH end beads in the first monomer layer. In a layer of this size, there is on average only one double bond at a given time t . Therefore, there isn't enough statistical data to construct any conclusions.

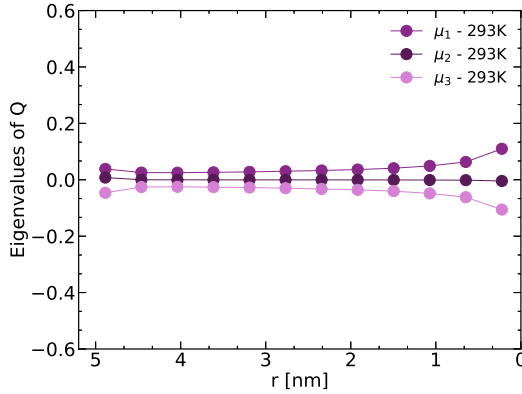


Figure 4.8: The eigenvalues of the nematic order tensor \mathbf{Q} at $T = 293$ K. The order parameter $S = \mu_1$ indicating no nematic ordering for a bin size of 0.4 nm.

In this section, we described the effects of cylindrical confinement on the structural properties of PBD. The confinement creates a layering effect in the density of the PBD's united atoms extending to around 2.5 nm away from the pore ($\sim 2R_g$). The first peak of the monomer density layering suggests that there is a significant amount of monomers "adsorbed" to the wall which we will address in the following section. In addition to the layering in the density profile, the confinement induces orientational ordering on both the segment and chain scale. On the segmental scale we deduce from studying the second Legendre polynomial of the angle between the double bonds and the radial and axial axes, that the double bonds near the walls prefer to be along the pore walls. For the

orientational ordering on the chain scale, the gyration tensor shows that the radius of gyration remains constant across the nanopore except for chains with centers of mass within the first monomer layer at the lowest temperature. The gyration ellipsoid of the chains shows that for the layer closest to the pore walls, the longest axis of the ellipsoid has its largest projection along the axis of the cylinder thus also preferring to lie perpendicular to the radial axis. In the following section, we investigate the effects of the confinement and geometry on the dynamics of the unentangled polymer system.

4.2 Dynamics across the nanopore

The change in polymer dynamics in nanocomposites has an impact on the properties of PNCs. For example, segmental dynamics affect certain mechanical properties such as stiffness and strength. Slower dynamics in the melt can result in an increase in the viscosity. Therefore, studying polymer dynamics in the bulk or in confinement can help in understanding and controlling the performance of certain PNCs.

The addition of NPs to produce nanocomposites can help with changing the properties and dynamics of the melt in a controlled manner [128–130]. The studies that have addressed the dynamics of melts in nanocomposites [32,65–67,69,72,120,131–134] mention the decrease in mobility of the monomers as they approach the surface of confinement. Namely, there is a slowing down of the dynamics in the layer adsorbed to the confinement walls until bulk-like behavior is later obtained as we move away.

The effects of cylindrical 2D confinement on polymer dynamics has been the subject of investigation by different techniques [13,34–36,38,40,41,63,135–137]. The results from these experimental techniques do not always coincide; therefore, a consolidated agreement on how the dynamics are affected by the pore has not been reached. The role of MD simulations in understanding the effects of confinement on dynamics is to provide a link between the microscopic molecular mechanisms and experimentally observed quantities. Several studies, using simulations, have tackled the dynamics affected by nanoparticles and thin films. On the other hand, not much simulations have addressed the effects of cylindrical confinement on chemically realistic polymer melts.

In this section we start by studying the mean squared displacement of both the monomers and chains in the system for different layers across the nanopore.

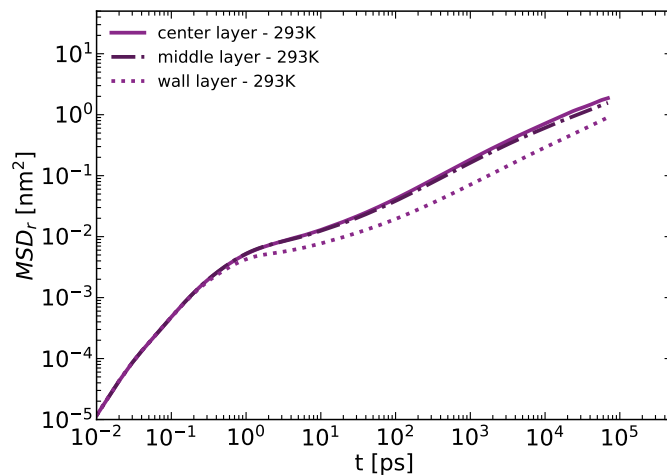
We observe the slowing down of the dynamics in both the axial and radial directions for the layer at the wall (size $\sim R_g$). For the incoherent neutron scattering function, a measurement accessible by experiments, we observe again the slowing down of the relaxation as well as a third step in the decay of the relaxation for the layer at the wall. By computing the adsorption autocorrelation function, we are able to connect this extra step in the relaxation to the adsorption/desorption process occurring at the wall layer due to the melt-wall interactions and augmented by the decrease in temperature. Finally, we investigate the segmental relaxation of *cis* and *trans* groups and the effect of the confinement on the potential experimentally obtained quantities such as the spin-lattice relaxation times T_1 .

4.2.1 Mean squared displacement (MSD)

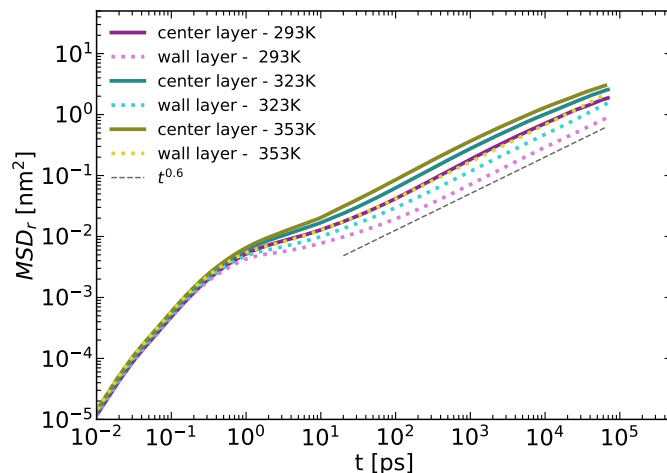
We start the dynamical analysis with the mean squared displacement (MSD) of the monomers in the system. The previous results (section 4.1) concerning the structural analysis show that on the monomer scale, the effects extend to a distance of $\sim 2R_g$ (valid for the chains in our system) away from the pore wall. Consequently, we choose to divide the system into three layers (slabs) of size $\approx R_g$ across the radial direction. The layers are defined such that $r_{max} - r_{min} = 1.695$ nm. A monomer belongs to a certain layer if its radial position is in that layer at $t=0$. We define our MSD as the displacement in the axial/radial positions of the monomers/chains,

$$MSD(t) = \frac{1}{N} \sum_{i=1}^N \langle |\mathbf{r}_i(t) - \mathbf{r}_i(0)|^2 \rangle. \quad (4.7)$$

Eq.(4.7) describes the deviation of the projection of particle i on $\hat{\mathbf{e}}_z$ or $\hat{\mathbf{e}}_r$ over time with respect to its initial position at $t = 0$. At very short time scales, the monomers in an unentangled polymer melt show typical ballistic dynamics ($MSD \sim t^2$) and their movement is independent of chain connectivity (similar to entangled melts). Beyond a specific characteristic time denoted by τ_0 , the MSD follows Rouse scaling [138] with a predicted $MSD \sim t^{1/2}$. At longer time scales monomer diffusion is expected with MSD directly proportional to time $\sim t$.



(a)



(b)

Figure 4.9: (a) Monomer mean squared displacement (MSD) for three layers across the radial direction of the melt at $T=293\text{K}$. (b) Monomer MSD for the center layer (full lines) and wall layer (dotted lines) across the radial direction for three different temperatures. The dashed grey line is the Rouse-like behavior.

Figures (4.9a) and (4.9b) show the MSD across the radial direction for three layers and the MSD for the center most layer (full lines) and the pore wall layer (dotted lines) for all three temperatures respectively. The displacement crosses from a vibrational dominant behavior ($\sim t^2$) to a Rouse like behavior as expected at around 1 ps. From Figure (4.9a) we can deduce that along the radial direction, the motion in the wall layer is slower than in the other two layers in the system.

The plots for $T = 323$ and 353 K can be found in Figures (B.3) and (B.4) respectively in Appendix (B). The same behavior is present at all three temperatures with the motion in all layers being slower for lower temperatures. Moreover, the crossover between the vibrational dominant behavior and the relaxational one is more prominent for the layers at the wall as seen in Figure (4.9b). For longer time scales, the radial displacement is expected to reach a plateau as $\Delta r = \sqrt{(MSD_r)}$ approaches 5 nm (radius of the nanopore).

For the displacement along the axial direction, as seen in Figure (4.10), the wall effect extends to the motion of the monomers in that direction as well, and the motion at the interface is slower than that at the center of the nanopore. This displacement also shows the time scale separation between vibrational and relaxational motions setting in at around 1 ps as observed for the radial motion. The expected diffusive motion along the axial direction has not set in yet which is in agreement with the behavior of bulk PBD found in the literature [99] as well as the monomer MSD behavior for PBD between graphite walls [22]. The dashed grey line represents the Rouse-like behavior while the dotted grey line is set to calculate later on a characteristic relaxation time τ_{mon} .

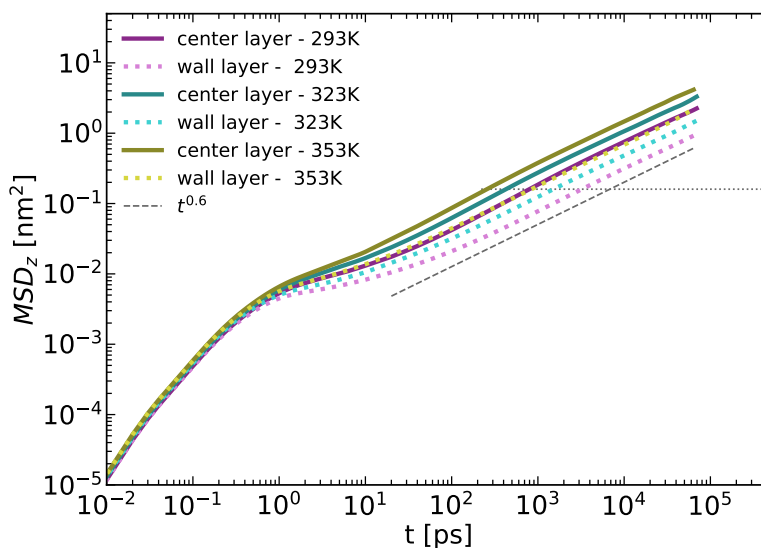


Figure 4.10: Monomer MSD for the center layer (full lines) and wall layer (dotted lines) across the axial direction for three different temperatures. The dashed grey line is the Rouse-like behavior. The dotted grey line is set to calculate a characteristic relaxation time τ_{mon}

Neutron scattering experiments [13] of a Polyethylene oxide melt confined in

alumina pores also state that the confinement affects the direction perpendicular to the pores in a more pronounced way. Other simulations [39,127] of coarse grained models of entangled melts in cylindrical confinement show that the confinement affects the motion in the radial direction more than axial direction. On the other hand, Ref [39] notes that for entangled chains the lateral diffusion in a cylindrical confinement is faster when compared to the bulk. Our results show that the motion in both directions is affected significantly when compared to the rest of the melt as well as the bulk behavior.

The motion of the COM of the chains is also affected by the confinement which was also observed in previous studies on PBD in confinement [23]. To visualize this, Figure (4.11) shows the trajectory of the COM for chains with their COM starting at the center of the nanopore and for chains with COM starting at the wall. The motion of the chains with COM starting in the bulk-like region covers a distance of length scale close to the radius of the nanopore. On the other hand, for the chains at the wall, the motion is highly restricted and the chains' centers of mass appear to never leave the first layer. This also further supports our observation that there exists an adsorbed layer of monomers at the polymer-pore interface.

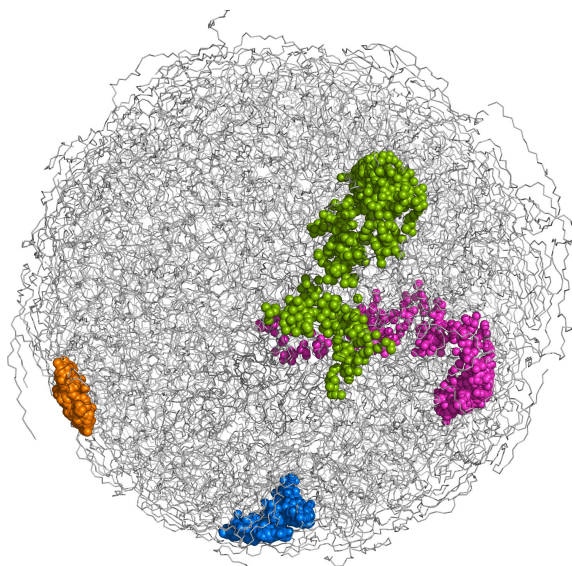


Figure 4.11: Chain center of mass (COM) trajectory ($T = 293$ K) for two chains with COM starting at the wall (99-blue and 258-orange) and two chains with COM starting in the center of the pore (14-green and 188-magenta). The trajectory is taken over 410 ns and 820 frames and an interval of 500 ps between each point. The centers of mass were translated along the z-direction for a clearer visualization. Each bead represents the COM of the chain at time t .

Figure (4.12) shows the chain center of mass MSD for both the radial and axial directions.

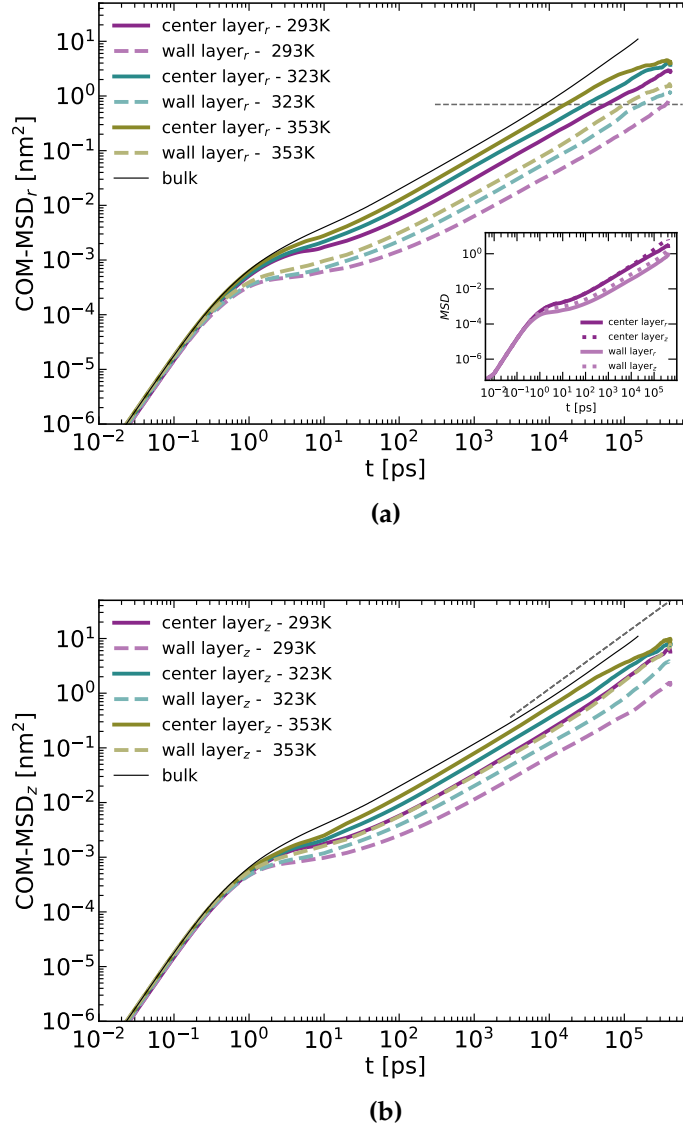


Figure 4.12: The center of mass (COM) mean squared displacement in the melt. **(a)** shows the MSD along the radial direction for wall and center layers at three temperatures. The inset shows the difference between the radial and axial MSD at $T = 293$ K and the dashed line is at $R_p^2/3$ that we define later as the characteristic time τ_R . **(b)** displays the COM MSD along the axial direction for the wall and center layers. The dashed grey line has a slope of 1 corresponding to diffusive behavior and the black solid line is the bulk MSD [45].

After the ballistic regime (t^2), the chain dynamics, similar to the monomer dynamics, are slowed down at the interface due to the attractive interaction between the cylindrical pore and the melt. The plateau of the first time scale separation becomes stronger for the layer at the wall and for lower temperatures especially along the radial direction in Figure (4.12a). The motion of the chains along the axial direction is also affected but to a slightly lesser effect. The inset of Figure

(4.12a) shows that the dynamics of the chains in the center most layer in the melt is similar in both directions; however, as we approach the wall the motion along \hat{e}_r is slower. Diffusive behavior would show a linear dependence of the displacement on time and is only applicable along the axial direction \hat{e}_z which is shown as the grey dashed line in Figure (4.12b).

Even though the displacement at higher temperatures and for the center layer seems to start to exhibit diffusion, the statistics at these time scales for our simulation are not good enough to make a definite statement. The motion in the center most layer in both plots is not as affected by the pore as the wall layer; however, it is still slower than the bulk behavior shown in the black solid line.

Table 4.1: The values of τ_{mon} and τ_R calculated from the monomer and COM displacements respectively. The values correspond to three different layers across the nanopore for both the axial and radial motions at all three temperatures.

	τ_{mon} [ps]					
	Radial			Axial		
	L1 ^a	L2 ^b	L3 ^c	L1	L2	L3
293 K	800	970	3 720	790	890	3 220
323 K	420	500	1 660	420	460	1 510
353 K	260	300	920	250	280	840
	τ_R [ps]					
	Radial			Axial		
	L1	L2	L3	L1	L2	L3
293 K	57 290	124 590	356 550	38 470	53 890	189 400
323 K	30 540	60 260	168 200	23 250	27 770	85 970
353 K	16 250	35 870	102 240	13 160	16 100	43 890

^a L1 corresponds to the layer at the center of the pore.

^b L2 corresponds to the intermediate layer.

^c L3 corresponds to the layer closest to the pore walls.

For a more quantifiable approach, we define a characteristic time τ_{mon} where $\langle MSD_{mon}(\tau_{mon}) \rangle = \sigma^2$ (σ is the approximate size of the united atom) and another characteristic time τ_R defined by $\langle MSD_{COM}(\tau_R) \rangle = R_g^2/3 \simeq 0.7 \text{ nm}^2$. Table (4.1) shows τ_{mon} and τ_R for all layers in both the axial and radial directions for all three temperatures. The values of τ_{mon} for both directions are comparable, with the radial direction slightly larger, the difference is smaller for higher temperatures.

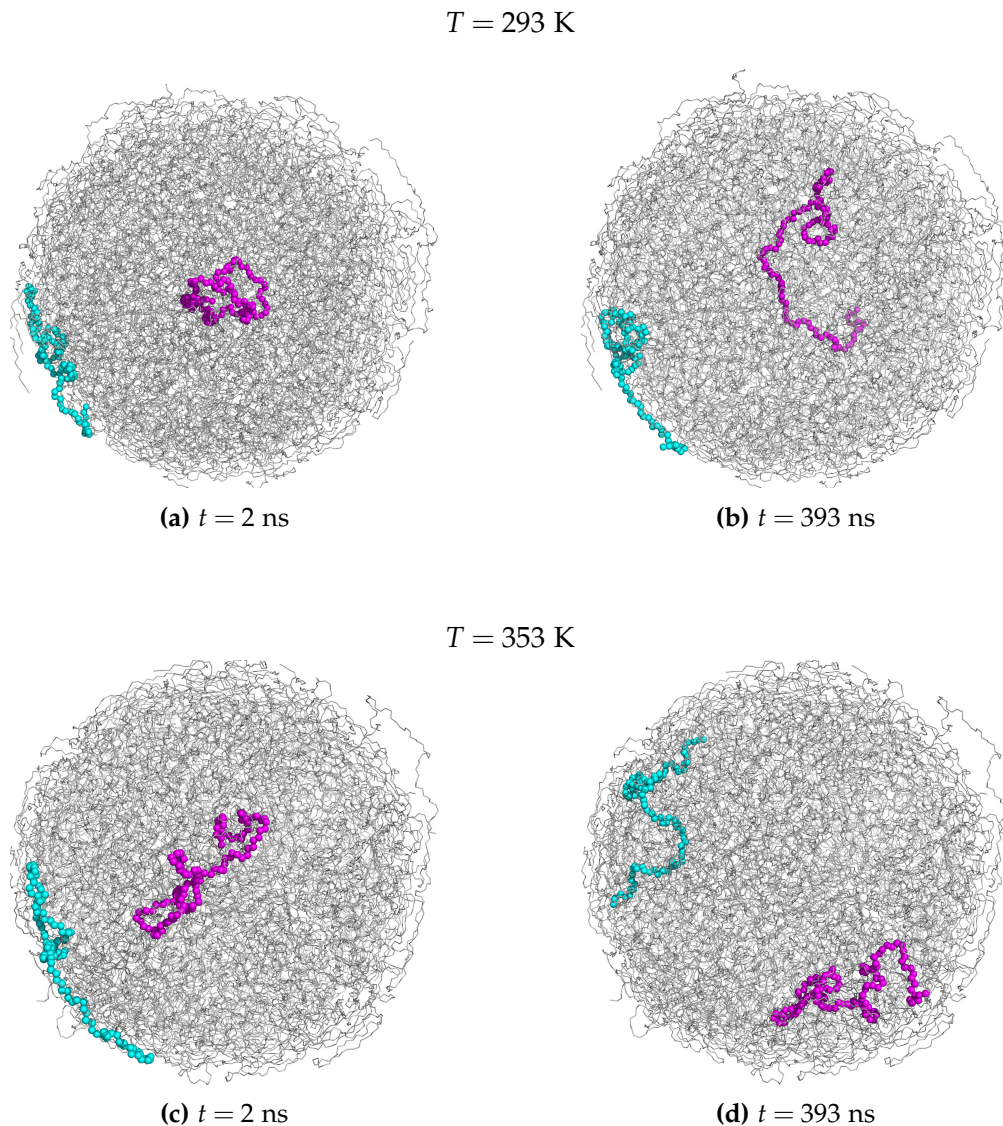


Figure 4.13: Snapshots of two chains at $t = 2 \text{ ns}$ (a and c) and at $t = 393 \text{ ns}$ (b and d). The snapshots are at two different temperatures: **a,b** $T = 293 \text{ K}$ for chain 14 at the center and chain 258 at the wall and **c,d** $T = 353 \text{ K}$ for chain 250 at the center and also chain 258 at the wall. The chains were translated along the z-direction for a clearer visualization.

The time it takes the monomers and chains to travel a distance of their own size increases with the decrease in temperature and as we move closer to the pore wall. τ_R , obtained from the COM displacement, can be compared to the results of simulations of a PBD melt between graphite walls [45]. For the displacement parallel to the graphite surface at the wall (L3) at $T = 353 \text{ K}$, $\tau_{R\parallel}^{L3}(\text{walls}) = 15 \text{ ns}$ compared to $\tau_{R\parallel}^{L3}(\text{pore}) = 43 \text{ ns}$ for this system which shows much slower motion in that layer. The graphite walls value is more comparable to the intermediate layer in the pore system with $\tau_{R\parallel}^{L2}(\text{pore}) = 16 \text{ ns}$. As for the dis-

placement perpendicular to the confining walls, the results are similar, with $\tau_{R_{\perp}}^{L3}(walls) = 39$ ns for the flat wall geometry whereas our cylindrical geometry results in $\tau_{R_{\perp}}^{L3}(pore) = 102$ ns while $\tau_{R_{\perp}}^{L2}(pore) = 36$ ns. The calculations of characteristic time for the bulk at $T = 353$ K [45] shows that $\tau_R(bulk) = 9$ ns $<$ $\tau_{R_{\parallel}}^{L1}(pore) = 13$ ns where bulk-like behavior can be expected. A valid explanation for this is the fact that the density in the center ($\rho_{center}^{353K} = 884$ kg/m³) is slightly larger than the bulk density at $T = 353$ K allowing for a slightly slower motion in the center.

Figure (4.13) shows two snapshots of two chains, one starting at the layer close to the confining pore wall and the other starting at the center of the pore, at $T = 293$ K and $T = 353$ K. The snapshots were taken at two different times where Figure (4.13a) and Figure (4.13c) are at $t = 2$ ns and Figure (4.13b) and Figure (4.13d) at $t = 393$ ns. The same wall chain (258) was chosen for both temperatures while for the center of the pore, chain 14 is chosen for $T = 293$ K and chain 250 for $T = 353$ K. While the chains in the center move freely across the nanopore, the chains at the wall exhibit different behaviors at the two temperatures. At $T = 353$ K, the wall chain starts adsorbed to the pore wall and manages to desorb and to escape the first layer. However, the same chain at a lower temperature is adsorbed to the pore wall at the beginning of the simulation and remains in that state after around 400 ns. The time scale of the desorption process at $T = 293$ K is larger than our simulation time and we are unable to see the chains directly at the wall desorb and move away from the wall. This effect is expected to get stronger as we go to lower temperatures and affects the extent of the "deformation"/extension (already observed in Figure (4.5) and Figure (4.6) at $T = 293$ K) and slowing down of the dynamics as a result of the cylindrical confinement. This behavior may give rise to the observation of residual orientational order in NMR experiments [139].

4.2.2 Adsorption Autocorrelation Function

In section 4.1.1 we mentioned that the density profile suggests the existence of an adsorbed layer of monomers at the wall. The MSD calculations show the implication of the adsorption/desorption kinetics on the motion of the monomers and chains particularly at the pore-melt interface. To quantify these adsorption/desorption kinetics we calculate the correlation function (eq. (4.8)), where $s(t) = 1$ if the monomer is adsorbed, i.e., if it is in the first layer of the density

profile, at time t and $s(t) = 0$ otherwise.

$$\Phi(t) = \frac{\langle s(t)s(0) \rangle - \langle s \rangle^2}{\langle s(0)s(0) \rangle - \langle s \rangle^2} = \frac{\langle s(t) \rangle - \langle s \rangle^2}{1 - \langle s \rangle^2} \quad (4.8)$$

To identify the monomers we choose the chains whose centers of mass belong to the bin of size $\approx R_g$ (length scale of COM density profile) at $t = 0$, then the adsorbed monomers are those that belong to the latter chains and whose position is in the first layer at the wall with a thickness of ≈ 0.5 nm. Accordingly, $s(0) = 1$ which results in $\Phi(0) = 1$. Then $\Phi(t)$'s definition is based on geometric criteria i.e. whether the monomers of a chain whose center of mass is at a radial distance $\sim R_g$ are themselves at a distance ~ 0.5 nm away from the pore wall.

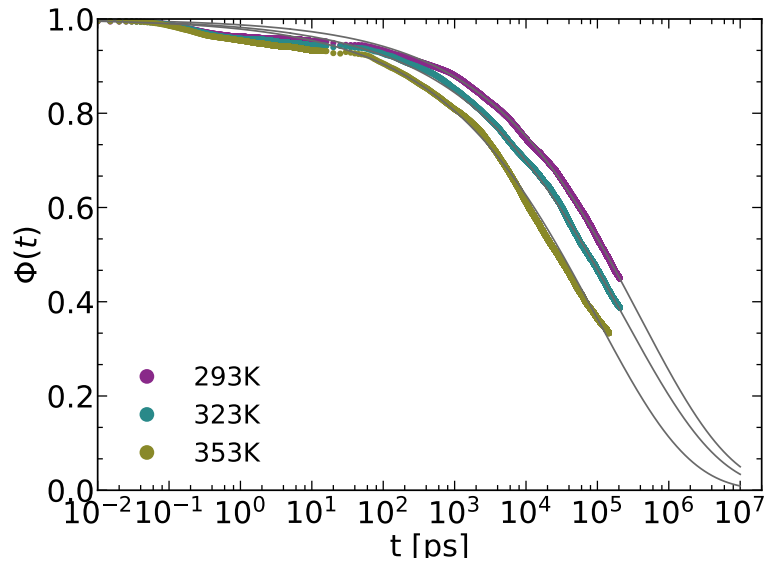


Figure 4.14: The adsorption autocorrelation function $\Phi(t)$ for all three temperatures. The grey solid lines represent the fits to the stretched exponential in eq.(4.9).

It is also good to note that the decay of the correlation function with time presents information on the time scale of the monomer desorption. Consequently we assign a relaxation time τ corresponding to the relaxation process where τ is obtained by fitting the autocorrelation function $\Phi(t)$ to a stretched exponential. β in the following equation is the stretching exponent,

$$F_s(q_r, t) = A \exp \left[- \left(\frac{t}{\tau} \right)^\beta \right]. \quad (4.9)$$

The prefactor A is set to 1 given that $\Phi(0) = 1$ and the fitting parameters can be found in Table (4.2). Figure (4.14) shows the autocorrelation function for all three temperatures as well as the respective fits to the stretched exponential. However, to better understand these results, we study them along with the calculations of the incoherent scattering function in the following subsection.

4.2.3 Incoherent Neutron Scattering Function

In neutron scattering experiments, the scattering of neutrons is a result of the interactions between the neutrons and the atomic nuclei. The scattering is characterized by b which is known as the scattering length. The double differential scattering cross section defined as,

$$\frac{\partial^2 \sigma}{\partial \Omega \partial E} \quad (4.10)$$

is the number of neutrons scattered between an angle Ω and $\Omega + d\Omega$ and have a change in energy defined as $\Delta E = \hbar\omega$ compared to the total number of initial incident neutrons. If there is no change in the energy between the incident and scattered neutrons ($\hbar\omega = 0$) the scattering is elastic and monitors the changes in the momentum transfer $\mathbf{q} = \mathbf{k}_f - \mathbf{k}_i$ (\mathbf{k}_f and \mathbf{k}_i are the scattered and incident wavevectors respectively) only. This type of scattering can also be referred to as neutron diffraction and is beneficial when studying structural information only. If the neutron has led to an excitation in the sample, then $\hbar\omega \neq 0$ and the scattering is defined as inelastic. The latter measures scattered neutrons as a function of both the momentum transfer and energy which results in information on the structure and the dynamics of the sample.

The double differential scattering cross section in Eq.(4.10) contains an incoherent and a coherent part as follows,

$$\begin{aligned} \frac{\partial^2 \sigma}{\partial \Omega \partial E} &= \left(\frac{\partial^2 \sigma}{\partial \Omega \partial E} \right)_{Coh} + \left(\frac{\partial^2 \sigma}{\partial \Omega \partial E} \right)_{Inc} \\ &\propto \left[\sum_{i,j} S_{ij}^{Coh}(\mathbf{q}, \omega) + \sum_i S_i^{Inc}(\mathbf{q}, \omega) \right]. \end{aligned} \quad (4.11)$$

The coherent part is a result of the interference between scattered neutron waves from different scattering centers where a collective behaviour of the atoms can be studied while the incoherent part is present when there is no interference between the scattered neutron waves and thus follows a single atom in time. In Eq.(4.11) the indices i and j run over different atoms where $S_{ij}^{Coh}(\mathbf{q}, \omega)$ is the coherent scattering function involving different atoms and $S_i^{Inc}(\mathbf{q}, \omega)$ is the incoherent scattering function of atom i . Since we would like to study the single atom motion in time we will from here on consider only the incoherent scattering function which can be written as,

$$S_{Inc}(\mathbf{q}, \omega) = \frac{1}{2\pi} \int_{-\infty}^{\infty} F(\mathbf{q}, t) \exp(i\omega t) dt. \quad (4.12)$$

$F(\mathbf{q}, t)$ is called the intermediate incoherent neutron scattering function and gives information on the translational motion of the atoms in the system and is defined as,

$$F(\mathbf{q}, t) = \frac{1}{N} \sum_{i=1}^N \left\langle \exp \left\{ -i\mathbf{q} \cdot [\mathbf{r}_i(t) - \mathbf{r}_i(0)] \right\} \right\rangle \quad (4.13)$$

where $\mathbf{r}_i(t)$ is the position vector of scattering center i at a time t (the scattering centers in our system are the united atoms), \mathbf{q} is the scattering wave vector also called the momentum transfer, N is the total number of atoms in the layer or the system and the angular brackets denote the thermodynamic average. We are interested in two alignments of \mathbf{q} : along $\hat{\mathbf{e}}_z$ and $\hat{\mathbf{e}}_r$. In experiments this is attainable by rotating the sample at 45° (momentum transfer perpendicular) and 135° (momentum transfer parallel) to the incident beam with a scattering angle of 90° . For both cases of the analytical expression, let us annotate $\mathbf{r}_i(t) - \mathbf{r}_i(0) = \mathbf{R}$.

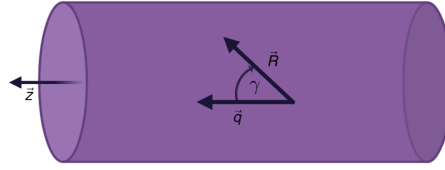
Case 1: \mathbf{q} along $\hat{\mathbf{e}}_z$


Figure 4.15: A sketch of the cylinder showing the momentum transfer \mathbf{q} aligned along the axial direction. \mathbf{R} is the vector connecting monomer i at times 0 and t and γ is the angle formed between \mathbf{R} and \mathbf{q} .

Aligning \mathbf{q} with $\hat{\mathbf{e}}_z$ would result in information concerning the motion along the axial direction of the cylinder. Starting from Eq.(4.13) and denoting the momentum transfer as \mathbf{q}_z we get,

$$F_s(\mathbf{q}_z, t) = \frac{1}{N} \sum_{i=1}^N \left\langle \exp(-i\mathbf{q}_z \mathbf{R}) \right\rangle = \left\langle \frac{1}{N} \sum_{i=0}^N \exp(-iqR \cos(\gamma)) \right\rangle \quad (4.14)$$

where γ is the angle between \mathbf{R} and \mathbf{q}_z as seen below in Figure (4.15). Since the momentum transfer is along \mathbf{z} then $R \cos(\gamma) = Z = z_i(t) - z_i(0)$ is the projection of \mathbf{R} along the z -axis. The intermediate scattering function becomes,

$$F_s(\mathbf{q}_z, t) = \frac{1}{N} \sum_{i=0}^N \left\langle \exp(-iqZ) \right\rangle. \quad (4.15)$$

Taking both directions of \mathbf{q}_z into consideration we obtain,

$$\begin{aligned} F_s(q_z, t) &= \frac{1}{N} \sum_{i=1}^N \left\langle \left[\cos(q_z Z) + i \sin(q_z Z) + \cos(-q_z Z) + i \sin(-q_z Z) \right] \right\rangle \\ &= \frac{1}{N} \sum_{i=1}^N \left\langle \left[\cos(q_z Z) + i \sin(q_z Z) + \cos(q_z Z) - i \sin(q_z Z) \right] \right\rangle \end{aligned}$$

and finally,

$$F_s(q_z, t) = \frac{2}{N} \sum_{i=1}^N \left\langle \cos [q_z(z_i(t) - z_i(0))] \right\rangle. \quad (4.16)$$

Case 2: \mathbf{q} perpendicular to $\hat{\mathbf{e}}_z$

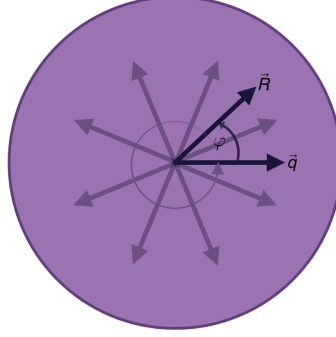


Figure 4.16: A sketch of the cylinder showing the momentum transfer \mathbf{q} perpendicular to the axis of the cylindrical pore. \mathbf{q}_r then can take different directions (faded purple arrows) and exists in the xy -plane. \mathbf{R} is the vector connecting monomer i at times 0 and t and φ is the angle formed between \mathbf{R} and \mathbf{q} . Note that the source of the incident neutrons is not at the origin and that \mathbf{R} is not the radial position and was sketched at the origin to simplify the diagram.

To get information on the motion along the radial direction of the pore, \mathbf{q} should be perpendicular to the pore axis as seen in Figure (4.16). Starting again with Eq.(4.13) where we define $\mathbf{R} = \mathbf{r}_i(t) - \mathbf{r}_i(0)$ and φ to be the angle between \mathbf{q} and \mathbf{R} we get,

$$F_s(\mathbf{q}_r, t) = \frac{1}{N} \sum_{i=1}^N \left\langle \exp(-iq_r R \cos \varphi) \right\rangle. \quad (4.17)$$

To get an average over all possible values of φ which can also be expressed as all possible directions of \mathbf{q} where the latter is in the xy -plane, an integration over the angle φ is needed and the integral form is,

$$F_s(q, t) = \frac{1}{N} \int_0^{2\pi} \exp(-iqR \cos \varphi) d\varphi$$

$$F_s(q, t) = \frac{1}{N} \int_0^{2\pi} \cos(qR \cos \varphi) d\varphi + i \frac{1}{N} \int_0^{2\pi} \sin(qR \cos \varphi) d\varphi \quad (4.18)$$

$$= \frac{1}{N} \int_0^{2\pi} \cos(qR \cos \varphi) d\varphi. \quad (4.19)$$

The imaginary part of Eq.(4.18) is zero and Eq.(4.19) is a Bessel function of the first kind with the proof below. The integral representation of the Bessel function is,

$$J_n(x) = \frac{1}{\pi} \int_0^\pi \cos(n\theta - x \sin \theta) d\theta. \quad (4.20)$$

For $n = 0$ and the fact that $\cos(-x) = \cos(x)$ we get,

$$J_0(x) = \frac{1}{\pi} \int_0^\pi \cos(x \sin \theta) d\theta.$$

We then apply a change of variable where $\varphi = \frac{\pi}{2} - \theta$

$$\begin{aligned} J_0(x) &= \frac{1}{\pi} \int_{\pi/2}^{-\pi/2} \cos [x \sin(\pi/2 - \varphi)] d\varphi \\ &= \frac{1}{\pi} \int_{-\pi/2}^{\pi/2} \cos(x \cos \varphi) d\varphi \\ &= \frac{1}{\pi} \int_0^\pi \cos(x \cos \varphi) d\varphi \\ &= \frac{1}{2\pi} \int_0^{2\pi} \cos(x \cos \varphi) d\varphi. \end{aligned} \quad (4.21)$$

Now we can write the intermediate scattering function in terms of the Bessel function where $x = q_r R$,

$$F_s(q_r, t) = \frac{2\pi}{N} J_0(q_r R). \quad (4.22)$$

Similar to the mean squared displacement, we divide the pore into three bins

of the same size along the radial direction and a monomer is considered to belong to a certain layer if its position is in that layer at $t = 0$. To get a more detailed look at the scattering function for all three temperatures we plot in Figure (4.17)² the wall and center layers for \mathbf{q}_r (solid and dotted lines respectively) and only the wall layer for \mathbf{q}_z (dashed lines). As observed from the mean squared displacement, the motion in both directions is affected by the confinement. As the temperature decreases, the motion of the monomers is slowed down and the same is observed as we get closer to the pore wall. At around 1 ps there is the first time scale separation between the vibrational and relaxational processes that gets stronger for lower temperatures. The amplitude of the vibrational decay is dependent on the value of the momentum transfer as we will see later in Figure (4.19). The plateau observed here that increases in height and extends in time as we decrease the temperature is due to packing and dihedral barriers. In comparison with the monomer MSD, the change of the time scale separation with temperature is seen more clearly from the scattering function.

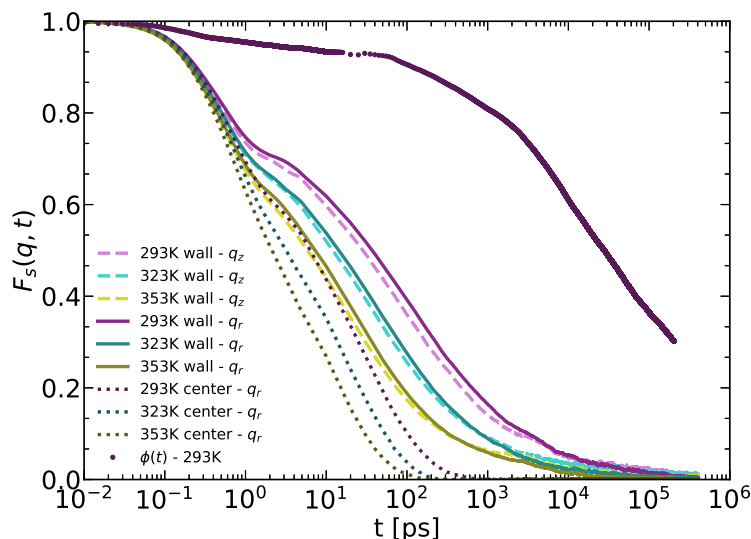


Figure 4.17: The incoherent neutron scattering function (INSF) for monomers at the center (dotted lines - \mathbf{q}_r) and the monomers at the pore layer (solid for \mathbf{q}_r and dashed for \mathbf{q}_z) with $q_r = q_z = 12 \text{ nm}^{-1}$. $\Phi(t)$ is the adsorption autocorrelation function defined in eq.(4.8) for the lowest temperature $T = 293 \text{ K}$.

An important detail the MSD doesn't show us so clearly, is the fact that the relaxational process is split into two for the layer at the wall. This is a re-

²For all the plots of the scattering function, the plotted $F_s(q, t)$ is in fact $F_s(q, t)/2\pi$

sult of an additional slow process of the desorption of monomers/chains at the wall as shown by the adsorption autocorrelation function $\Phi(t)$ (see subsection 4.2.2) included in Figure (4.17) for the lowest temperature $T = 293$ K. The second crossover in the incoherent scattering function occurs at the end of the plateau regime in $\Phi(t)$ at around 1 ns and indicates that the monomers (also chains given the criteria upon which we define adsorption) have started the desorption process. This has been previously observed and reported by Yelash et Al. [22] for simulations of PBD on graphite. Neutron scattering experiments on Polythylene oxide (PEO) confined in alumina pores [13] describe an anisotropic slowing down of the dynamics due to the confinement. This slowing down is more prominent in the results on the direction perpendicular to the pore walls.

The scattering function in Figure (4.17) shows us results for different layers that are only reachable through simulations. The observation of the three-step decay seen for the layer at the wall is not obtainable from experiments. We then proceed to calculate the scattering function that is accessible and could be measured by experiments. We consider a scattering geometry with the momentum transfer perpendicular to the confining pore wall; however, the scattering function is calculated for all the layers in the pore combined (average of all the monomers across the 5 nm radius).

Figure (4.18) shows the incoherent neutron scattering function of all the monomers in the system for a momentum transfer $\mathbf{q}_r = 12 \text{ nm}^{-1}$ (value chosen is close to the first peak of the structure factor of the PBD melt) for all three temperatures. For comparison, the figure also contains the center most layer at $T = 353$ K and the wall layer at $T = 293$ K. In this case, the third step in the decay is still visible even for an average over all the monomers in the system. This was also observed for the parallel wall confinement. The amplitude of the plateau for the first time scale separation is reduced and the extra third-step is shifted slightly to lower times. These results show the extent of the effect of confinement on the melt as a whole and can be compared to experimental results on PEO in alumina nanopores [13]. In the latter, they studied the motion perpendicular to the wall for the whole melt and they attribute the slowing down to $\sim 10\%$ of the segments in the melt that are within ~ 1 nm away from the pore wall. In the mentioned paper, they question the length scale of the effect of the confinement on the melt, a point which we were able to address by studying different layers. So far, from both the structural and the dynamical results, we have observed that the effects start to decrease after a length scale of R_g for our polymer melt.

Moreover, Fig.(4.18) predicts that the experiments on PBD confined in alumina nanopores will show the mentioned third step in the final $\sim 20\%$ of the decay.

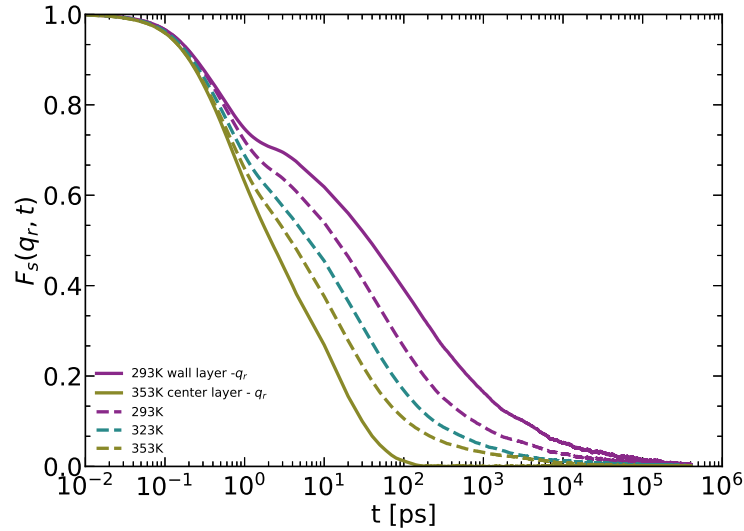


Figure 4.18: The incoherent scattering function of all the monomers in the system for a momentum transfer $\mathbf{q}_r = 12 \text{ nm}^{-1}$ for all three temperatures. The solid green line shows the center most layer at $T = 353 \text{ K}$ and the solid purple line shows the wall layer at $T = 293 \text{ K}$ for comparison.

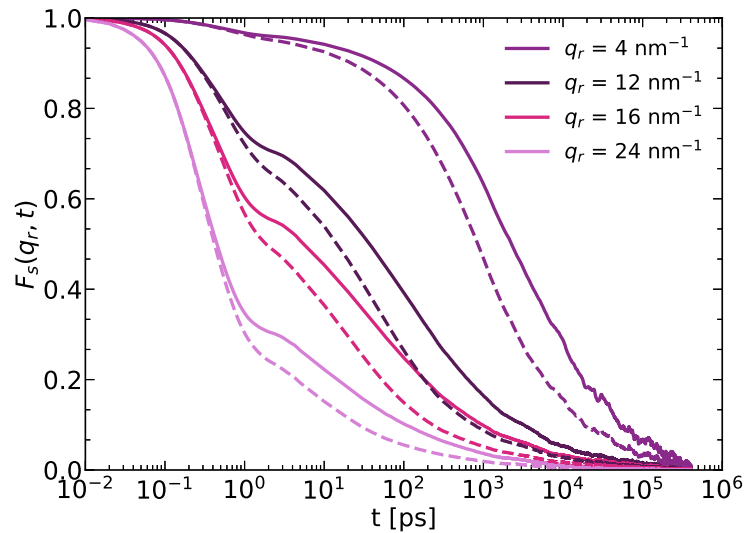


Figure 4.19: The INSF at $T = 293 \text{ K}$ for the monomers in the wall layer (solid) and averaged over all monomers (dashed) for different values of the momentum transfer \mathbf{q}_r .

Figure (4.19) displays the scattering function for the monomers in the layer at the wall (solid lines) and for all the monomers in the system (dashed lines) for different values of the momentum transfer directed perpendicular to the pore wall (\mathbf{q}_r) at $T = 293$ K (The plots for $T = 323$ and 353 K can be found in Appendix (B)). This is closer to the format obtained by Krutyeva et al. experimentally [13,41]. For large momentum transfers ($\mathbf{q}_r = 16 \text{ nm}^{-1}$ and $\mathbf{q}_r = 24 \text{ nm}^{-1}$), as seen in Figure (4.19), the vibrational regime dominates and detecting the additional process due to desorption kinetics becomes more difficult.

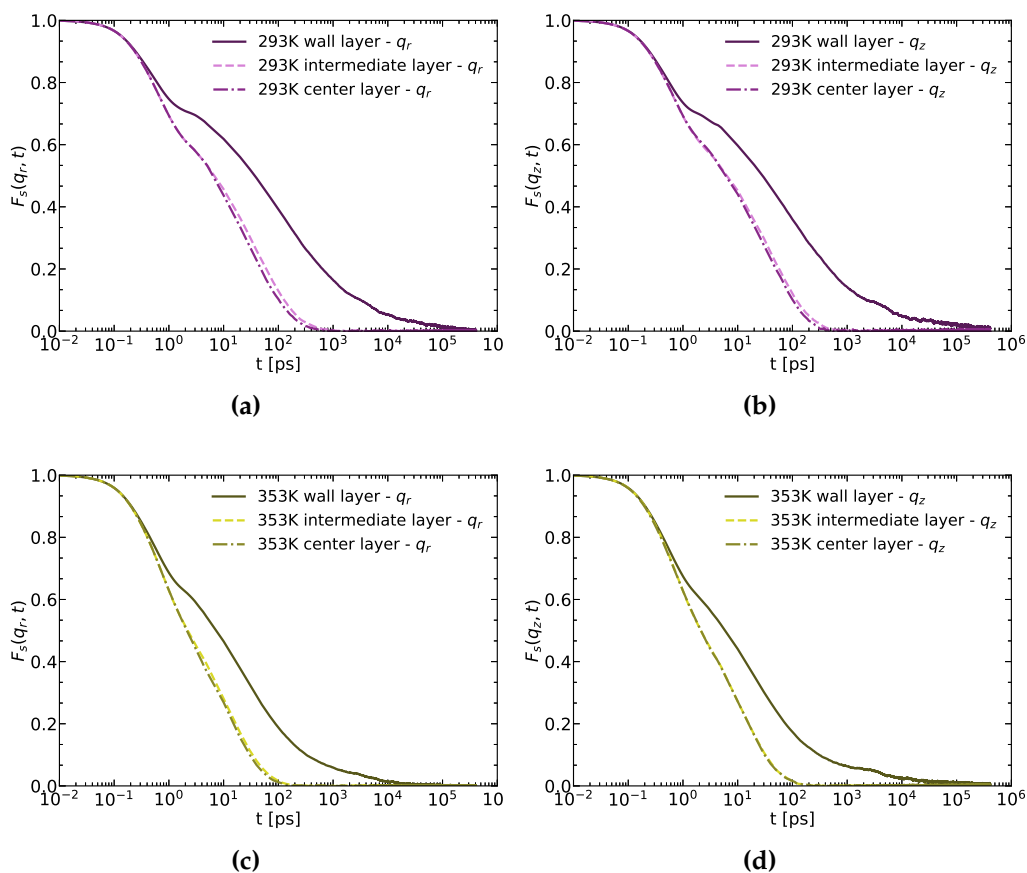


Figure 4.20: The (INSF) at $T = 293$ K and $T = 353$ K with momentum transfer $q_r = 12 \text{ nm}^{-1}$ (a,c) and $q_z = 12 \text{ m}^{-1}$ (b,d).

As for the momentum transfer $\mathbf{q}_r = 4 \text{ nm}^{-1}$, the vibrational regime is almost not visible while the desorption at the wall time window is much larger and stretches over the scattering function. Comparing our results to the studies on PEO in alumina pores [13], we claim that the "slow fraction" discussed in the experiments can be attributed to the desorption process at the wall which cannot

yet be observed given the time scales of the experiments.

If we take a look back at the scattering function for different layers across the pore, we could consider how the effect of the wall is weakened as we move towards the center. Figure (4.20) shows the INSF at $T = 293$ K and $T = 353$ K for both orientations of the momentum transfer. The desorption process is only present for monomers with their initial radial position in the layer at the wall. For the highest temperature $T = 353$ K, which is almost $\sim 2T_g$ (T_g is the glass transition temperature), bulk like behaviour is restored when we are in the intermediate layer with $r \lesssim 3.2$ nm (r being the radial distance from the center of the pore). While for the lower temperature of $T = 293$ K for both the intermediate and center layer there is a slight slowing down of the α -process that eventually gets stronger for the wall layer. The characteristic length of the α -relaxation process extends as we decrease the temperature and move towards the glass transition temperature. The temperature dependence of the length scale of the α -relaxation times has been addressed before for several coarse-grained model studies [60,140–144]. This effect could be a combination of the rotational barriers as well as the cage effect. For the latter, a "cage" is formed by a monomer's neighbors due to packing especially at the wall; therefore, it is often discussed that if a monomer is to escape the "cage", a collective rearrangement of several particles in its vicinity is needed.

The incoherent neutron scattering function in the center and at the wall can be fitted to a stretched exponential and a superposition of two stretched exponentials respectively to get a more quantitative idea about the relaxation process. The inner most layer in the center as well as the adsorption autocorrelation function (shown in subsection (4.2.2)) are fitted to a single stretched exponential. The superposition of two stretched exponentials is defined by,

$$F_s(q_r, t) = A_0 \left[X \exp\left\{-\left(t/\tau_\alpha\right)^{\beta_\alpha}\right\} + (1 - X) \exp\left\{-\left(t/\tau_{des}\right)^{\beta_{des}}\right\} \right]. \quad (4.23)$$

The first part of the right hand side of Eq.(4.23) describes the α -relaxation with X defined as the contribution of the α -relaxation to the total relaxation while $1 - X$ is its counterpart in the second term of Eq.(4.23) which is designated for the relaxation of the monomer adsorption/desorption process. A_0 is chosen to be $A_0 = 0.886, 0.899$ and 0.94 for $T = 293, 323$ and 353 K respectively. The amplitude prefactor of Eq.(4.9) corresponding to the center most layer of the melt is set to

$A = 0.84$, while that of the fit for the adsorption ACF is set to 1.

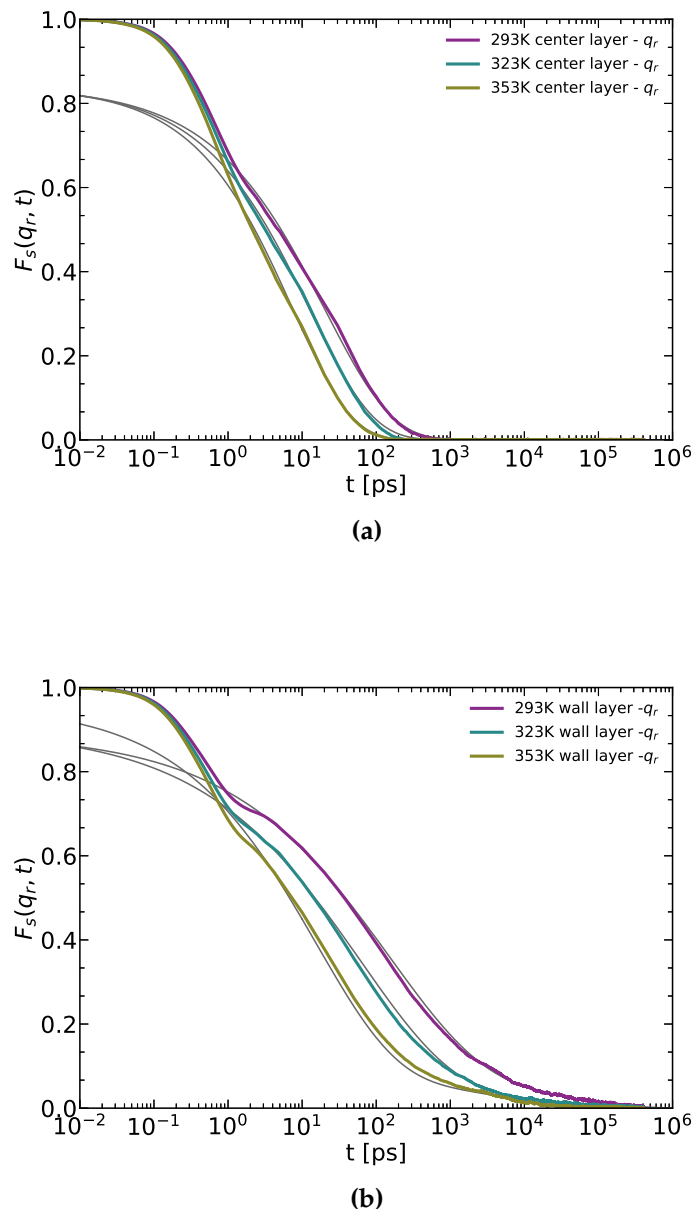


Figure 4.21: (a) shows the scattering function for \mathbf{q}_r for the center most layer along with the respective fits to the stretched exponential function in solid grey lines. The prefactor for eq.(4.9) is $A = 0.84$ for all three temperatures. (b) shows the scattering function for the wall layer with \mathbf{q}_r and the fits to the superposition of two stretched exponentials. The prefactor $A_0 = 0.886, 0.899$ and 0.96 for $T = 293, 323$ and 353 K respectively.

Figure (4.21) shows the plots of the fits and Table (4.2) includes the fitting parameters for the the adsorption autocorrelation as well as the scattering functions. Table (4.2) collects all the parameters obtained for the various fits to the

adsorption autocorrelation function (left) and the scattering function (right). For the parameters of the scattering function, the α -relaxation at the wall is slower than that of the center layers with slower relaxation for both as the temperature decreases.

Table 4.2: The table on the left hand side presents the fitting parameters τ , β obtained from the stretched exponential fit to $\Phi(t)$ while the table on the right hand side presents the fitting parameters $\tau_\alpha, \beta_\alpha$ and τ_{des}, β_{des} obtained from the stretched exponential fits to $F_s(q_r, t)$ in the bulk of the melt and in the layer adjacent to the walls.

Adsorption ACF			Bulk-like		Wall				
T [K]	τ [ps]	β	T [K]	τ_α [ps]	β_α	τ_α [ps]	β_α	τ_{des} [ps]	β_{des}
353	66 089	0.320	353	8	0.550	15	0.400	5 447	0.502
323	151 281	0.334	323	13	0.510	59	0.342	11 052	0.329
293	259 638	0.364	293	20	0.480	149	0.343	53 402	0.553

The difference between the wall and center α -relaxation increases as we decrease the temperature as well. The stretching exponent for the α -relaxation at the center layer is larger than the one calculated at the wall where the former is closer to the bulk value [145, 146].

Another observation also made in the parallel walls confinement [24] is that for all temperatures studied, the onset of the third step is seen when the scattering function has decayed to ~ 0.2 which in the adsorption autocorrelation function $\Phi(t)$ corresponds to a decay to ~ 0.8 . However, in the cylindrical geometry, τ_{des} should be considered with caution. The latter is supposed to quantify the relaxation of the adsorption process of the monomers at the wall. The way the scattering function is calculated, $F_s(q_r, t)$ is affected by the adsorption/desorption process; however, it does not portray only the desorption of the monomers from the cylindrical wall. Hence, the divergence between τ for $\Phi(t)$ and τ_{des} for the scattering function. For a parallel wall geometry, \mathbf{q}_z is the momentum transfer perpendicular to the confinement and for the monomers to desorb, they need to move along $\hat{\mathbf{e}}_z$ away from the wall. Any movement along the wall (i.e. $z_i(t) - z_i(0) = 0$) does not contribute to the adsorption process and consequently to the third step in the relaxation. The same cannot be applied to the cylindrical geometry. Considering the nanopore, movements along the pore in either $\hat{\mathbf{e}}_x$ or $\hat{\mathbf{e}}_y$ contribute to the relaxation of the scattering function while the

monomers are still adsorbed. This explains why the onset of the third step in the scattering function is triggered by the desorption process; however, $F_s(\mathbf{q}_r, t)$ relaxes before the relaxation of the adsorption autocorrelation function.

As a final step concerning the dynamics on the monomer and chain scale, we look at the number of monomers adsorbed in each chain with its COM in the first layer. We follow here the geometric criteria mentioned in subsection (4.2.2) and we check at each frame whether a chain's COM is in the first layer of size $\sim R_g$ and how many monomers in each chain are adsorbed to the pore wall (is in the first monomer layer of size ~ 0.4 nm from the wall). Figure (4.22) shows a histogram, for all three temperatures, of the adsorbed monomers per chain normalized by the total number of frames. This consequently displays the average number of chains (y-axis) per frame with a given number of adsorbed monomers (x-axis).

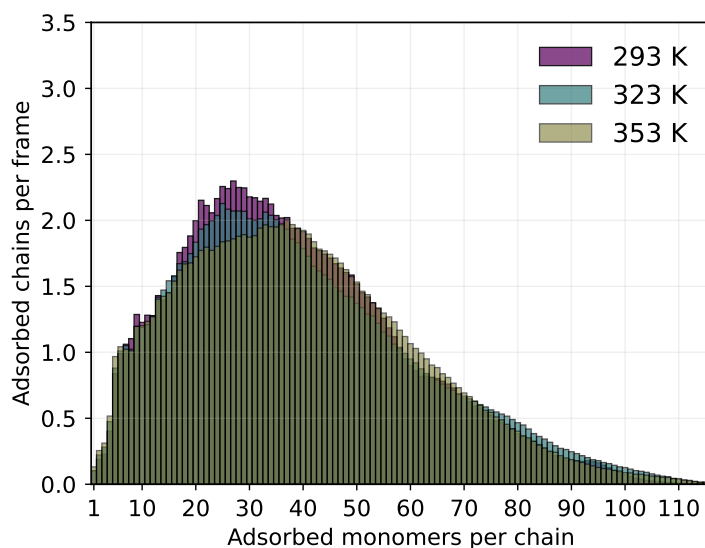


Figure 4.22: Histogram of the number of adsorbed monomers per chain in the first layer of size $\sim R_g$ for all three temperatures in the nanopore system. The total number of adsorbed monomers in each bin is normalized to the total number of frames which in turn gives us the average number of chains per frame (y-axis) with a given number of adsorbed monomers (x-axis).

It is good to note that the plot doesn't include the chains that are in the first COM layer with zero adsorbed monomers. However, on average in each frame there are approximately 6 chains with zero adsorbed monomers indicating that $\sim 5\%$ (average of total chains in the first layer is ~ 116 obtained from integrating

over the histogram) of the chains in the first layer are not adsorbed to the pore wall. The distribution is skewed and most chains in the first layer have 20 – 40 adsorbed monomers depending on the temperature with higher number of adsorbed chains for lower T . The total number of adsorbed chains (chains with adsorbed monomers) is consistent for all temperatures with $N_{Ads}^{chains} \simeq 112, 108$ and 109 for $T = 293, 323$ and 353 K respectively. If we look closely at the lower right side of the distribution, we can see that there exists chains with a large number of adsorbed monomers including the case where the latter includes all 116 united atoms in the chain.

As we have seen in the sections containing the MSD and INSF, these monomers at the wall take longer than the time scale of our simulations to desorb and move away from the wall. In this geometry specifically, when the chains start to desorb and try to move away from the pore wall especially in the motion perpendicular to the pore axis, they are hindered by the curvature of the wall and are subject to re-adsorption.

4.2.4 Segmental Orientational Correlation Function

Melt dynamics are also dependent on the conformations of the polymer molecules and the relaxation processes vary in length and times scales: from chain to local segmental mobility. Accordingly, different experimental methods are used to study different scales of motion.

Nuclear magnetic resonance (NMR) experiments, and specifically ^{13}C NMR spin lattice relaxation measurements, provide experimental data concerning the local segmental dynamics of polymer chains. The spin lattice relaxation time T_1 or the spin lattice relaxation rate $1/T_1$ are affected by the reorientation of the C–H bonds which in turn can be described by the orientational autocorrelation function of the bond vector between the carbon atom and its bonded proton (H). Therefore, in this subsection, we will focus on the relaxation of individual C–H bonds in the chains. We also make a distinction between C–H bonds based on whether they belong to *cis* or *trans* groups and introduce a unit vector $\hat{\mathbf{e}}_i$ along a given i -th C–H bond at time t . The averaged second Legendre polynomial of the orientational autocorrelation of $\hat{\mathbf{e}}_i(t)$ is,

$$\langle C(t) \rangle = \frac{1}{2} \left(3 \langle [\hat{\mathbf{e}}_i(t) \cdot \hat{\mathbf{e}}_i(0)]^2 \rangle - 1 \right). \quad (4.24)$$

From the above expression, we can compute experimentally obtainable quantities such as T_1 . The latter largely depends on the local dynamics in the chain. Moreover, previous simulations on polymer melts [147–150] have shown that the decay of the C–H bond autocorrelation function is also a result of mainly, but not exclusively, local conformational changes. Consequently, in those simulations they represent the obtained $C(t)$ function as a sum of a stretched exponential term that describes the local conformational contributions to the relaxation alongside a time exponential related to the long relaxation of the chain backbones. However, in simulations on confined PBD between graphite walls, it was found that $C(t)$ is best described there by a superposition of two stretched exponentials. From the fits of $C(t)$ (all fitting parameters can be found in Table (B.1)), the spectral density, defined as the Fourier transform of the autocorrelation function, can be calculated,

$$J(\omega) = \int_0^{\infty} C(t) \cos(\omega t) dt. \quad (4.25)$$

The spin-lattice relaxation times (T_1) that are obtained experimentally are related to the motion of the C–H bonds [151] by equation (4.26) where ω_H , ω_C are the Larmor frequencies of the hydrogen and carbon nuclei, respectively. K is a constant with a value of 2.29×10^9 and $2.42 \times 10^9 \text{ s}^{-2}$ for sp^3 and sp^2 nuclei respectively. For our calculations we have an sp^2 nucleus and the number of hydrogen atoms attached to the carbon atom is $n = 1$.

$$\frac{1}{nT_1} = K \left[J(\omega_H - \omega_C) + 3J(\omega_C) + 6J(\omega_H + \omega_C) \right] \quad (4.26)$$

The time integral of the correlation function yields also the correlation time,

$$\tau_c = \int_0^{\infty} C(t) dt. \quad (4.27)$$

The system is again divided into three different layers along the pore; therefore, the $\langle \rangle$ is considered to be the average over all equivalent bonds i in a certain layer (where a bond belongs to a specific layer if the radial position of its center of mass is in that bin at $t = 0$) and a time average over all the frames in the trajectory. Our model is made up of united atoms, thus, as mentioned in Chapter 3, each atom is either CH or CH_2 . To be able to study individual C–H bonds

we are required to calculate the position of the hydrogen atom from the stored united atom (carbon) positions. To best reproduce the molecular geometries we place the hydrogen atom along the bisector of the angle between the $\text{CH}_2\text{-CH}$ and $\text{CH}=\text{CH}$ bonds. Knowing the length of a C-H bond (1.09 \AA) and with the following definition of γ which is a vector going through the bisector of the angle of two vectors \mathbf{a} and \mathbf{b}

$$\gamma = \lambda \left[\frac{\mathbf{a}}{|\mathbf{a}|} + \frac{\mathbf{b}}{|\mathbf{b}|} \right], \quad (4.28)$$

we can obtain the unit vector $\hat{\mathbf{e}}_i$ as well as the position of the respective hydrogen atom. The latter is needed to calculate the center of mass of the C-H bond.

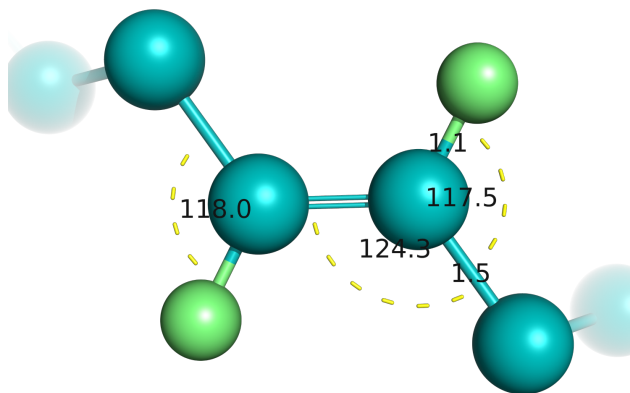


Figure 4.23: A snapshot showing a *trans*-PBD molecule with the calculated positions of the hydrogen atoms. The values show the bond lengths (in \AA) with the correct values for the C-H bond as well as the angles.

Figure (4.23) shows one *trans*-PBD molecule with the calculated hydrogen positions. Figure (4.24) shows the orientational autocorrelation function for both the *cis* and *trans* groups at $T = 293 \text{ K}$ for the three layers in the melt (Appendix B includes the plots for $T = 323$ and 353 K). The relaxation for all three temperatures and for both conformations is slowed down in the layer at the wall while the other two layers are overlapping. The relaxation is also slower as we decrease the temperature. The two-step decay that was observed previously in the MSD as well as the incoherent neutron scattering function can also be seen here setting in with a short plateau at $\sim 1 \text{ ps}$ for the *cis* group and at $\sim 0.5 \text{ ps}$ for the *trans* group. As we have seen in the scattering function, the plateau separating the time steps is more prominent at lower temperatures. Figure (4.25) shows the

same behavior.

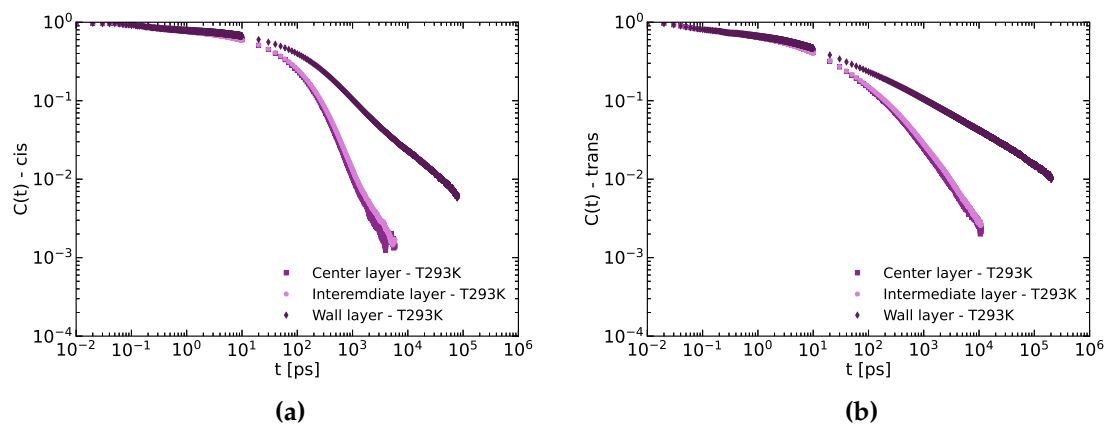


Figure 4.24: The orientational autocorrelation function of C–H *cis* (a) and *trans* (b) groups at $T = 293$ K for the three layers in the melt.

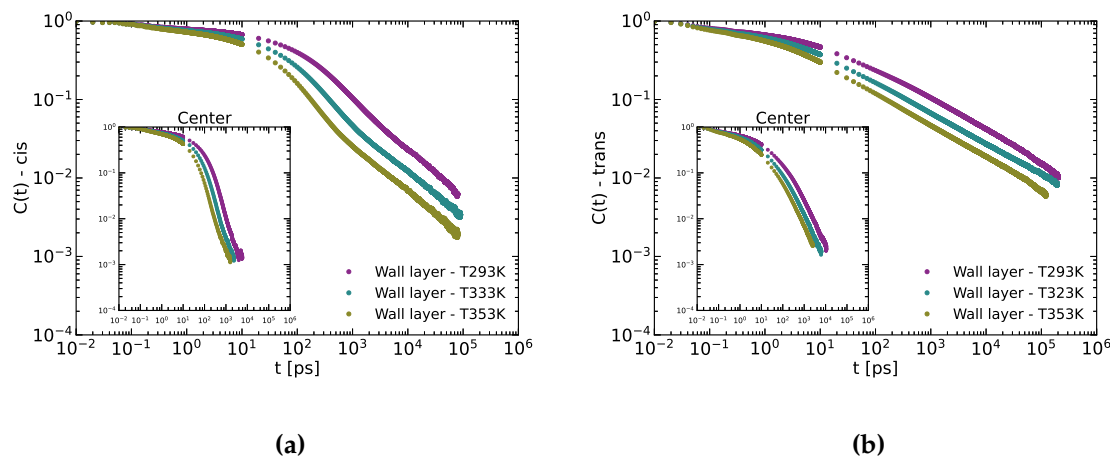


Figure 4.25: The orientational autocorrelation function of C–H *cis* (a) and *trans* (b) groups for all temperatures at the wall. The inset shows the corresponding data for the center-most bulk-like layer.

Table (4.3) shows the calculated correlation times τ_c of the C–H bond relaxation for all temperatures and for the center and wall layers. The table also shows the values obtained for the bulk PBD from Ref. [92]. For a better description we plot these values on a semi-log scale against the inverse temperature. We do not have enough temperature data to make any conclusions on the temperature dependence but some general observations can be made.

Table 4.3: The correlation times τ_c (left) and T_1 (right) calculated from the $C - H$ bond relaxation at three different temperatures for both the *cis* and *trans* groups. The values for the bulk are taken from Ref. [92].

τ_c [ps]							nT_1 [s]						
<i>trans</i>			<i>cis</i>				<i>trans</i>			<i>cis</i>			
T [K]	Nanopore		Bulk	Nanopore			T [K]	Nanopore			Nanopore		
	center	wall		center	wall	Bulk		Center	Wall	Bulk	Center	Wall	Bulk
293	171	20 919	305	111	3 725	184	293	0.79	0.55	0.61	0.54	0.33	0.37
323	87	12 758	78	59	2 148	61	323	1.22	0.84	1.03	1.01	0.49	0.85
353	46	9 137	37	32	992	26	353	1.85	1.08	1.95	1.62	0.77	1.7

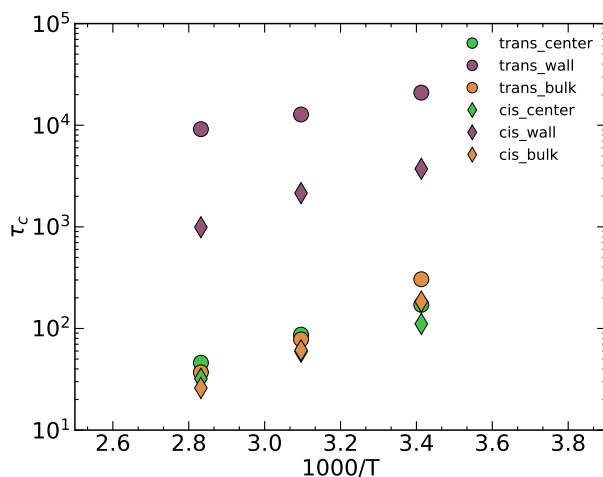


Figure 4.26: $C(t)$ autocorrelation times calculated from the integral in expression (4.27).

For the layer in the center and at higher temperatures the autocorrelation times start to overlap since at higher temperatures the faster dynamics lead to narrowing behavior where the spin-lattice relaxation times could then be directly calculated from the correlation times. However, that behavior is not yet reached here. Also for the layer in the center, we see a slightly weaker temperature dependence of τ_c for lower temperatures than the one observed in the bulk. The correlation times for the wall layer are noticeably higher than the center layer and the bulk with a greater increase for the *trans* group.

The resulting spin lattice relaxation times T_1 that correspond to the correlation functions in Figure (4.25) are shown in Table (4.3). The latter also shows the bulk values calculated from MD simulations for bulk PBD [91,92]. In the bulk simulations, they differentiate between *trans-cis* (a *trans* conformer followed by a *cis*), *trans-trans*, *cis-cis* and *cis-trans*. Since we study a certain group regardless of the one following we take the average values obtained in the bulk. The calculations were done with Larmor frequencies $\omega_H = 1885$ MHz and $\omega_C = 141.1$ MHz.

We quantify the relaxation of the *cis* and *trans* groups and relate to potential experimental results; however, our presented results should be taken with caution given the errors that accompany the fitting process.

The resulting T_1 values in the center are close to the bulk values especially at $T = 353$ K while the results on the other two temperatures vary. The latter is due to the discrepancy between the densities in the center at all three temperatures ($\rho_{center} \simeq 884 \text{ kg/m}^3$) and their respective bulk values. However, the relaxation times increase significantly for the layer at the wall for both the *cis* and *trans* groups. This is also in agreement with results found on PBD confined between graphite walls [24]. Figure 4.27 shows a comparison between two different types of confinement for the correlation function for both the *cis* and *trans* groups at $T = 353$ K. $C(t)$ for the *cis* group is slower for the nanopore system for the layer at the wall while the center layers are comparable.

As for the *trans* $C(t)$, both layers are comparable yet with a slightly slower mobility for the pore system.

While both types of confinements affect the segmental mobility in the layer at the wall, the mobility of both groups is further disturbed by the nanopore system. These results help us get a clearer picture on what affects segmental relaxation and consequently T_1 values. Apart from any temperature dependence which can be seen in the bulk, segmental relaxation in confinement is also influenced by the

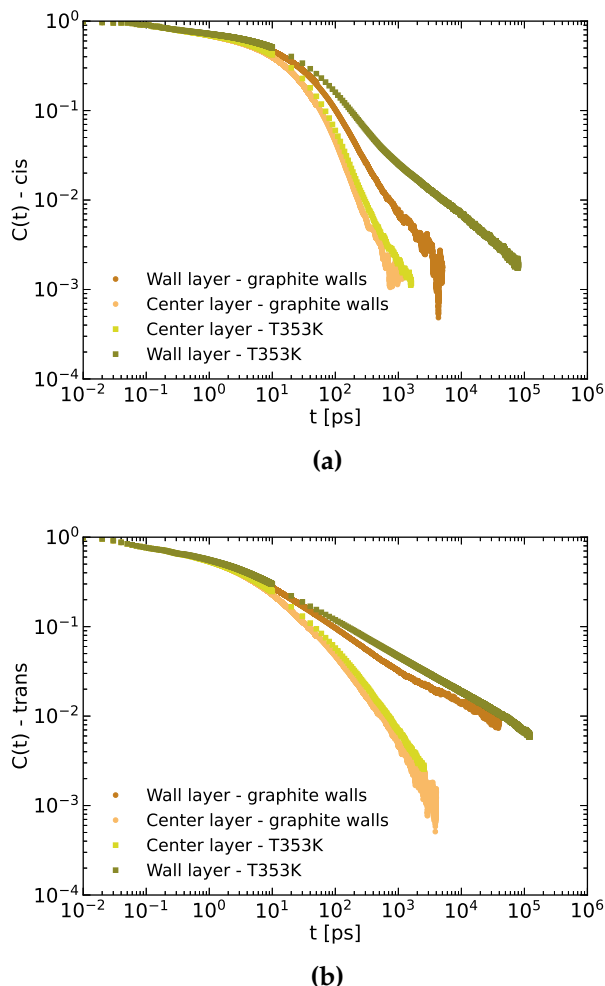


Figure 4.27: The correlation function (**a** *cis* and **b** *trans*) at $T = 353$ K for the wall layer and center-most layer for the nanopore (green) and for the confinement between parallel graphite walls (orange) taken from Ref. [24].

melt-surface interactions and their effect on the adsorption process. The latter along with the ordering on the segmental scale at the wall impede the segmental mobility resulting in the decrease in T_1 . It is also good to note the difference in the time scales between the correlation times obtained from the OACF [ps], motion of monomer and chains and the spin-lattice relaxation times [s]. Given that, we would note that even though the calculated spin-lattice relaxation times are for different layers in the melt, they incorporate an average over the polymer melt.

In this section, we focused on the effect of the nanopore on the dynamics in the melt. All the analysis indicates the existence of a layer at the wall with a size $\sim R_g$ that exhibits slower dynamics due to the nanopore confinement. The mean squared displacement showed a slowing down on both the monomer and chain scale at the wall that increases slightly at lower temperatures. Following our first assumption about an adsorbed layer at the wall we studied in conjunction the adsorption autocorrelation function and the incoherent scattering function in the melt. For the latter we could study the scattering function for the motion parallel and perpendicular to the walls which is also an experimentally attainable quantity. For the layer at the wall, at all temperatures the relaxation process exhibits an extra step in the time scale separation which is correlated to the adsorption/desorption process of the monomers. From snapshots of chains directly at the wall we observe that at the lowest temperature of $T = 293$ K the desorption process is beyond the time scale of our simulations. The scattering function calculated for the whole melt with a momentum transfer perpendicular to the pore walls also shows the third step in the decay of the relaxation revealing the extent of the effect of the confinement on the melt as a whole. On the segmental scale, we study the relaxation of *cis* and *trans* groups. The latter displays similar behavior to the one seen in parallel wall confinement for the center and wall layers with a distinguishable slowing down at the wall. The *cis* groups' relaxation is affected less by the wall but the effect is more prominent in the cylindrical geometry than in the parallel wall confinement. To allow further comparison with experiments (not yet done at this point), the spin lattice relaxation times were calculated from the conformational autocorrelation function. The latter analysis allows us to further understand the effect of the confinement on segmental relaxation.

Chapter 5

Polybutadiene surrounding an alumina nanorod

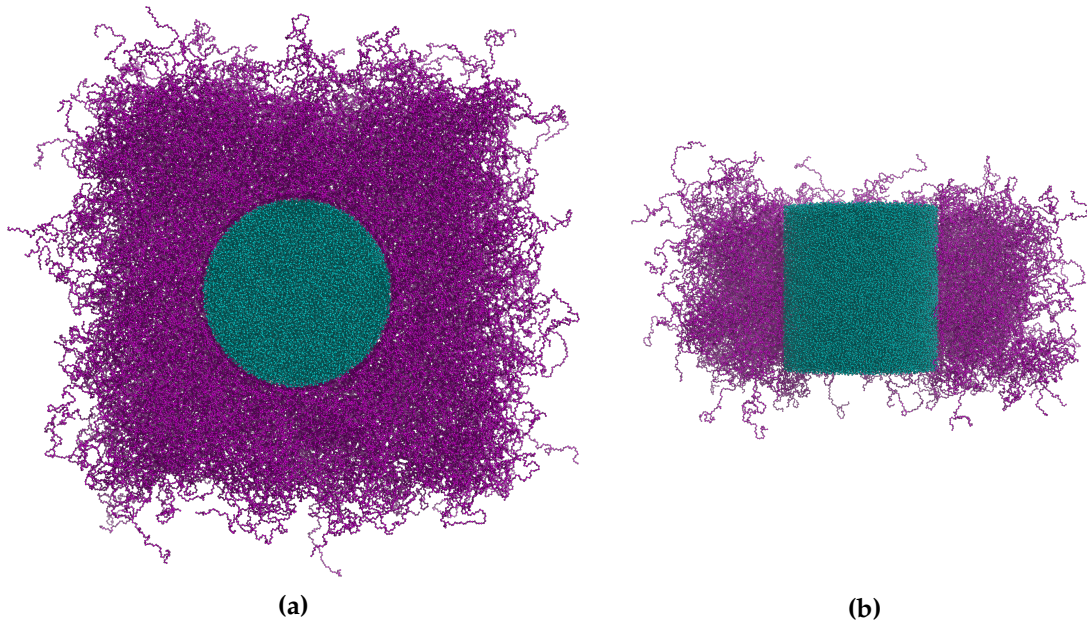


Figure 5.1: Snapshots of the system of a polybutadiene melt surrounding an alumina nanorod from two different views: **(a)** along the axial direction and **(b)** along the radial direction (some PBD chains were removed to view the alumina rod).

At the beginning of Chapter 4, it was mentioned that we study two different systems in this dissertation. The first system represents a polybutadiene (PBD) melt confined inside a cylindrical alumina nanopore with its structure and dynamics discussed in Chapter 4. This chapter will tackle the second system where an alumina rod is placed inside a polybutadiene melt. The PBD model is the one

also used for the PBD inside the alumina nanopore and is described in Chapter 3 and in more detail in Refs [91,97].

The presence of spherical nanoparticles in polymer melts introduces a region of altered polymer properties which is commonly referred to as the interphase. The interfacial contacts create perturbations in both the structure (for e.g. Refs. [120, 131, 152, 153]) and the dynamics (for e.g. Refs. [32, 66, 69, 72]) of the melt. Therefore, understanding the interfacial region is critical in controlling ultimately the properties of nanocomposite materials.

This chapter will address the structural and dynamical properties of a PBD melt surrounding a single alumina nanorod (with a radius larger than the melt's gyration radius) in comparison to the bulk and the previous system where the melt is confined inside the nanopore and encounters a different surface curvature. The alumina nanorod is fixed and spans the simulation cell in the axial direction (z -axis). The preparation of the system and the simulation parameters can be found in Chapter 3 in their respective sections.

5.1 Structure of the melt

Over the past couple of decades, several theoretical studies [154–157], coarse-grained [25,27,30,33,65–67,69,158–164] and atomistic simulations [153] have been conducted to predict and investigate the structure and conformation of polymer nanocomposites. For spherical nanoparticles (NP), some theoretical studies [155, 156] predict that around the NP, the monomers are depleted and the density of the polymer is reduced compared to its bulk value. Other theoretical studies [154] observed that for attractive spherical NP smaller than the polymer chains, the polymer chain dimensions are perturbed and there is an increase in the radius of gyration. Some coarse-grained simulations [30,165] on spherical NP in polymer melts also show that the monomer density is lower at the polymer-NP surface compared to the bulk unless the polymer chains are attracted to the spherical NP [66,153,164,166–169]. For the latter, the monomer density increases in the vicinity of the NP and is higher than its bulk value. As for the expansion of the chains, different simulations have given contrasting results. Here we study the density profile of the monomers and chains in the system as well as the shape of the chains across the melt. We then proceed to investigate any type of orientational ordering on both the segment and chain scales.

In this section we report on the effects of an alumina nanorod of diameter 10

nm on the structure of the melt for our simulations for three different temperatures ($T = 293, 323$ and 353 K).

5.1.1 Density layering

For our system with a total number of PBD chains $N_c = 1361$, we expect that the density away from the wall is close to the bulk value. The monomer and center of mass (COM) densities are calculated along the radial direction for bins of equal volume. The initial bin size that starts close to the melt-rod interface is 0.2 \AA and 0.5 \AA for monomer and COM densities respectively. Since the bin size becomes smaller as we move further away from the rod in the radial direction, a maximum radius for the calculations was set at 9 nm . The spatial locations of the monomers and centers of mass along the radial direction were calculated for each bin and then averaged over the entire trajectory.

Figure (5.2a)¹ shows the monomer density for all three temperatures normalized to its value away from the nanorod. The density profile has a well defined layered structure with a distinct enhancement in the first layer which is a consequence of the melt-rod attraction. The oscillations in the monomer density persist over a distance of around 2.5 nm similar to the PBD inside the nanopore case. In fact, the amplitudes of the density curves are also almost identical to that seen in Figure (4.2a) indicating that for a nanostructure with the same contact surface area, whether the melt is confined inside the nanopore or surrounding the alumina nanorod, the density profile is a result of the interaction. The profile has a length scale close to the size of the monomer $\sim 0.4 \text{ nm}$ and as the temperature decreases the first peak becomes slightly more defined. Away from the rod walls the melt reaches a density comparable to that of the bulk (865 kg/m^3) within a 0.58% percentage difference.

Figure (5.2b) displays a 2D monomer density map of the melt at $T = 323 \text{ K}$ and is in agreement with Figure (5.2a). The density map has a grid size of 0.02 nm and averaged along the axial direction. Moreover, the density is normalized to its value far away from the nanorod with darker shades of green representing layers with high density. Different layers can be observed with an increase in intensity as we move closer to the rod walls. After $\sim 3 - 4$ layers in the opposite direction, a homogeneous density is reached. Below a radius of $\sim 5 \text{ nm}$, where

¹In this figure and all the figures in the current section, r is the radial position with a value of 5 at the wall and then increases as we move away from the nanorod

the alumina atoms are, the density of the PBD is zero. Figure (5.2a) includes the center of mass density profile at $T = 353$ K. The plot for all three temperatures can be found in Appendix (C). For this geometry, the center of mass of a chain can be located inside the cylindrical rod given that the chains can wrap around it which will also be significant once the gyration tensor is studied. The center of mass density is also normalized by its value away from the rod walls. The density layering indicates that we might also observe for this system an adsorption of the monomers to the surface. As for the orientational ordering close to the cylindrical rod we will proceed in the next two subsections to study the ordering on the double bond scale as well as the chain scale.

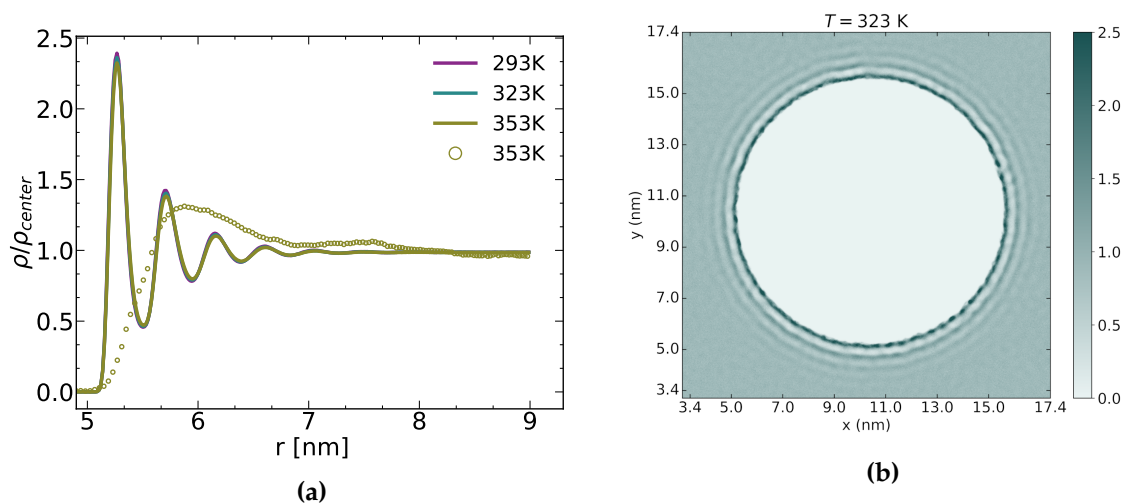


Figure 5.2: (a) Monomer density profile for all three temperatures normalized to their value away from the rod walls. The center of mass density (green circles) is shown for $T = 353$ K. The bin volume along the radial direction is kept constant with an initial size of 0.2 \AA and 0.5 \AA close to the rod wall for the monomer and COM densities respectively. (b) A 2D monomer density map along the x and y directions showing the different layers. The grid size is taken to be 0.02 nm and averaged along the axial direction. The density is normalized to the value away from the wall and is calculated for $T = 323$ K.

5.1.2 Double bond orientational ordering

To calculate the orientational ordering of the double bonds in the melt we use the second Legendre polynomial of the angle (θ) between the double bonds and the radial/axial directions defined in eq.(4.1). The melt was divided into cylindrical slabs across \hat{e}_r starting at the nanorod wall at 5 nm and a double bond belongs to a certain slab if its center of mass is in that layer at a time t . The spatial locations

of the double bonds were calculated for each slab along with the double bond's $P_2(\theta_r)$ and $P_2(\theta_z)$ and their respective angles.

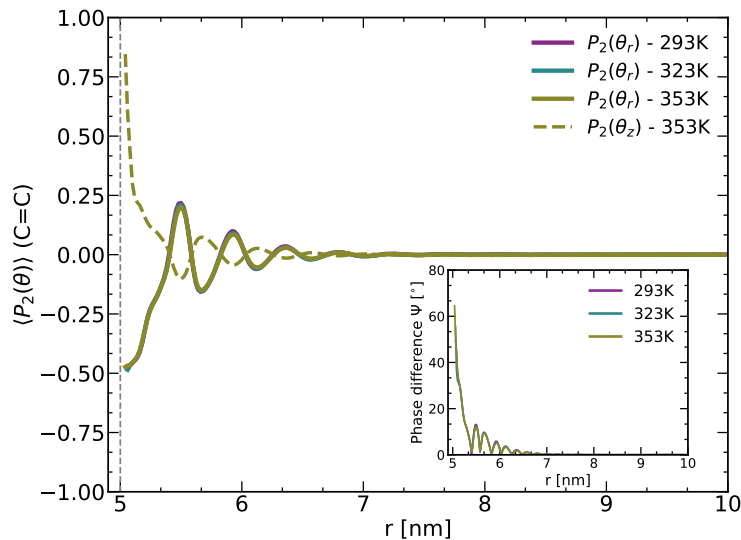


Figure 5.3: The second Legendre polynomial $P_2(\theta_r)$ for the angle with \hat{e}_r at $T = 293$, 323 and 353 K and $P_2(\theta_z)$ for the angle with \mathbf{z} at $T = 353$ K. The inset shows the phase difference between the two angles across melt. The grey dashed line indicates the radial position of the nanorod wall.

Figure (5.3) shows P_2 for the angle between the double bonds and the radial direction for all three temperatures and for the angle with the axial direction for $T = 353$ K. The inset shows the phase difference between both angles defined in the previous chapter in eq.(4.2). For an angle of $\theta = 90^\circ$ the double bonds would be perpendicular to the studied direction and $P_2 = -0.5$. There exists a similar behavior to the nanopore system given that at the interface, $P_2 \simeq -0.5$ indicating that the double bonds prefer to lie perpendicular to the normal to the nanorod surface. However, for the nanorod case the double bonds seem to be more compelled to align with the axial direction \hat{e}_z especially at higher temperatures. The plots showing $P_2(\theta_z)$ can be found in the supplementary material in Figure (C.2) and one can observe that for the highest temperature $T = 353$ K the value approaches 1 indicating a strong alignment with the axial direction. This effect decreases as we lower the temperature.

The layering here extends to ~ 2.5 nm away from the surface of the nanorod with a decrease in the amplitude as we move further away and closer to bulk-like melt behavior. Consequently, we can state that for both types of curva-

ture/confinement, the similar density layering, which in itself is a result of the interaction, causes the double bonds to lie perpendicular to the normal to the surface of confinement. A slight difference is observed when comparing the angle with the axial direction where the curvature of the nanorod confinement forces the double bonds to be slightly more aligned with \hat{e}_z .

5.1.3 Chain ordering and orientation

Gyration Tensor

The shape and orientation of the chains can be accessed by studying their gyration tensor defined in eq.(4.3). We know that for the case of a PBD melt inside a nanopore, the chains' gyration radius is close to its bulk value except at the interface for the lowest temperature $T = 293$ K. Moreover, for all temperatures, the confinement causes the gyration ellipsoid of the chains to be aligned with the axial direction of the cylindrical pore where the strength of the alignment increases with decreasing temperature.

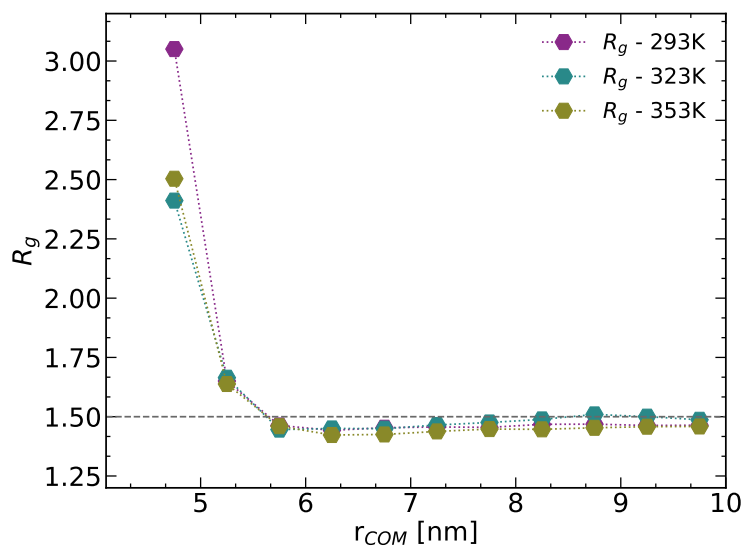


Figure 5.4: The radius of gyration R_g of the chains in the system across bins of size 0.5 nm in the radial direction for all three temperatures. The dashed grey line is the bulk value of R_g .

We perform the same calculations found in section (4.1.3) where we obtain the gyration tensor for each chain at each time t of the simulation trajectory. The chains are then binned into layers of thickness 0.5 nm and a chain belongs to a

specific layer if its center of mass is in that layer at time t . For this geometry, if a chain is wrapped around the nanorod then its center of mass position can be at a radial position smaller than 5 nm (radius of the nanorod). Therefore, we start our analysis at a radius below the surface of the rod.

The radius of gyration, obtained from the trace of the gyration tensor, is shown in Figure (5.4) for all three temperatures as a function of the distance from the center of the nanorod. The effect of the nanorod on the radius of gyration R_g extends to ~ 1 nm away from its wall after which R_g retains its bulk value. Unlike the "concave" curvature, for the layer directly at the wall the radius is greatly affected at all temperatures. According to our calculations, only a few chain centers of mass are in that layer throughout the whole trajectory; nonetheless, for the chains that are, the radius of gyration reaches a value of $\sim 2R_g$ for the lowest temperature $T = 293$ K.

To further understand the shape of the chains we study the eigenvalues of the gyration tensor and the chains' anisotropy in Figure (5.5). The eigenvalues represent the principal axes of the gyration ellipsoid with λ_1 being the largest axis ($\lambda_1 > \lambda_2 > \lambda_3$). The anisotropy addresses the symmetry of the chains and has a bulk value of ~ 0.4 that coincides with the value for the chains ~ 1 nm away from the rod wall as seen in Figure (5.5). However, for the chains at the wall the anisotropy approaches 1 which indicates stretched chains at all temperatures with the highest value for $T = 293$ K. These results agree with the eigenvalues from which the shape of the chains can be determined. λ_1 , which is the largest eigenvalues, decreases as we move away from the nanorod wall; however, it remains larger than the other two eigenvalues λ_2 and λ_3 . The ratios of the principal components away from the wall are found in the plots in Figure (5.5) and are in agreement with the literature [124,125].

As we change the curvature of confinement the shape and size of the chains at the interface drastically change as well. For the nanorod "convex" curvature the pancake like structure observed at lower temperatures in the nanopore system extends to higher temperatures for chains whose center of mass is at the first layer. This results in a large radius of gyration and a high value of the anisotropy $\langle \kappa^2 \rangle$. The difference in curvature allows the chains in this system to stretch further which could lead to larger values of R_g and λ_1 than the ones observed for the nanopore confinement. The rod-like value of the latter and the position of their COM suggest that the chains are stretched and the possibility of adsorption respectively.

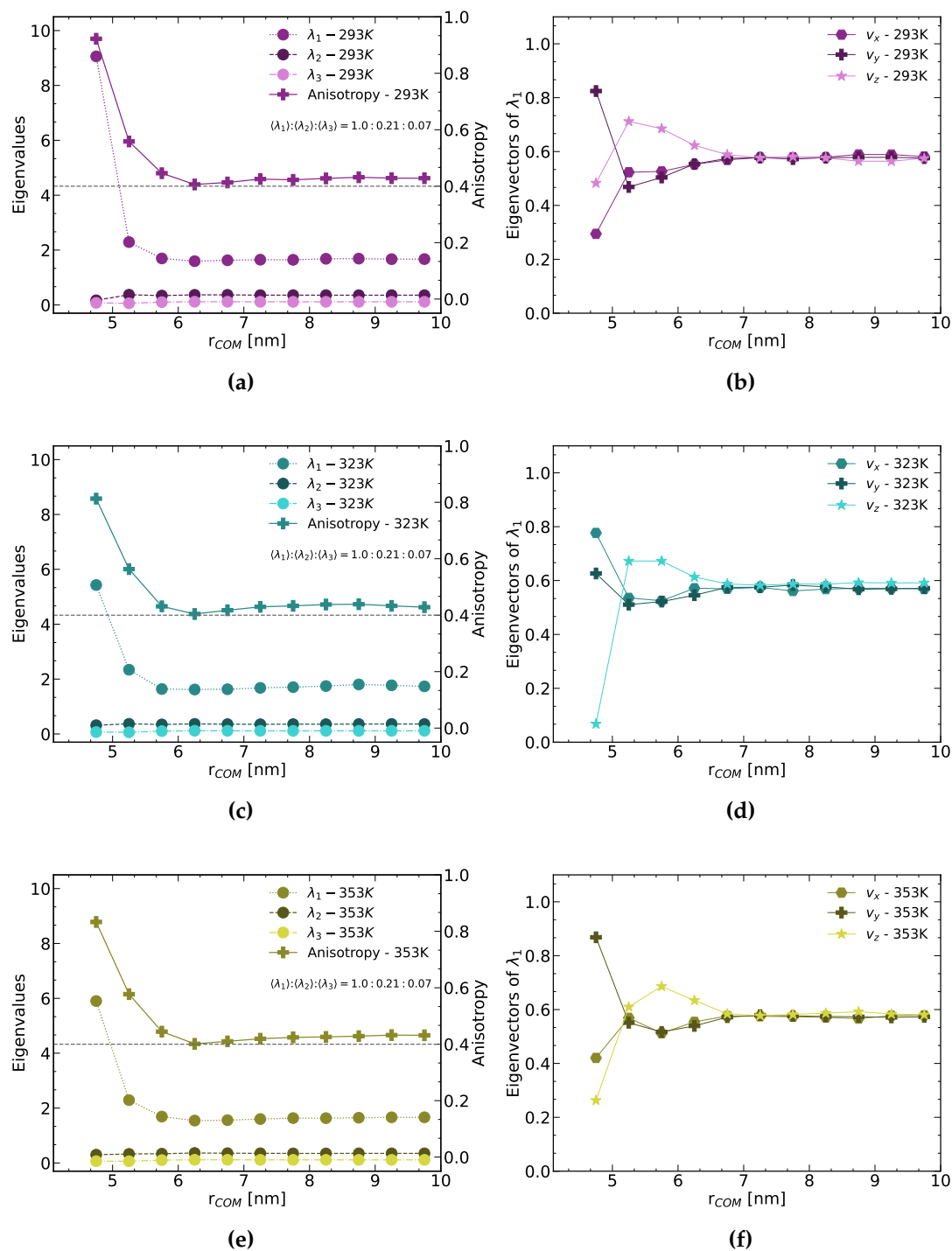


Figure 5.5: (a, c, e) show the eigenvalues of the gyration tensor representing the principal axes of the gyration ellipsoid for all three temperatures. The relative shape anisotropy and its bulk value (grey dashed lines) are also shown. The ratios of the eigenvalues are found in their respective plots. (b, d, f) show the eigenvectors, indicating the orientation, of the largest eigenvalue λ_1 of the gyration tensor in cartesian coordinates. r , in both, is determined by the distance of the chain's center of mass from the rod wall.

Figure (5.6a) is a snapshot of the positions of all the monomers over time for two chains in the melt. The configurations are taken over a time span of 50 ns of the simulation starting at $t = 100$ ns for $T = 323$ K. The monomers in magenta belong to chain 1329 whose center of mass is away from the nanorod wall at the starting time of the snapshot. Our interest lies in the chain at the wall (1198) shown in teal and whose center of mass is at the interface layer. The chain appears to be adsorbed to the wall and lies along the curvature of the nanorod with mostly its ends moving freely. Figures (5.6(b-e)) show the conformations of chain 1198 at the interface at four different times in the 50 ns time span. The configurations in Figure (5.6d) and Figure (5.6e) are accessible to chains in the pore system where the chain is either wrapping around the curvature or has some of its monomers adsorbed and the tails moving away from the walls. However, in Figure (5.6a) and Figure (5.6c) the chains obtain configurations only attainable in this system where they are allowed to stretch beyond the arc length of the curvature resulting in the stretched chains that we observe at the rod wall in this system.

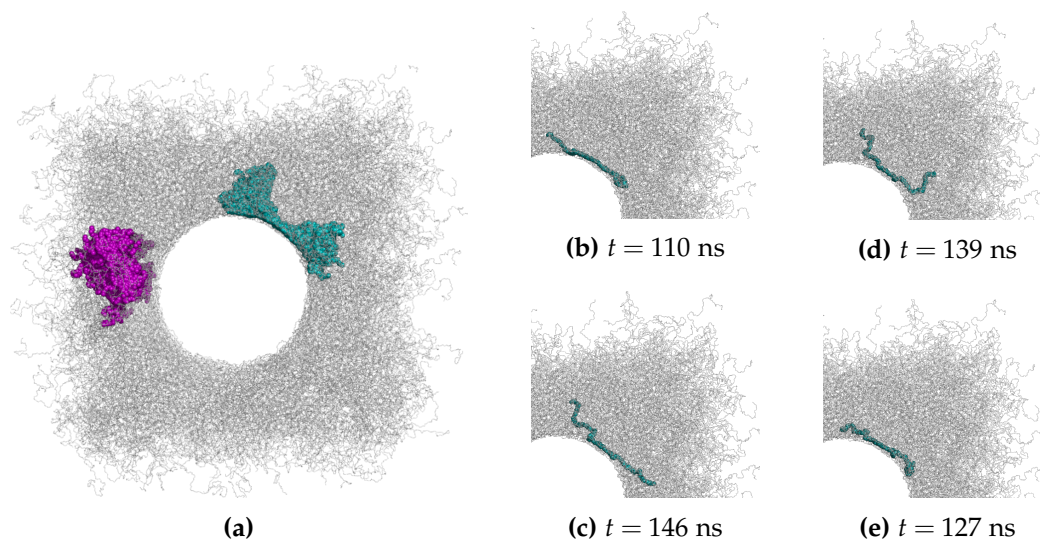


Figure 5.6: (a) A snapshot containing the positions of all the monomers over time for two chains in the melt. Chain 1198 at the interface in teal and chain 1329 that start with its center of mass away from the nanorod wall in magenta. The configurations are taken over a time span of 50 ns starting at $t = 100$ ns for $T = 323$ K. (b,c,d,e) Snapshots of chain 1198 at the interface at different times $t = 110, 146, 139$ and 127 ns respectively. The alumina atoms are not included.

Now that we have a clearer picture on the configuration of the chains, we proceed to study the eigenvectors of the largest principal axis λ_1 of the ellipsoid to

obtain information on their orientation. Similarly to the previous system, the absolute value of the eigenvectors was considered since the ellipsoid has head/tail symmetry. The normalized values of the eigenvectors are shown in Figure (5.5). The latter figures show that the effect of the nanorod extends to around $\simeq 1.5$ nm defining a length scale comparable to the radius of gyration R_g for the orientational ordering and slightly greater than the one observed in the previous system with the melt confined inside the nanopore. For the few chains that are found directly at the wall layer, the alignment is similar for $T = 293$ K and $T = 353$ K and is oriented along the \hat{e}_y . For $T = 323$ K, the alignment is along both \hat{e}_x and \hat{e}_y and almost no contribution from the axial direction. Thus, the chains for that temperature prefer to align perpendicular to \hat{e}_z . This is different to what was observed in the nanopore system where the chains were oriented along the axial direction with a stronger alignment for lower temperatures.

Beyond the first two layers (~ 1 nm away from the wall) the chains' preferred alignment changes to the axial direction before they retain bulk-like behaviour in agreement with the chains studied at the center of the pore. Previous studies on polymer melts with nanoparticles [66,170] have demonstrated similar behavior where the chains are "flattened" against the nanoparticle surface for approximately the width of the first layer. The results from both systems demonstrate that the chain ordering, conformation and orientation is not only affected by the interaction between the melt and the confinement but by the curvature of the latter as well.

5.1.4 Nematic Order

The large value of the anisotropy of the chains along with the magnitude and direction of the principal axes of the gyration ellipsoid demonstrate that the chains with their center of mass at the wall are stretched and have a preferred orientation. In addition, the value of the anisotropy implies the possibilities of nematic ordering of the double bonds at the wall region. We use eq.(4.6) to compute the nematic order tensor $Q_{\alpha\beta}$ of the double bonds for different bins across the melt. A double bond belongs to a specific bin if its center of mass is in that bin at a time t . For these calculations one tensor $Q_{\alpha\beta}$ was computed along with its eigenvalues for each bin at a time t and then averaged over the trajectory.

For a bin size of 0.4 nm we could not observe any ordering concurring with the results for the same bin size in the nanopore system. When calculating for a

bin of that thickness we would then be taking into consideration double bonds with at least one of their CH beads in the first bin layer, and since no ordering is present for that bin size we exclude the possibility of nematic ordering.

In this section we discussed the effects of the nanorod on the structure of the PBD melt. The density layering at the rod, which is identical to the one seen in the nanopore system, implies that it is a consequence of the polymer-rod and polymer-pore interactions rather than the curvature of the confinement. Nodoro et al. [153] also study the monomer densities as a function of particle size and find that the amplitudes increase with the diameter size. Since we conduct our simulations for only one diameter, we are unable to make a statement on the effect of the size on the structure. The layering in the monomer and chain center of mass density extend to ~ 2.5 nm away from the rod after which bulk density is maintained. This behavior is seen in several studies of polymer melts with nanoparticles [66, 132, 152, 153, 171, 172]. The peaks in the density profile suggest orientational ordering at the wall as well as a layer of adsorbed monomers. On the segmental scale, the second Legendre polynomial of the angle between the double bonds and the axial/radial direction indicates their preference to lie perpendicular to the normal to the surface and more along the axial direction as we increase the temperature. Coarse-grained simulations of Silica-Polystyrene nanocomposites [152] show a similar behavior for the angle between different bonds and the surface normal to the particle with a bond orientation angle of 90° . Theoretical studies [154], simulations [72, 173] and experiments [33, 73] have predicted chain swelling at the interface in polymer-nanoparticle composites. Specifically, for attractive nanostructure the polymer chains are stretched and flattened for the case of diameter $< 2R_g$. For the system with a nanorod of diameter 10 nm $> 2R_g$, we also obtain values for the anisotropy and λ_1 (the largest eigenvalue of the gyration tensor) indicating that the few chains with a center of mass inside the rod are stretched at all simulated temperatures. Moreover, our results show that most of those chains are wrapped around the nanorod. Beyond this first layer, the anisotropy value decreases and the alignment shifts to the axial direction until bulk-like behavior is attained.

5.2 Dynamics of the melt

The properties of polymer chains close to the surface of confinement are different compared to those in the bulk as we have seen so far, which in turn affects the behavior of the whole system.

In the following section, we investigate the dynamics of the PBD melt in the presence of the nanorod. We study the effect on the mobility at different scales, starting with the chain center of mass mean squared displacement, then the motion of the monomers through the incoherent neutron scattering function while we analyze the effects of the adsorption on the latter. Finally, we address segmental relaxation through the orientational autocorrelation function and obtain experimentally relevant values for the spin lattice relaxation times.

5.2.1 Mean Squared Displacement

The analysis based on the mean squared displacement is one that is only attainable through simulations yet it still is greatly efficient in providing a qualitative picture as well as some quantitative values for the relaxation times of the system. Similar to the previous nanopore system, we divide the melt into three different layers each of the size of $\sim R_g$ of the PBD chains. It is good to note again that when calculating the mean squared displacements we define the latter as the displacement in the axial/radial position of the monomers/centers of mass defined in Eq. (4.7).

For this system, we only calculate the MSD of the chain COM. Given the total number of united atoms in the system ($N_{total} = 157876$), the time and computational effort to calculate the monomer MSD for $\sim 10^5$ ps is quite large. Therefore, this subsection includes only the analysis on the chain scale leaving the monomer scale to the subsection involving the INSF.

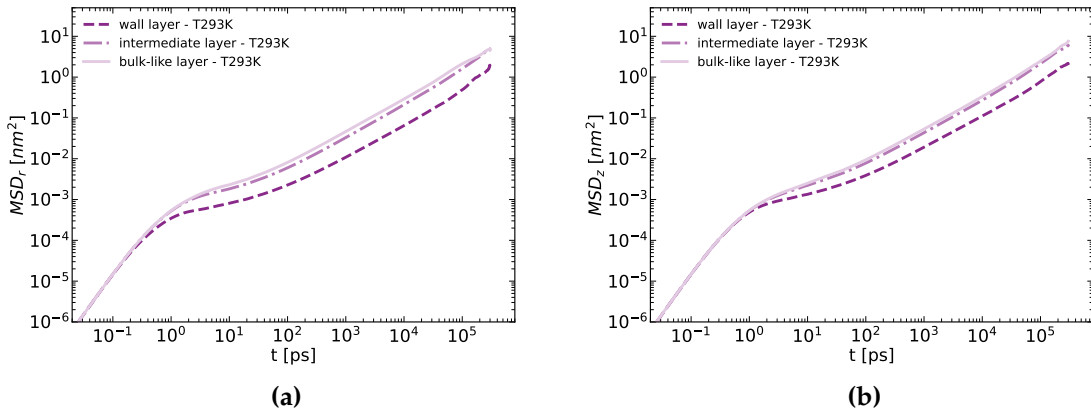
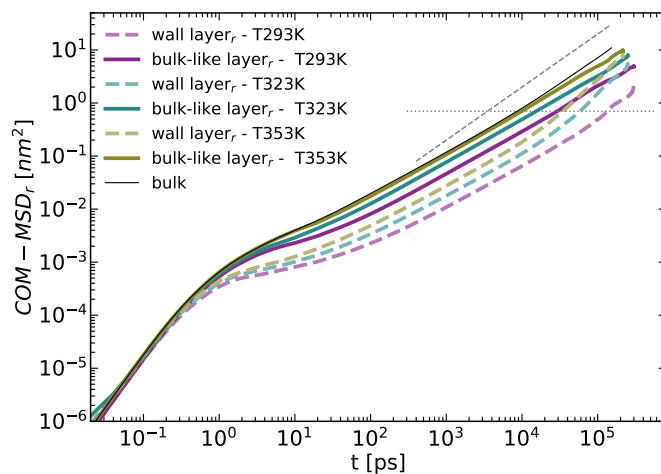


Figure 5.7: Center of mass (COM) mean squared displacement in the radial (a) and axial (b) directions for the three different layers at $T = 293$ K.

Figure (5.7) shows the COM mean squared displacement as a function of time in both the radial and axial directions at $T = 293$ K for three different bins along \hat{e}_r . In both directions there is a slowing down of the centers of mass motion in the first layer at the wall; however, the motion along the radial direction is slower at the rod wall when compared to the motion of the other layers as well as that along \hat{e}_z . The time scale separation from the ballistic regime becomes more prominent in the layer at the wall and this effect decreases as we increase the temperature.

Figure (5.8) shows the MSD of the centers of mass for all three temperatures for the layer at the rod wall and for the farthest layer along the radial and axial directions. After a ballistic regime, that is not affected by the proximity of the chains to the rod wall, the center of mass dynamics are slowed down at the interface. The motion along the axial direction is also affected at all simulated temperatures. At longer times, the center of mass motion at the wall layer, and especially at higher temperatures, catches up with the bulk-like layer farther away (a similar effect was observed in Ref. [43]). The statistics at these larger times are not as reliable; however, we can see a systematic increase in the displacement after a certain time in the interface layer for both directions and especially as we increase the temperature. This is also seen slightly for the intermediate layer at higher temperatures (Figures (C.3) and (C.4)). Therefore, we expect to see the same behavior for all the layers in the melt for long enough simulations in which the chains in the wall layer seem to escape it and return to bulk-like behavior.



(a)

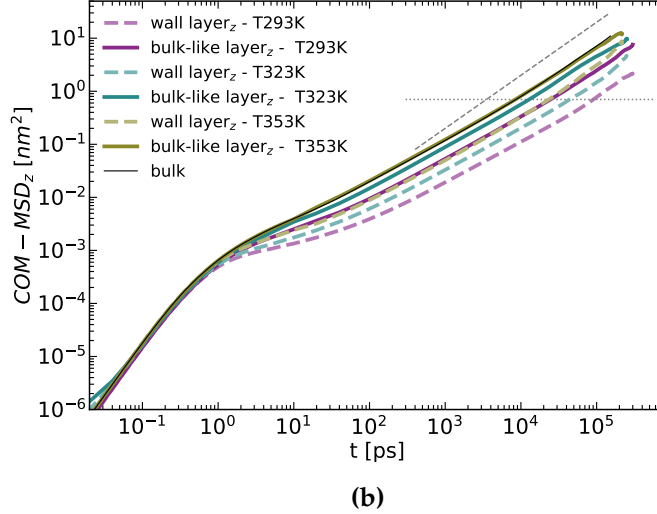


Figure 5.8: The center of mass (COM) mean squared displacement in the melt. **(a)** shows the MSD along the radial direction for wall and center layers at three different temperatures. The dashed line is the value $R_g^2/3$ that we define later as the relaxation time τ_R . **(b)** displays the COM MSD along the axial direction for the wall and center layers at $T = 293, 323$ and 353 K. The dashed grey line has a slope of 1 corresponding to diffusive behavior and the black solid line represents the bulk MSD [45].

The dashed grey line in both the radial and axial plots shows the diffusive behavior with $MSD(t) \sim t^1$. We can see that for our simulations the diffusive behavior is only reached for the motion along the axial direction especially for the layer away from the rod wall. However, since we expect the wall layer to become comparable to the bulk-like layer, then diffusive behavior is presumed to be reached there as well. The black solid line in Figure (5.8) represents the bulk center of mass MSD at $T = 353$ K. The layer we define as bulk-like, which is the farthest away from the rod wall, indeed behaves like the bulk. For the motion in the axial direction we see a complete overlap between that layer at $T = 353$ K and the bulk while for the radial direction our bulk-like layer is slightly slower still.

In the MSD displacement section of the nanopore we defined a quantitative characteristic relaxation time, τ_R where $\langle MSD_{COM}(\tau_R) \rangle = R_g^2/3 \simeq 0.7 \text{ nm}^2$. This value is also present in Figure (5.8) as the grey dotted line. Table (5.1) shows the values for τ_R for three different layers and temperatures for both the radial and axial directions.

Compared to the nanopore system, $\tau_R(\text{rod})$ shows faster dynamics and shorter relaxation times for all temperatures and layers. Roughly, the characteristic time $\tau_R(\text{rod})$ at $T = 293$ K is comparable to $\tau_R(\text{pore})$ at $T = 323$ K. Whereas the COM

motion in the pore is much slower than that in the parallel walls confinement, the latter is slightly more comparable with the nanorod system with $\tau_{R\parallel}^{L3}(walls) = 15$ ns vs. $\tau_{R\parallel}^{L3}(rod) = 23$ ns and $\tau_{R\perp}^{L3}(walls) = 39$ ns vs. $\tau_{R\perp}^{L3}(rod) = 35$ ns at $T = 353$ K. For the bulk, as seen in Figure (5.8), $\tau_R(bulk) = 9$ ns vs. $\tau_{R\perp}^{L1}(rod) = 9.8$ ns and $\tau_{R\parallel}^{L1}(rod) = 8.4$ ns.

Table 5.1: The values τ_R calculated from the COM displacement. The values correspond to three different layers across the nanopore for both the axial and radial motions at all three temperatures.

	τ_R [ps]					
	Radial			Axial		
	L1 ^a	L2 ^b	L3 ^c	L1	L2	L3
293 K	29 280	41 280	132 700	24 480	30 260	90 640
323 K	15 400	22 360	58 360	12 860	15 780	43 820
353 K	9 860	14 280	34 820	8 400	10 000	23 220

^a L1 corresponds to the farthest away from the nanorod.

^b L2 corresponds to the intermediate layer.

^c L3 corresponds to the layer at the interface.

Keeping in mind that the graphite walls' interaction with the melt is different from that of alumina, the previous results indicate that different geometries and curvatures/confinements affect the melt differently. The nanopore structure's effect on the COM displacement is the most prominent and visible at the wall layer as well as its extent on the inner and intermediate layers. When the curvature is changed (nanorod), the effect of the same type of interaction is reduced at the wall as well as for the different layers away from the rod walls. Where for the pore system, the melt is fully confined along the radial direction in two dimensions while free to diffuse along the axial direction, the rod system lacks these constraints on the chains.

To visualize the motion and conformation of the chains across the melt we follow four different chains at $T = 293$ K along the trajectory and show the snapshots at $t = 0.01, 41, 92$ and 229 ns in Figure (5.9). The black circles represent the different layers, used to calculate the dynamic properties, starting with the smallest at the rod wall at a radial distance of 5 nm from the rod center. Two of the chains (green and magenta) start with their COM in the first wall layer while

the other two start with their COM further away from the nanorod. The chains positioned away from the nanostructure move freely across the melt similar to the snapshots seen for the nanopore system in Figure (4.13). The first wall chain (1170 - magenta) starts with the majority of its monomers adsorbed to the surface while it wraps around the rod walls while the other (851 - green) has its COM in the first layer but only has a few monomers directly at the interface. Chain 1170 is stretched and is oriented along the rod walls and most importantly remains adsorbed indicating that its full desorption process is beyond the time scale of this simulation. These elongated and almost fully adsorbed chains are rare at the interface; nonetheless, examining their behavior is still important. On the other hand, chain 851 which is similar to most of the other chains in the first layer goes through the desorption process even at the lowest temperature and moves away where its center of mass crosses the first wall layer.

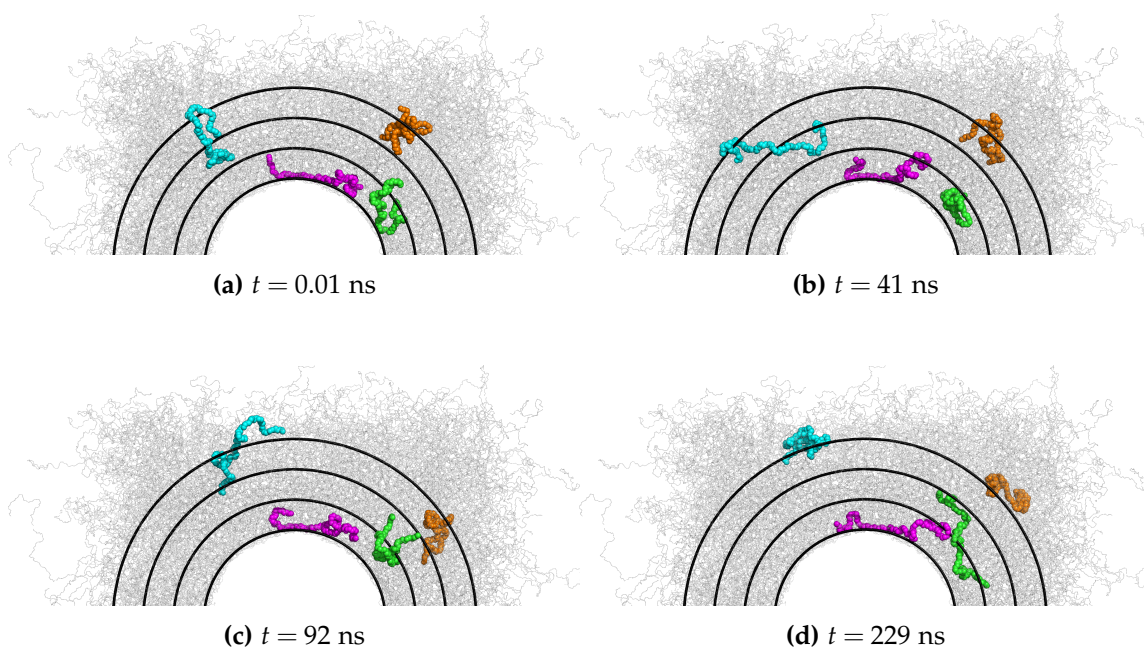


Figure 5.9: Snapshot of four different chains (green and magenta - chains 851 and 1170 / cyan and orange - chains 586 and 674) at four different times along the simulation trajectory ($T = 293$ K). The black rings indicate the different layers of size $\sim R_g$ starting with the smallest at the rod wall at a radial distance of 5 nm from the center of the rod.

5.2.2 Incoherent Neutron Scattering Function

The incoherent neutron scattering function studies single atom dynamics in the melt and is an experimentally obtainable quantity. Subsection (4.2.3) has details on the scattering function and the expressions obtained for momentum transfers

oriented parallel and perpendicular to the confinement walls. For this system we are also interested in the scattering function with \mathbf{q} along $\hat{\mathbf{e}}_r$ and $\hat{\mathbf{e}}_z$ subsequently studying the motion of the melt perpendicular and parallel to the rod walls.

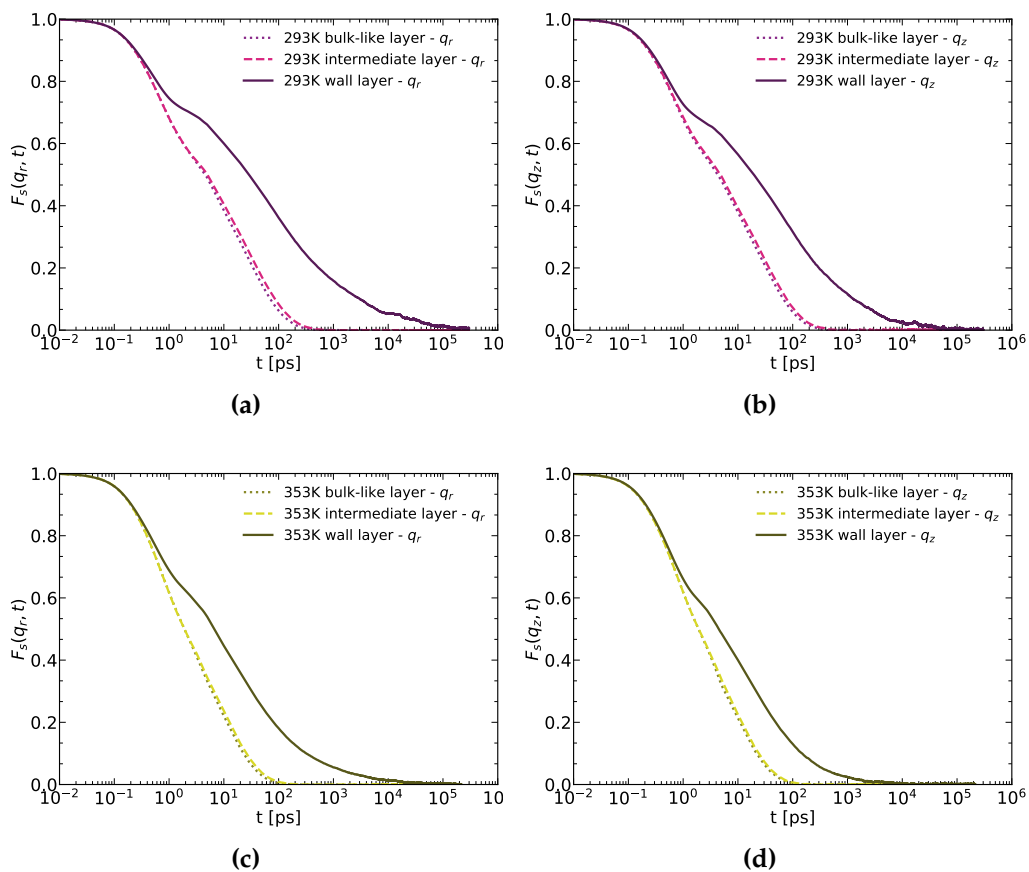


Figure 5.10: The INSF at $T = 293$ K and $T = 353$ K with momentum transfer $q_r = 12$ nm^{-1} (a,c) and $q_z = 12$ m^{-1} (b,d).

The melt is divided into three different layers across the radial direction each of size $\sim R_g$ and a monomer belongs to a specific layer if its radial position is in that layer at $t = 0$. In the nanopore system we saw that the adsorption of the monomers to the pore walls and their desorption process slow down the motion at the walls significantly and most importantly introduce a third step in the relaxation that can be observed in the scattering function. One question for the rod system would be whether the adsorption of the monomers here will have the same effect or is the interfacial layer more mobilized.

Figure (5.10) shows the incoherent neutron scattering function (INSF) for both orientations of the momentum transfer $q = 12$ nm^{-1} for $T = 293$ and 353 K. The different curves in each figure belong to the three layers across the melt. These

results show the effect of the temperature in combination with the proximity of the monomers to the rod wall on the motion in the melt. For $T = 353$ K we see the slowing down at the wall layer that is enhanced for \mathbf{q}_r . However, as we move away from the wall at that temperature bulk-like behavior starts to manifest especially for the third layer. As we decrease the temperature to $T = 293$ K all the effects seen at $T = 353$ K are amplified in particular in the wall layer. However, unlike the nanopore system, for the second and third layers, the effect of the nanorod is almost negligible indicating that the slowing down of the α -relaxation process in this system due to the nanostructure is restricted to the first interfacial layer.

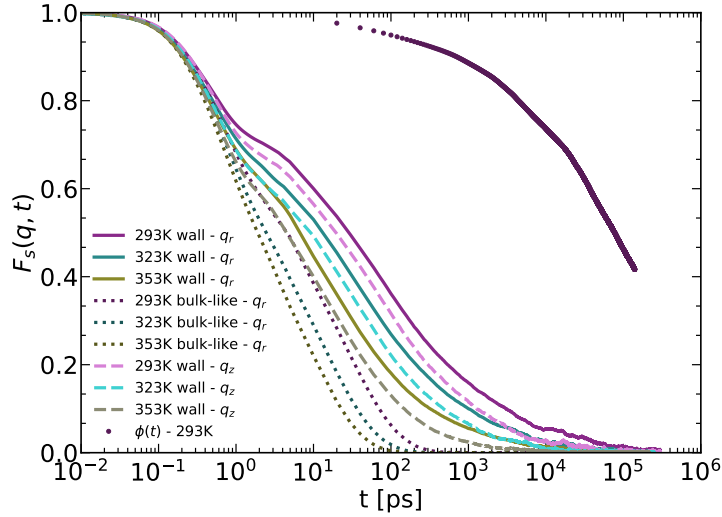


Figure 5.11: The INSF for the wall layer (solid and dashed lines) and the bulk-like layer (dotted lines) for a momentum transfer $q = 12 \text{ nm}^{-1}$. All three temperatures are included. $\Phi(t)$ is the adsorption autocorrelation function at $T = 293$ K.

Figure (5.11) shows the INSF for all three temperatures for the wall and bulk-like layers for the motion in the radial direction. The axial motion is shown for the layer at the wall (dashed lines) and $\Phi(t)$ is the adsorption autocorrelation function defined in eq.(4.8). The latter is calculated for this system starting from 10 ps; however; this is enough to study the behavior of the adsorption/desorption process. The plot containing the adsorption autocorrelation function for all three temperature can be found in Appendix (C). The motion in the axial direction ($\hat{\mathbf{e}}_z$) is slightly less affected by the nanorod than the radial motion and in com-

parison with the axial motion in the pore system. For the layer at the wall the third step in the relaxation and time scale separation is present at all temperatures. It is good to note again that for the scattering function the relaxation here also takes into consideration the motion along the rod surface in the \hat{e}_x and \hat{e}_y directions in addition to the movement away which is defined as the desorption of the monomers.

To get a more quantitative picture that would also help us to compare to the pore system, we fit the scattering function at the wall layer to a superposition of two stretched exponential (see eq. (4.23)) and the bulk-like layer to a stretched exponential (see eq.(4.9)) and extract the fitting parameters (Table (5.2)). The fitting was done for the motion perpendicular (for \mathbf{q}_r) and the table also includes values for the fitting of the adsorption autocorrelation function $\Phi(t)$ to a stretched exponential.

Table 5.2: The table on the left hand side presents the fitting parameters τ , β obtained from the stretched exponential fit to $\Phi(t)$ while the table on the right hand side presents the fitting parameters $\tau_\alpha, \beta_\alpha$ and τ_{des}, β_{des} obtained from the stretched exponential fits to $F_s(q_r, t)$ in the bulk of the melt and in the layer adjacent to the walls.

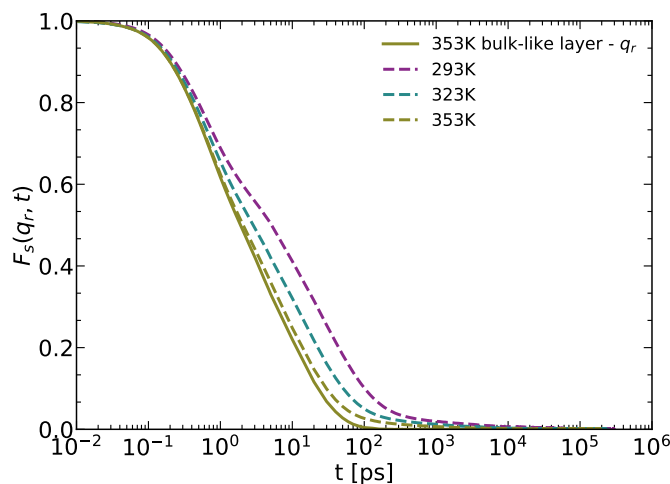
Adsorption ACF			Bulk-like		Wall				
T [K]	τ [ps]	β	T [K]	τ_α [ps]	β_α	τ_α [ps]	β_α	τ_{des} [ps]	β_{des}
353	30 375	0.446	353	4	0.520	10	0.400	479	0.298
323	51 728	0.481	323	7	0.531	32	0.307	985	0.264
293	149 110	0.413	293	13	0.505	39	0.319	1 396	0.268

$\Phi(t)$ is based on geometric criteria where a monomer is considered to be adsorbed if the chain it belongs to is in the first COM density layer (~ 1.5 nm from rod wall) and if its radial position is in the first monomer density layer (~ 0.5 nm) at $t = 0$. As the simulation time progresses the autocorrelation function will decay as the monomers desorb from the nanorod walls. Therefore, when fitting $\Phi(t)$ to a stretched exponential we can extract a relaxation time that describes the desorption process of the monomers. The exponent A in the stretched exponential is set to 1. The exponents for the stretched exponential and the superposition of two stretched exponentials for the INSF in the bulk-like and wall layers respectively, take a value from 0.9 to 1. From the parameters of the scattering function fits, the α -relaxation at the wall is again slower than that of the bulk-like layer but the difference is smaller than that found in the nanopore system. The α -relaxation values for both layers in the nanorod system are smaller when

compared to the nanopore system indicating a larger effect of the nanopore on the dynamics. τ_{des} is the time scale obtained from the scattering function and is correlated with the desorption of the monomers from the wall. In the previous system system we mentioned that τ_{des} includes not only the time scale from the motion of the monomers away from the wall but also the motion along the confinement walls explaining the discrepancy seen between τ_{des} and τ from the the adsorption autocorrelation function. Comparing the two systems, τ_{des} is an order of magnitude slower in the nanopore system at all simulated temperatures. As for the desorption process, the relaxation times indicate a much faster (almost half) desorption process than the one observed in the nanopore system. This is in agreement to the dynamical results we have seen so far for the rod and the observed extent of the rod effect.

Following this we calculate the INSF across the whole melt with momentum transfers \mathbf{q}_r and \mathbf{q}_z . Figure (5.12a) shows the latter for \mathbf{q}_r with the bulk-like layer at $T = 353$ K, while Figure (5.12b) shows the total scattering function for all three temperatures with the two directions of the momentum transfer. These two plots are important because they indicate the following:

First, the comparison between both directions of \mathbf{q} and the almost complete overlap of the two curves here but not at the wall layer indicates that the nanorod affects the motion in the radial direction more than the axial direction only at the wall layer. The second observation comes from the fact that the scattering function for the melt as a whole is almost identical to the scattering function of the bulk-like layer.



(a)

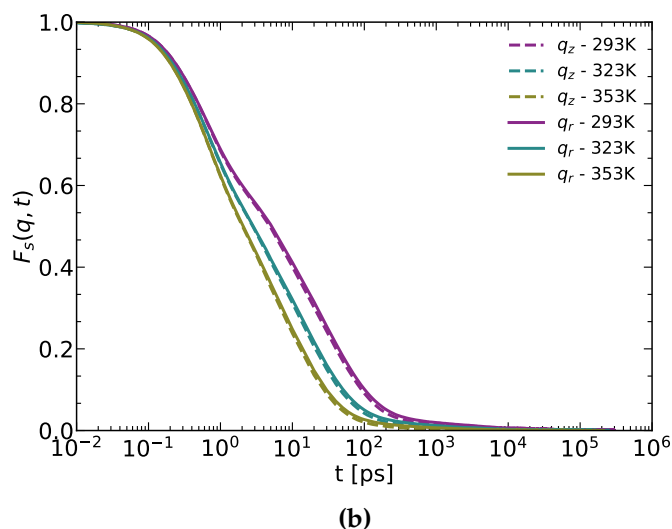


Figure 5.12: (a) Total INSF for the melt as a whole and the bulk-like layer at $T = 353$ K for \mathbf{q}_r . (b) Total INSF for the melt as a whole for all three temperatures for both directions of momentum transfer \mathbf{q}_r and \mathbf{q}_z .

The third step in the relaxation, which kicks in at the end of the plateau of the adsorption autocorrelation function and is a result of the desorption process, is almost negligible and the first time scale separation plateau can be seen slightly only for the lowest temperature. This demonstrates that the effect of the nanorod on the melt is not as strong as we have seen in the nanopore system. Apart from the few chains wrapping around the nanorod and especially at the lowest temperature, the chains and hence the monomers in the wall layer are able to desorb and escape that layer as seen also in the snapshots in Figure (5.9). The contribution of the non-desorbed chains on the melt as a whole is minute.

Finally, in this section, we study the INSF at different momentum transfers shown in Figure (5.13) for $T = 293$ K. The plots for $T = 323$ and 353 K can be found in Appendix (C). The solid lines represent the wall layer while the dashed lines are for the total INSF of the melt. For a smaller momentum transfer ($q = 4$ nm⁻¹) the second and third steps in the relaxation are dominant for the wall layer while the vibrational regime starts to become indistinguishable. The time scale separation for the total INSF at $q = 4$ nm⁻¹ is even less identifiable with the third step kicking in and decaying at much shorter times. The opposite applies for the higher momentum transfers ($q = 16$ and 24 nm⁻¹) where the vibrational regime is dominant and the additional process is not visible. Additionally, as observed for $q = 12$ nm⁻¹, the differences between the wall layer and total INSF for all

momentum transfers is broader in this system in comparison with the nanopore indicating a weaker response of the melt to the nanorod.

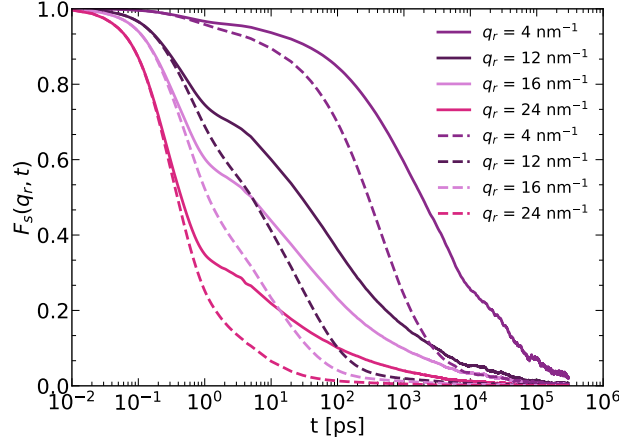


Figure 5.13: The INSF at $T = 293$ K for the monomers in the wall layer (solid) and averaged over all monomers (total INSF, dashed) for different values of the momentum transfer q_r .

Following the analysis that was done at the end of subsection (4.2.3), we study here as well the adsorbed number of monomers per chain averaged over the trajectory. Figure (5.14) shows a histogram, for all three temperatures in the rod system, of the adsorbed monomers per chain normalized by the total number of frames. This consequently displays the average number of chains (y-axis) per frame with a given number of adsorbed monomers (x-axis).

The results for the rod system are more temperature dependent than the pore system where for the former, the number of chains with adsorbed monomers decreases with the increase in temperature ($N_{ads}^{chains} = 147, 125$ and 74 as we increase the temperature). The chains belonging to the first COM layer with no adsorbed monomers are not shown in the plot; however, they are also temperature dependent. As we increase the temperature, the number of chains with zero adsorbed monomer increases where they make up 8.9, 21.9 and 37.8 % (for $T = 293, 323$ and 353 K respectively) of the average number of chains in the first COM layer. The histogram shows also a jump between the number of chains per frame with a couple of monomers adsorbed to the wall and the chains with ~ 10 monomers at the wall. For the rod system, and especially for the lowest T , the number of chains with most of their monomers adsorbed is slightly larger than those in the pore system. Despite the fact that this system has a larger number of adsorbed

chains and monomers, we have seen that they are able to desorb and escape the first layer and this is partly a consequence of the curvature of the nanorod.

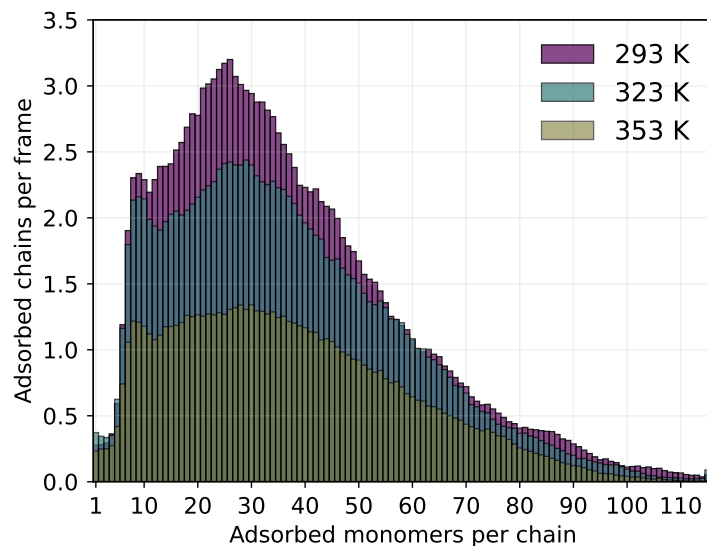


Figure 5.14: Histogram of the number of adsorbed monomers per chain in the first layer of size $\sim R_g$ for all three temperatures in the nanorod system. The total number of adsorbed monomers in each bin is normalized to the total number of frames which in turn gives us the average number of chains per frame (y-axis) with a given number of adsorbed monomers (x-axis).

Both systems show that the adsorption is due to a few chains with a large number of adsorbed monomers rather than several chains with few contacts to the surface which plays a role in the large time scales seen for the desorption process.

5.2.3 Segmental Orientational Correlation Function

In the final subsection concerning the nanorod system, we investigate the dynamics on the segmental scale by studying the relaxation of individual CH-bonds in the system based on whether they belong to *cis* or *trans* groups. To do so, we calculate the second Legendre polynomial of the orientational autocorrelation function found in eq. (4.2.4) where we define \hat{e}_i to be a unit vector along a certain C–H bond at a given time t .

Since the model used establishes a united atom to be either a CH or a CH₂, it is required to explicitly calculate the positions of the hydrogen atoms from the

stored UA positions. Section (4.2.4) includes more details on the procedure and Figure (4.23) presents an example of the calculated results. Then the melt is divided into three layers each of size $\sim R_g$ and a C–H bond belongs to a certain layer if its COM is in that layer at $t = 0$. Figure (5.15) shows the segmental orientational autocorrelation function for different layers across the melt and for both *cis* and *trans* conformers at different temperatures and layers across the melt. The inset of both plots shows the respective ACF for the bulk-like layer away from the nanorod walls. Separate plots for all three layers at each temperature for both *cis* and *trans* groups can be found in Appendix (C). As expected, the relaxation in the layer at the wall is slower than the rest of the melt. This applies to all temperatures with faster relaxation as we increase T .

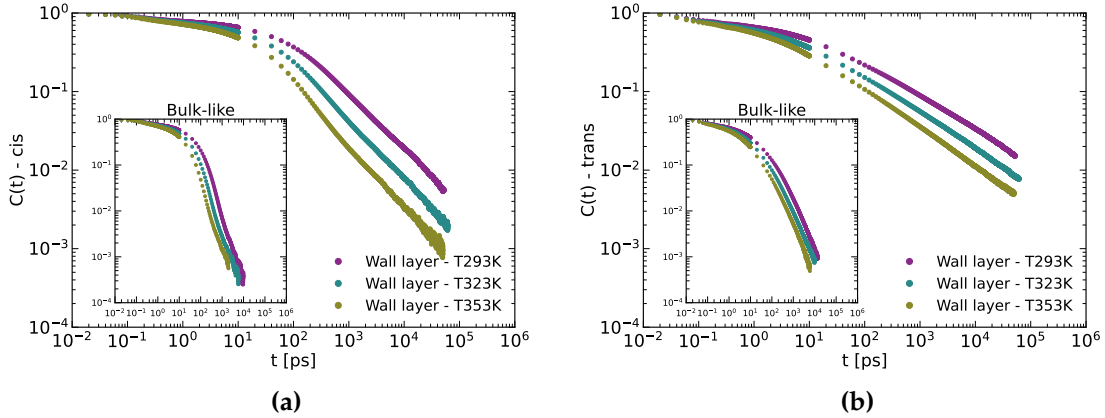


Figure 5.15: The orientational autocorrelation function of CH *cis* (a) and *trans* (b) groups for all three temperatures for the wall layer. The insets in both figures show the respective data for the bulk-like layer away from the rod walls.

The ACF exhibits the first time scale separation with a slightly longer plateau for the *cis* group. The relaxation in the bulk-like layer is also visibly faster than the one seen for the center layer in the nanopore system. To be able to compare the two systems more quantitatively and to extract experimentally obtainable data, we fit the segmental ACF to a superposition of two stretched exponentials. From the parameters of the latter (Table (C.1) contains all the fitting parameters), we can extract the correlation times τ_c defined in eq.(4.27) as well as the spin lattice relaxation times (T_1 , eqs.(4.25) and (4.26)) that can be obtained from NMR experiments. Section (4.2.4) contains more details on the parameters used to calculate T_1 and the fitting procedure. Tables (5.3) and (5.3) contain the results on the calculated T_1 and τ_c respectively. For the calculations of the spectral densities,

we use the same frequencies as in the nanopore system with $\omega_H = 1885$ MHz and $\omega_C = 141.1$ MHz.

Table 5.3: The correlation times τ_c (left) and T_1 (right) calculated from the $C - H$ bond relaxation at three different temperatures for both the *cis* and *trans* groups. The values for the bulk are taken from Ref. [92].

τ_c [ps]							nT_1 [s]						
<i>trans</i>			<i>cis</i>				<i>trans</i>			<i>cis</i>			
T [K]	nanorod		Bulk	nanorod			T [K]	nanorod			nanorod		
	bulk-like	wall		bulk-like	wall	Bulk		bulk-like	Wall	Bulk	Center	Wall	Bulk
293	124	17 689	305	87	2 446	184	293	0.85	0.56	0.61	0.66	0.35	0.37
323	65	5 818	78	46	685	61	323	1.45	0.85	1.03	1.15	0.53	0.85
353	36	3 064	37	27	341	26	353	2.11	1.08	1.95	1.83	0.81	1.7

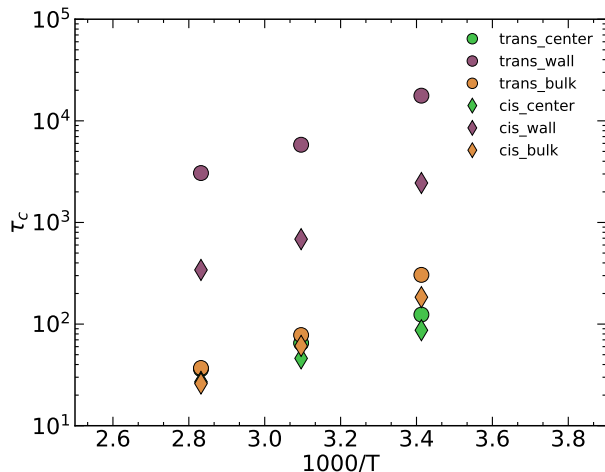


Figure 5.16: $C(t)$ autocorrelation times calculated from the integral in expression (4.27) for the nanorod system.

Figure (5.16) shows the temperature dependence of the correlation times for both *cis* and *trans* groups in the bulk, bulk-like and wall layers. The bulk-like layer correlation times are comparable to the bulk values especially at higher temperatures. For the layer at the wall, we see similar behavior to the nanopore system with larger correlation times particularly for the *trans* group. However, the temperature dependence is not so easily observed for the spin-lattice relaxation times. The latter are given in Table (5.3) along with the bulk values taken from Ref. [91,92]. The fitting is a sensitive process that can be contingent on the choice of initial values of the parameters where different sets of parameters can produce similar fits. Moreover, given the several integrations needed to calculate the spin lattice relaxation times, all these values and especially T_1 should be

considered with caution and not as strict and definitive values. Similarly to the nanopore system, as we increase the temperature, T_1 in the bulk-like region gets closer to the PBD bulk values. The latter can be a result of the slight difference between the densities in the center at different different temperatures ($\rho_{center} \simeq 870 \text{ kg/m}^3$) and their respective bulk values.

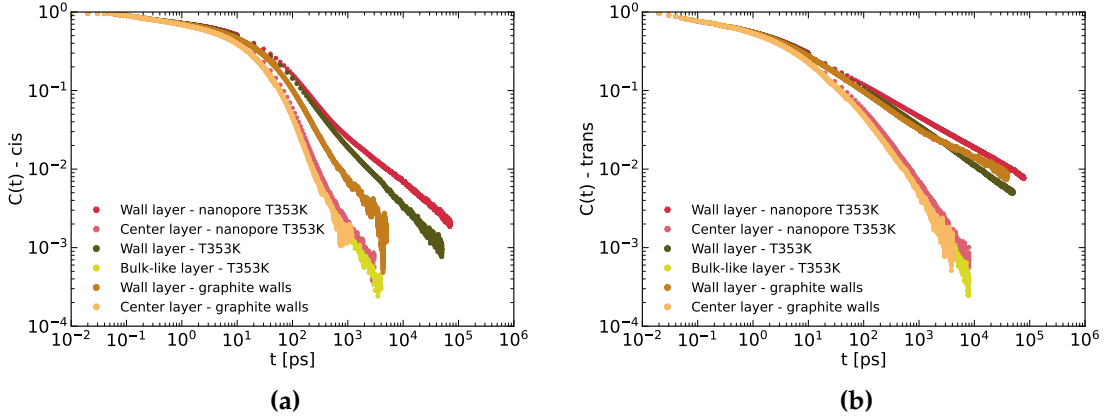


Figure 5.17: The correlation function (**a** *cis* and **b** *trans*) at $T = 353 \text{ K}$ for the wall layer and furthest layer from the rod for the nanopore (pink), parallel graphite walls taken from Ref. [24] (orange) and the nanorod (green).

Figure (5.17) shows the conformational ACF for three different systems: nanopore (red hexagons), parallel graphite walls (orange circles) and the nanorod system (green circles) at $T = 353 \text{ K}$ (The comparison between the rod and pore systems for $T = 293$ and 323 K can be found in Appendix (C)). For the layer affected least by the confinement, there is a similar behavior in both groups for all three systems with a slight increase in the relaxation for the cylindrical geometries especially the nanopore. However, for the wall layer the difference is significant. This can also be seen clearly in the values of τ_c where the effect of the nanopore is the most significant.

In this section, we discussed the dynamical effects introduced by the alumina nanorod on the melt. Starting with the center of mass mean squared displacement, the nanorod creates a layer at the interface with a size $\sim R_g$ of the PBD chains that demonstrates slower dynamics than the rest of the melt. The effect is extended to both directions studied (axial and radial) with a slightly stronger effect on the radial motion. The furthest layer from the wall is found to be comparable to the bulk and starts to show diffusive behavior given our simulation

times. After a certain time the centers of mass at the wall which are defined by having their radial position in that layer at $t = 0$ appear to be able to escape that layer (this can also be seen in the snapshots of chains in different layers of the melt) and exhibit faster dynamics especially at higher temperatures. This indicates that most of the adsorbed monomers/chains in this geometry undergo the desorption process in the time scale of our simulation. Consequently we study the adsorption autocorrelation function alongside the incoherent neutron scattering function. The INSF is calculated for two directions of the momentum transfer: parallel and perpendicular to the rod walls for different layers and for the melt as a whole. The layer at the wall shows again slower dynamics with more pronounced time scale separations for lower temperatures. For both \mathbf{q}_r and \mathbf{q}_z a third step in the relaxation is introduced and can be seen clearly in the scattering function. This step kicks in at end of the plateau of the adsorption autocorrelation function indicating the causal effect of the latter on the dynamics. The scattering function for the melt as a whole shows almost identical behavior for \mathbf{q}_r and \mathbf{q}_z . Another important observation is the dissipation of the third step in the relaxation process for the melt as a whole indicating the small-scale effect of the rod on the system. Finally, and similar to what we have seen in the nanopore confinement but to a lesser extent, the segmental mobility at the wall is hindered by the confinement in the interfacial layer. This can be observed by studying the orientational autocorrelation function of individual C–H bonds. The correlation times increase as we get closer to the confinement especially at lower temperatures.

Chapter 6

Conclusion and Outlook

The preceding two chapters presented the effects of two different types of confinements on a polymer melt. To better understand how nanofillers in polymer nanocomposites affect the melt, we study the impact of both nanoscopic confinement and curvature on the dynamics and properties of a chemically realistic united atom model of a 1,4-Polybutadiene melt using Molecular Dynamics simulations. Therefore, we divide the work into two systems: one with a PBD melt confined in a cylindrical alumina pore (Chapter 4) and the other with a PBD surrounding an alumina cylindrical nanorod (Chapter 5). Alumina was chosen because it represents a good controlled confinement and microporous alumina with nano-sized diameters is experimentally accessible.

Studying two separate systems allows us to first understand any alterations in the melts in each type of confinement and to compare the effects of the two types of curvatures. The latter along with our simulations at three different temperatures, experiments on melts in cylindrical pores and previous simulations on the same model of PBD between parallel walls (graphite) brings us closer to interpreting the factors that influence the changes in both the structure and dynamics.

As a first step, we start with the density profiles for the monomers and chains in the system and we see for both systems a layering across the radial direction for both with length scales \sim size of monomer (σ) and \sim gyration radius (R_g) respectively. The fact that both layering profiles for both systems are almost identical can only mean that for nanostructures of the same size, i.e. contact area with the melt, the density profile is a result of the melt-wall interactions. Such a layering profile allows us to make an assumption of the existence of an ordering on the segment and chain scales as well as the possibility of having an adsorbed

layer of monomers to the wall. Whether and how the latter two affect the melt or different layers of the melt is what we continue to discuss.

The melt, in both systems, does in fact exhibit ordering on both the segment and chain scales. The segmental ordering is obtained by examining the angle between the double bonds and both the axial and radial directions. For both types of curvatures the double bonds, along the radial direction, show a layering that decreases in amplitude with a preference to lie perpendicular to the normal to the surface and along the pore/rod walls as seen in Figure (6.1).

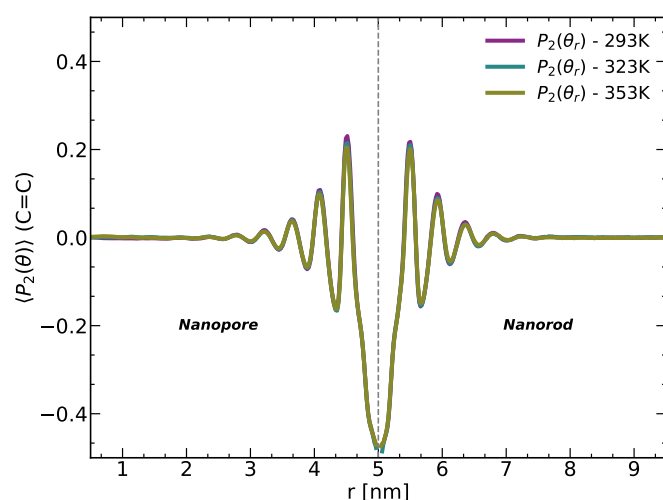


Figure 6.1: Orientational ordering of the double bonds in the chains given by the Legendre polynomial of the angle between the double bonds and the radial direction. The plots show P_2 for all three temperatures and for both the nanopore and nanorod systems. The vertical dashed line represents roughly the radial position of the pore/rod wall.

Their alignment with the axis of the pore/rod increases with the increase in temperature. The chain ordering on the other hand is obtained by studying the gyration tensor along with its eigenvalues that represent the principal axes of the gyration ellipsoid. The orientation (eigenvectors of the largest eigenvalue) gives more information on the preferred alignment of the chains. Similar to the simulations on a PBD melt between graphite walls, the chains in the nanopore system do not exhibit any stretching at the wall except for the lowest temperature and in that layer the chains orient themselves closer to the axis of the pore. The nanorod system's chains, on the other hand, behave more like what has been observed for spherical nanoparticles. Directly at the interface, there exists a small number of chains that stretch and wrap along the rod walls resulting in an increase in the

relative shape anisotropy and the gyration radius in that layer. For these chains their centers of mass are located inside the rod and they are oriented to lie in the (r, φ) plane. The chains directly beyond that first small layer show similar behavior to the ones in the nanopore system. It is also good to note that for all the structural analysis bulk-like behavior is observed in the center or beyond a certain distance from the nanostructure.

So far we can conclude that the structure in the melt is an interplay between curvature/geometry and type of interaction. The type of interaction between our PBD melt and the alumina attracts the monomers close to the wall and creates a density layering extending to ~ 2.5 nm away from the walls. Now given that the chains and monomers are attracted and adsorbed to the wall (will be mentioned later), the curvature/geometry plays an important role in the orientational ordering. The fact that we have a two dimensional confinement restricts the ordering to be perpendicular to the normal to the surface and along the walls. The only exception to the latter is the small number of chains that stretch and wrap around the rod which cannot be observed in the pore system. The temperature here plays a role with the "magnitude" of orientational ordering especially for the nanopore system.

This brings us to the effect of the confinement on the dynamics of the melt. For all the dynamical analysis, we study three different layers along the radial direction each of size $\sim R_g$ of our PBD chains. Previously, it was mentioned that the density layering suggests an adsorbed layer of monomers/chains at the wall. If that were true, we should be able to see the implications of that on the first wall layer. What are those implications and how is the mobility altered in our systems is what the dynamical analysis should answer. The mean squared displacement shows a slower motion of the layer closest to the wall with respect to the rest of the melt. The monomer and chain motion are affected in both the radial and axial directions. The latter two are comparable for the nanopore system while the motion in the radial direction is affected slightly more than its axial counterpart for the nanorod. The other two layers show similar behavior; however, the ones in the nanorod system are comparable to the bulk especially at the higher temperatures. The quantitative characteristic time τ_R obtained from the MSD shows the slowest motion to be for the pore interface layer which gets amplified with the decrease in temperature, followed by the layer on the wall-rod interface. Figure (6.2) shows the center of mass MSD along the axial direction at $T = 293$ and 353 K for the layers closest and farthest from the wall for both systems. One

can see the slower motion of the chain centers of mass in the pore system in for both layers and especially as we go to lower temperatures.

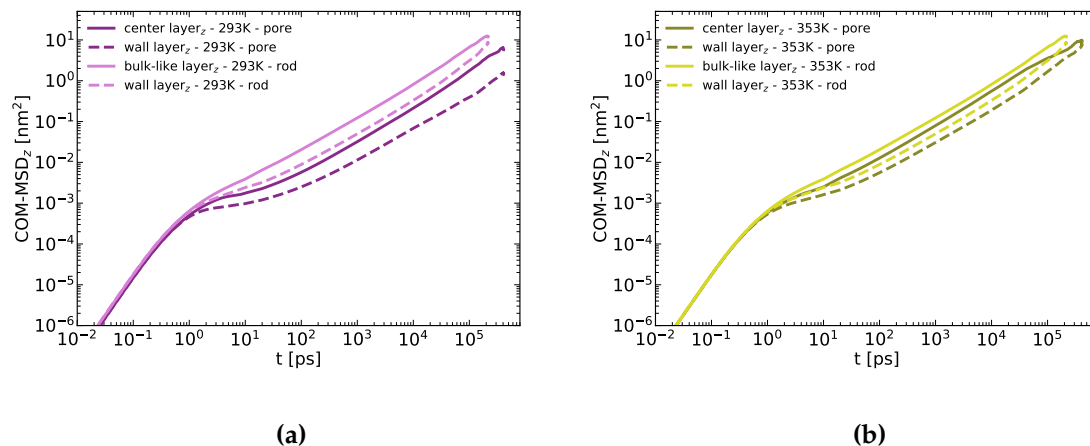


Figure 6.2: A comparison of the center of mass mean squared displacement along the axial direction of both systems (nanopore vs. nanorod). The plots the MSD at $T = 293$ and 353 K for the layers closest and furthest from the wall.

The incoherent neutron scattering function, an experimentally obtainable analysis, introduces another dynamical process brought about by the confinement. For the layer at the wall and for both systems (in the radial and axial motion), a third step in the relaxation process is detected. Studied along with the adsorption autocorrelation function we suggest that this extra time scale separation is brought about by the desorption process. The latter appears to be affected by the temperature of the system, where in the nanopore system specifically and for $T = 293$ K the desorption process is beyond the time span of the simulations (400 ns). By studying the value of adsorbed chains and monomers to the confinement walls, we find out that for both system there are a few number of chains with several monomers adsorbed to the surface rather than several chains with a few contacts. To be able to compare to experiments whose results also concur with our findings, we study the INSF for the melt as a whole rather than for different layers. For the nanopore, the extra third step is still present and easily distinguishable indicating the strong effect of the cylindrical pore confinement on the melt. The results on the nanorod system, on the other hand, indicate that apart from a number of chains that take longer than our simulation time to desorb from the wall, the INSF for the whole melt shows a behavior closer to that of the

bulk (a comparison of both can be found in Figure (6.3)).

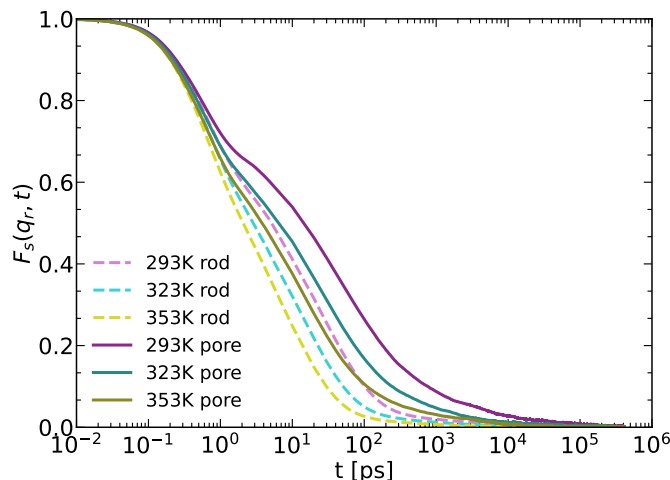


Figure 6.3: The incoherent neutron scattering function (with \mathbf{q}_r) for the whole melt for both systems at all three temperatures.

This can also be detected in the MSD curves where the monomers in the wall layer appear to desorb, leave the first layer and show an increase in their mobility. Therefore, the confinement in both systems creates a layer whose dynamics are different from the rest of the melt. However, the effect on the nanorod layer has a time scale and magnitude smaller than its counterpart for the nanopore. For the latter and especially at lower temperatures, there seems to exist what has been in previous work been described as an "immobilized" layer, at least when considering our simulation times.

The segmental dynamics are studied through the orientational autocorrelation function $C(t)$ of individual C–H bonds. This is another experimentally obtainable quantity given that the spin-lattice relaxation times that can be measured in NMR experiments can also be calculated from $C(t)$. The results of this analysis coincide with our previous observations on both systems. For both, the calculated correlation times τ_c and T_1 (relaxation rate $1/T_1$), the segmental mobility is slowed down for the layer at the wall and slightly more for the nanopore system.

All the quantitative values obtained from the mean squared displacement, the scattering function and the orientational autocorrelation function show a similar difference between the bulk and wall layers but exhibit even slower behavior for the nanopore system especially at lower temperatures. When comparing with the parallel wall confinement, the comparison varies but one should keep in mind

that the latter is graphite walls which means a different type of interaction. The effects observed in the dynamics cannot be attributed to one factor only. The adsorption of the monomers is in this setup a result of the interaction as we have stated before. We do not study the effect of the size of the nanostructure thus we cannot conclude on the latter's effect. The desorption process; however, is influenced greatly by both the temperature and the type of curvature and its effects can be seen on the motion on several scales. It would be good to note that the curvature is not just a definition of "concave" or "convex" but also the fact that one system has a melt fully confined in two dimensions and the other melt's motion is basically unrestricted in the same two dimensions.

Finally, in order to gain a comprehensive understanding of nano-scale confinement and the associated geometry, further research is necessary to explore future avenues in the field. Investigating the effects of parallel wall confinement with alumina structures would be a logical next step. By studying this type of interaction, researchers can deepen their understanding of the behavior of confined melts and the impact of varying confinement geometries.

Another crucial aspect that warrants investigation is the influence of nanostructure size on the properties of confined melts. Although the current study did not focus on this parameter, it represents an important factor that can significantly impact the behavior and dynamics of confined systems.

On the experimental front, replicating the observed results would be a valuable endeavor. By reproducing these findings, researchers can validate the conclusions drawn from the computational study and ensure the robustness of the obtained results. Furthermore, experimental replication would open up opportunities to extend and expand upon the conclusions, providing a more comprehensive understanding of the system under investigation.

Appendix A

GROMACS Topology File

An excerpt of the topology file of one chain of 1,4-polybutadiene that defines all the necessary parameters for the GRO-
MACS software.

```

1 ; OPT=
2 [ defaults ]
3 ; nbfunc      comb-rule   gen-pairs   fudgeLJ   fudgeQQ
4 1             2           no          1.0       1.0
5
6 [ atomtypes ]
7 ; atom_type   mass      charge     ptype     sigma[nm]  eps[kJ/mol]
8 CH2           14.027   0.000     A         0.400904   0.391806
9 CH1           13.019   0.000     A         0.38542    0.418593
10 ALU          26.982   0.000     A         0.311797   2.360997
11 OXY          15.999  -0.000     A         0.323102   0.936000
12
13 [ nonbond_params ]
14 ; i           j           func(LJ)   sigma[nm]  eps[kJ/mol]
15 CH2          CH1        1          0.379256   0.424870
16 ALU          ALU        1          0.311797   2.360997
17 OXY          OXY        1          0.323102   0.936000
18 ALU          OXY        1          0.317449   1.486571

```

```

19 [ moleculetype ]
20 ;Name        nrexcl
21 P1           3
22
23
24 [ atoms ]
25 ; nr      type  resnr  resnam  atom  cgnr  chrg  mass
26 1         CH2   1      PBD     CH2   1     0.00  14.027
27 2         CH1   1      PBD     CH1   2     0.00  13.019
28 3         CH1   1      PBD     CH1   3     0.00  13.019
29 4         CH2   1      PBD     CH2   4     0.00  14.027
30 5         CH2   1      PBD     CH2   5     0.00  14.027
31 6         CH1   1      PBD     CH1   6     0.00  13.019
32 7         CH1   1      PBD     CH1   7     0.00  13.019
33 8         CH2   1      PBD     CH2   8     0.00  14.027
34 9         CH2   1      PBD     CH2   9     0.00  14.027
35 10        CH1   1      PBD     CH1  10     0.00  13.019
36 11        CH1   1      PBD     CH1  11     0.00  13.019

```

37	12	CH2	1	PBD	CH2	12 0.00 14.027	57	CH2	1	PBD	CH2	57 0.00 14.027
38	13	CH2	1	PBD	CH2	13 0.00 14.027	58	CH1	1	PBD	CH1	58 0.00 13.019
39	14	CH1	1	PBD	CH1	14 0.00 13.019	59	CH1	1	PBD	CH1	59 0.00 13.019
40	15	CH1	1	PBD	CH1	15 0.00 13.019	60	CH2	1	PBD	CH2	60 0.00 14.027
41	16	CH2	1	PBD	CH2	16 0.00 14.027	61	CH2	1	PBD	CH2	61 0.00 14.027
42	17	CH2	1	PBD	CH2	17 0.00 14.027	62	CH1	1	PBD	CH1	62 0.00 13.019
43	18	CH1	1	PBD	CH1	18 0.00 13.019	63	CH1	1	PBD	CH1	63 0.00 13.019
44	19	CH1	1	PBD	CH1	19 0.00 13.019	64	CH2	1	PBD	CH2	64 0.00 14.027
45	20	CH2	1	PBD	CH2	20 0.00 14.027	65	CH2	1	PBD	CH2	65 0.00 14.027
46	21	CH2	1	PBD	CH2	21 0.00 14.027	66	CH1	1	PBD	CH1	66 0.00 13.019
47	22	CH1	1	PBD	CH1	22 0.00 13.019	67	CH1	1	PBD	CH1	67 0.00 13.019
48	23	CH1	1	PBD	CH1	23 0.00 13.019	68	CH2	1	PBD	CH2	68 0.00 14.027
49	24	CH2	1	PBD	CH2	24 0.00 14.027	69	CH2	1	PBD	CH2	69 0.00 14.027
50	25	CH2	1	PBD	CH2	25 0.00 14.027	70	CH1	1	PBD	CH1	70 0.00 13.019
51	26	CH1	1	PBD	CH1	26 0.00 13.019	71	CH1	1	PBD	CH1	71 0.00 13.019
52	27	CH1	1	PBD	CH1	27 0.00 13.019	72	CH2	1	PBD	CH2	72 0.00 14.027
53	28	CH2	1	PBD	CH2	28 0.00 14.027	73	CH2	1	PBD	CH2	73 0.00 14.027
54	29	CH2	1	PBD	CH2	29 0.00 14.027	74	CH1	1	PBD	CH1	74 0.00 13.019
55	30	CH1	1	PBD	CH1	30 0.00 13.019	75	CH1	1	PBD	CH1	75 0.00 13.019
56	31	CH1	1	PBD	CH1	31 0.00 13.019	76	CH2	1	PBD	CH2	76 0.00 14.027
57	32	CH2	1	PBD	CH2	32 0.00 14.027	77	CH2	1	PBD	CH2	77 0.00 14.027
58	33	CH2	1	PBD	CH2	33 0.00 14.027	78	CH1	1	PBD	CH1	78 0.00 13.019
59	34	CH1	1	PBD	CH1	34 0.00 13.019	79	CH1	1	PBD	CH1	79 0.00 13.019
60	35	CH1	1	PBD	CH1	35 0.00 13.019	80	CH2	1	PBD	CH2	80 0.00 14.027
61	36	CH2	1	PBD	CH2	36 0.00 14.027	81	CH2	1	PBD	CH2	81 0.00 14.027
62	37	CH2	1	PBD	CH2	37 0.00 14.027	82	CH1	1	PBD	CH1	82 0.00 13.019
63	38	CH1	1	PBD	CH1	38 0.00 13.019	83	CH1	1	PBD	CH1	83 0.00 13.019
64	39	CH1	1	PBD	CH1	39 0.00 13.019	84	CH2	1	PBD	CH2	84 0.00 14.027
65	40	CH2	1	PBD	CH2	40 0.00 14.027	85	CH2	1	PBD	CH2	85 0.00 14.027
66	41	CH2	1	PBD	CH2	41 0.00 14.027	86	CH1	1	PBD	CH1	86 0.00 13.019
67	42	CH1	1	PBD	CH1	42 0.00 13.019	87	CH1	1	PBD	CH1	87 0.00 13.019
68	43	CH1	1	PBD	CH1	43 0.00 13.019	88	CH2	1	PBD	CH2	88 0.00 14.027
69	44	CH2	1	PBD	CH2	44 0.00 14.027	89	CH2	1	PBD	CH2	89 0.00 14.027
70	45	CH2	1	PBD	CH2	45 0.00 14.027	90	CH1	1	PBD	CH1	90 0.00 13.019
71	46	CH1	1	PBD	CH1	46 0.00 13.019	91	CH1	1	PBD	CH1	91 0.00 13.019
72	47	CH1	1	PBD	CH1	47 0.00 13.019	92	CH2	1	PBD	CH2	92 0.00 14.027
73	48	CH2	1	PBD	CH2	48 0.00 14.027	93	CH2	1	PBD	CH2	93 0.00 14.027
74	49	CH2	1	PBD	CH2	49 0.00 14.027	94	CH1	1	PBD	CH1	94 0.00 13.019
75	50	CH1	1	PBD	CH1	50 0.00 13.019	95	CH1	1	PBD	CH1	95 0.00 13.019
76	51	CH1	1	PBD	CH1	51 0.00 13.019	96	CH2	1	PBD	CH2	96 0.00 14.027
77	52	CH2	1	PBD	CH2	52 0.00 14.027	97	CH2	1	PBD	CH2	97 0.00 14.027
78	53	CH2	1	PBD	CH2	53 0.00 14.027	98	CH1	1	PBD	CH1	98 0.00 13.019
79	54	CH1	1	PBD	CH1	54 0.00 13.019	99	CH1	1	PBD	CH1	99 0.00 13.019
80	55	CH1	1	PBD	CH1	55 0.00 13.019	100	CH2	1	PBD	CH2	100 0.00 14.027
81	56	CH2	1	PBD	CH2	56 0.00 14.027	101	CH2	1	PBD	CH2	101 0.00 14.027

127	102	CH1	1	PBD	CH1	102	0.00	13.019	172	28	29	1	0.15300
128	103	CH1	1	PBD	CH1	103	0.00	13.019	173	29	30	1	0.15000
129	104	CH2	1	PBD	CH2	104	0.00	14.027	174	30	31	1	0.13400
130	105	CH2	1	PBD	CH2	105	0.00	14.027	175	31	32	1	0.15000
131	106	CH1	1	PBD	CH1	106	0.00	13.019	176	32	33	1	0.15300
132	107	CH1	1	PBD	CH1	107	0.00	13.019	177	33	34	1	0.15000
133	108	CH2	1	PBD	CH2	108	0.00	14.027	178	34	35	1	0.13400
134	109	CH2	1	PBD	CH2	109	0.00	14.027	179	35	36	1	0.15000
135	110	CH1	1	PBD	CH1	110	0.00	13.019	180	36	37	1	0.15300
136	111	CH1	1	PBD	CH1	111	0.00	13.019	181	37	38	1	0.15000
137	112	CH2	1	PBD	CH2	112	0.00	14.027	182	38	39	1	0.13400
138	113	CH2	1	PBD	CH2	113	0.00	14.027	183	39	40	1	0.15000
139	114	CH1	1	PBD	CH1	114	0.00	13.019	184	40	41	1	0.15300
140	115	CH1	1	PBD	CH1	115	0.00	13.019	185	41	42	1	0.15000
141	116	CH2	1	PBD	CH2	116	0.00	14.027	186	42	43	1	0.13400
142									187	43	44	1	0.15000
143									188	44	45	1	0.15300
144									189	45	46	1	0.15000
145									190	46	47	1	0.13400
146									191	47	48	1	0.15000
147									192	48	49	1	0.15300
148									193	49	50	1	0.15000
149									194	50	51	1	0.13400
150									195	51	52	1	0.15000
151									196	52	53	1	0.15300
152									197	53	54	1	0.15000
153									198	54	55	1	0.13400
154									199	55	56	1	0.15000
155									200	56	57	1	0.15300
156									201	57	58	1	0.15000
157									202	58	59	1	0.13400
158									203	59	60	1	0.15000
159									204	60	61	1	0.15300
160									205	61	62	1	0.15000
161									206	62	63	1	0.13400
162									207	63	64	1	0.15000
163									208	64	65	1	0.15300
164									209	65	66	1	0.15000
165									210	66	67	1	0.13400
166									211	67	68	1	0.15000
167									212	68	69	1	0.15300
168									213	69	70	1	0.15000
169									214	70	71	1	0.13400
170									215	71	72	1	0.15000
171									216	72	73	1	0.15300

[constraints]
; ai aj type(1=coval.) b0[nm]

APPENDIX A. GROMACS TOPOLOGY FILE

```

307 45 46 47 2 125.89602 570.25755 352 90 91 92 2 125.89602 570.25755
308 46 47 48 2 125.89602 570.25755 353 91 92 93 2 111.65229 557.24591
309 47 48 49 2 111.65229 557.24591 354 92 93 94 2 111.65229 557.24591
310 48 49 50 2 111.65229 557.24591 355 93 94 95 2 125.89602 570.25755
311 49 50 51 2 125.89602 570.25755 356 94 95 96 2 125.89602 570.25755
312 50 51 52 2 125.89602 570.25755 357 95 96 97 2 111.65229 557.24591
313 51 52 53 2 111.65229 557.24591 358 96 97 98 2 111.65229 557.24591
314 52 53 54 2 111.65229 557.24591 359 97 98 99 2 125.89602 570.25755
315 53 54 55 2 125.89602 570.25755 360 98 99 100 2 125.89602 570.25755
316 54 55 56 2 125.89602 570.25755 361 99 100 101 2 111.65229 557.24591
317 55 56 57 2 111.65229 557.24591 362 100 101 102 2 111.65229 557.24591
318 56 57 58 2 111.65229 557.24591 363 101 102 103 2 125.89602 570.25755
319 57 58 59 2 125.89602 570.25755 364 102 103 104 2 125.89602 570.25755
320 58 59 60 2 125.89602 570.25755 365 103 104 105 2 111.65229 557.24591
321 59 60 61 2 111.65229 557.24591 366 104 105 106 2 111.65229 557.24591
322 60 61 62 2 111.65229 557.24591 367 105 106 107 2 125.89602 570.25755
323 61 62 63 2 125.89602 570.25755 368 106 107 108 2 125.89602 570.25755
324 62 63 64 2 125.89602 570.25755 369 107 108 109 2 111.65229 557.24591
325 63 64 65 2 111.65229 557.24591 370 108 109 110 2 111.65229 557.24591
326 64 65 66 2 111.65229 557.24591 371 109 110 111 2 125.89602 570.25755
327 65 66 67 2 125.89602 570.25755 372 110 111 112 2 125.89602 570.25755
328 66 67 68 2 125.89602 570.25755 373 111 112 113 2 111.65229 557.24591
329 67 68 69 2 111.65229 557.24591 374 112 113 114 2 111.65229 557.24591
330 68 69 70 2 111.65229 557.24591 375 113 114 115 2 125.89602 570.25755
331 69 70 71 2 125.89602 570.25755 376 114 115 116 2 125.89602 570.25755
332 70 71 72 2 125.89602 570.25755 377 114 115 116 2 125.89602 570.25755
333 71 72 73 2 111.65229 557.24591 378 114 115 116 2 125.89602 570.25755
334 72 73 74 2 111.65229 557.24591 379 114 115 116 2 125.89602 570.25755
335 73 74 75 2 125.89602 570.25755 380 114 115 116 2 125.89602 570.25755
336 74 75 76 2 125.89602 570.25755 381 114 115 116 2 125.89602 570.25755
337 75 76 77 2 111.65229 557.24591 382 114 115 116 2 125.89602 570.25755
338 76 77 78 2 111.65229 557.24591 383 114 115 116 2 125.89602 570.25755
339 77 78 79 2 125.89602 570.25755 384 114 115 116 2 125.89602 570.25755
340 78 79 80 2 125.89602 570.25755 385 114 115 116 2 125.89602 570.25755
341 79 80 81 2 111.65229 557.24591 386 114 115 116 2 125.89602 570.25755
342 80 81 82 2 111.65229 557.24591 387 114 115 116 2 125.89602 570.25755
343 81 82 83 2 125.89602 570.25755 388 114 115 116 2 125.89602 570.25755
344 82 83 84 2 125.89602 570.25755 389 114 115 116 2 125.89602 570.25755
345 83 84 85 2 111.65229 557.24591 390 114 115 116 2 125.89602 570.25755
346 84 85 86 2 111.65229 557.24591 391 114 115 116 2 125.89602 570.25755
347 85 86 87 2 125.89602 570.25755 392 114 115 116 2 125.89602 570.25755
348 86 87 88 2 125.89602 570.25755 393 114 115 116 2 125.89602 570.25755
349 87 88 89 2 111.65229 557.24591 394 114 115 116 2 125.89602 570.25755
350 88 89 90 2 111.65229 557.24591 395 114 115 116 2 125.89602 570.25755
351 89 90 91 2 125.89602 570.25755 396 114 115 116 2 125.89602 570.25755

```

```

[ dihedrals ]
; =====
; BEGINNING OF DIHEDRALS
; =====
; PBD with 13 cis (45%) and 16 trans (55%) states n=1 p=1
; TORSTABLE sequence
; -> 1101001110111101100000100101 with 1=trans and 0=cis
; =====
; NOTE: RYCKAERT-BELLEMANS function in gromacs defined as:
; V=Sum[Cn*cos(ψi)^n], where ψi=phi-180
; Hence, C1, C3 and C5 multiplied by -1 here
; i k1..k6 in kcal/mol
; 1 0 24.0111 0 0 0
; 2 0 24.0111 0 0 0
; 3 0.860396 -0.0400184 1.16053 0.160074 0.380176 -0.120055
; 4 -0.240111 -0.730336 2.3811 0.0800369 0.0900415 -0.0600277
; 5 -0.990456 -0.620285 -4.04187 -0.0700323 -0.250116 -0.190088
; Parameters of torsion potentials from phd of S. Krushev

```

```

397 ; nr k1 k2 k3 k4 k5 k6 (in K)
398 ; 1 0 12083.3 0 0 0
399 ; 2 0 12083.3 0 0 0
400 ; 3 432.984 -20.1388 584.025 80.5552 191.319 -60.4164
401 ; 4 -120.833 -367.533 1198.26 40.2776 45.3123 -30.2082
402 ; 5 -498.435 -312.151 -2034.02 -35.2429 -125.868 -95.6659
403
404 ; Expansion coefficients for RYCKAERT-BELLEMANS function from ki[j]
405 ; (note: k6=0)
406 ; nr CO C1 C2 C3 C4 C5 (in K)
407 ; 1 12083.3 0 -12083.3 0 0
408 ; 2 12083.3 0 -12083.3 0 0
409 ; 3 584.025 -181.248 342.36 -745.14 -322.221 1530.55
410 ; 4 193.837 -1744.53 528.643 1943.4 -161.11 362.498
411 ; 5 -1641.31 2487.14 171.179 -2809.36 140.972 -1006.94
412
413 ; Expansion coefficients for RYCKAERT-BELLEMANS function from ki[j]
414 ; (note: k6=0)
415 ; nr CO C1 C2 C3 C4 C5 (in kJ/mol)
416 ; 1 100.462 0 -100.462 0 0
417 ; 2 100.462 0 -100.462 0 0
418 ; 3 4.85568 -1.50692 2.84643 -6.19521 -2.67899 12.7253
419 ; 4 1.61159 -14.5043 4.39523 16.1577 -1.3395 3.01387
420 ; 5 -13.6461 20.6785 1.42321 -23.3575 1.17206 -8.37189
421 ; =====
422
423 ; =====
424 ; Alpha-cis and -trans potentials (nr=3,4 from Table 2.4 of Krushev)
425 ; PROPER DIHEDRALS RYCKAERT-BELLEMANS FUNCTION
426 ; i j k l type(3=RB-DIH.) CO,C1,C2,C3,C4,C5 (in kJ/mol)
427 2 3 4 5 3 1.61159 -14.5043 4.39523 16.1577 -1.3395 3.01387
428 4 5 6 7 3 1.61159 -14.5043 4.39523 16.1577 -1.3395 3.01387
429 6 7 8 9 3 1.61159 -14.5043 4.39523 16.1577 -1.3395 3.01387
430 8 9 10 11 3 4.85568 -1.50692 2.84643 -6.19521 -2.67899 12.7253
431 10 11 12 13 3 4.85568 -1.50692 2.84643 -6.19521 -2.67899 12.7253
432 12 13 14 15 3 1.61159 -14.5043 4.39523 16.1577 -1.3395 3.01387
433 14 15 16 17 3 1.61159 -14.5043 4.39523 16.1577 -1.3395 3.01387
434 16 17 18 19 3 4.85568 -1.50692 2.84643 -6.19521 -2.67899 12.7253
435 18 19 20 21 3 4.85568 -1.50692 2.84643 -6.19521 -2.67899 12.7253
436 20 21 22 23 3 4.85568 -1.50692 2.84643 -6.19521 -2.67899 12.7253
437 22 23 24 25 3 4.85568 -1.50692 2.84643 -6.19521 -2.67899 12.7253
438 24 25 26 27 3 1.61159 -14.5043 4.39523 16.1577 -1.3395 3.01387
439 26 27 28 29 3 1.61159 -14.5043 4.39523 16.1577 -1.3395 3.01387
440 28 29 30 31 3 1.61159 -14.5043 4.39523 16.1577 -1.3395 3.01387
441 30 31 32 33 3 1.61159 -14.5043 4.39523 16.1577 -1.3395 3.01387
442
443 ; =====
444 ; Alpha-cis and -trans potentials (nr=3,4 from Table 2.4 of Krushev)
445 ; PROPER DIHEDRALS RYCKAERT-BELLEMANS FUNCTION
446 ; i j k l type(3=RB-DIH.) CO,C1,C2,C3,C4,C5 (in kJ/mol)
447 32 33 34 35 3 1.61159 -14.5043 4.39523 16.1577 -1.3395 3.01387
448 34 35 36 37 3 1.61159 -14.5043 4.39523 16.1577 -1.3395 3.01387
449 36 37 38 39 3 4.85568 -1.50692 2.84643 -6.19521 -2.67899 12.7253
450 38 39 40 41 3 4.85568 -1.50692 2.84643 -6.19521 -2.67899 12.7253
451 40 41 42 43 3 1.61159 -14.5043 4.39523 16.1577 -1.3395 3.01387
452 42 43 44 45 3 1.61159 -14.5043 4.39523 16.1577 -1.3395 3.01387
453 44 45 46 47 3 1.61159 -14.5043 4.39523 16.1577 -1.3395 3.01387
454 46 47 48 49 3 1.61159 -14.5043 4.39523 16.1577 -1.3395 3.01387
455 48 49 50 51 3 1.61159 -14.5043 4.39523 16.1577 -1.3395 3.01387
456 50 51 52 53 3 1.61159 -14.5043 4.39523 16.1577 -1.3395 3.01387
457 52 53 54 55 3 1.61159 -14.5043 4.39523 16.1577 -1.3395 3.01387
458 54 55 56 57 3 1.61159 -14.5043 4.39523 16.1577 -1.3395 3.01387
459 56 57 58 59 3 1.61159 -14.5043 4.39523 16.1577 -1.3395 3.01387
460 58 59 60 61 3 1.61159 -14.5043 4.39523 16.1577 -1.3395 3.01387
461 60 61 62 63 3 4.85568 -1.50692 2.84643 -6.19521 -2.67899 12.7253
462 62 63 64 65 3 4.85568 -1.50692 2.84643 -6.19521 -2.67899 12.7253
463 64 65 66 67 3 1.61159 -14.5043 4.39523 16.1577 -1.3395 3.01387
464 66 67 68 69 3 1.61159 -14.5043 4.39523 16.1577 -1.3395 3.01387
465 68 69 70 71 3 1.61159 -14.5043 4.39523 16.1577 -1.3395 3.01387
466 70 71 72 73 3 1.61159 -14.5043 4.39523 16.1577 -1.3395 3.01387
467 72 73 74 75 3 4.85568 -1.50692 2.84643 -6.19521 -2.67899 12.7253
468 74 75 76 77 3 4.85568 -1.50692 2.84643 -6.19521 -2.67899 12.7253
469 76 77 78 79 3 4.85568 -1.50692 2.84643 -6.19521 -2.67899 12.7253
470 78 79 80 81 3 4.85568 -1.50692 2.84643 -6.19521 -2.67899 12.7253
471 80 81 82 83 3 4.85568 -1.50692 2.84643 -6.19521 -2.67899 12.7253
472 82 83 84 85 3 4.85568 -1.50692 2.84643 -6.19521 -2.67899 12.7253
473 84 85 86 87 3 4.85568 -1.50692 2.84643 -6.19521 -2.67899 12.7253
474 86 87 88 89 3 4.85568 -1.50692 2.84643 -6.19521 -2.67899 12.7253
475 88 89 90 91 3 4.85568 -1.50692 2.84643 -6.19521 -2.67899 12.7253
476 90 91 92 93 3 4.85568 -1.50692 2.84643 -6.19521 -2.67899 12.7253
477 92 93 94 95 3 1.61159 -14.5043 4.39523 16.1577 -1.3395 3.01387
478 94 95 96 97 3 1.61159 -14.5043 4.39523 16.1577 -1.3395 3.01387
479 96 97 98 99 3 4.85568 -1.50692 2.84643 -6.19521 -2.67899 12.7253
480 98 99 100 101 3 4.85568 -1.50692 2.84643 -6.19521 -2.67899 12.7253
481 100 101 102 103 3 4.85568 -1.50692 2.84643 -6.19521 -2.67899 12.7253
482 102 103 104 105 3 4.85568 -1.50692 2.84643 -6.19521 -2.67899 12.7253
483 104 105 106 107 3 1.61159 -14.5043 4.39523 16.1577 -1.3395 3.01387
484 106 107 108 109 3 1.61159 -14.5043 4.39523 16.1577 -1.3395 3.01387
485 108 109 110 111 3 4.85568 -1.50692 2.84643 -6.19521 -2.67899 12.7253
486 110 111 112 113 3 4.85568 -1.50692 2.84643 -6.19521 -2.67899 12.7253
487 112 113 114 115 3 1.61159 -14.5043 4.39523 16.1577 -1.3395 3.01387
488 ; 26 alpha-cis and 30 trans of total 56 states
489 ; =====
490 ; =====
491 ; =====
492 ; =====
493 ; =====
494 ; =====
495 ; =====
496 ; =====
497 ; =====
498 ; =====
499 ; =====
500 ; =====
501 ; =====
502 ; =====
503 ; =====
504 ; =====
505 ; =====
506 ; =====
507 ; =====
508 ; =====
509 ; =====
510 ; =====
511 ; =====
512 ; =====
513 ; =====
514 ; =====
515 ; =====
516 ; =====
517 ; =====
518 ; =====
519 ; =====
520 ; =====
521 ; =====
522 ; =====
523 ; =====
524 ; =====
525 ; =====
526 ; =====
527 ; =====
528 ; =====
529 ; =====
530 ; =====
531 ; =====
532 ; =====
533 ; =====
534 ; =====
535 ; =====
536 ; =====
537 ; =====
538 ; =====
539 ; =====
540 ; =====
541 ; =====
542 ; =====
543 ; =====
544 ; =====
545 ; =====
546 ; =====
547 ; =====
548 ; =====
549 ; =====
550 ; =====
551 ; =====
552 ; =====
553 ; =====
554 ; =====
555 ; =====
556 ; =====
557 ; =====
558 ; =====
559 ; =====
560 ; =====
561 ; =====
562 ; =====
563 ; =====
564 ; =====
565 ; =====
566 ; =====
567 ; =====
568 ; =====
569 ; =====
570 ; =====
571 ; =====
572 ; =====
573 ; =====
574 ; =====
575 ; =====
576 ; =====
577 ; =====
578 ; =====
579 ; =====
580 ; =====
581 ; =====
582 ; =====
583 ; =====
584 ; =====
585 ; =====
586 ; =====
587 ; =====
588 ; =====
589 ; =====
590 ; =====
591 ; =====
592 ; =====
593 ; =====
594 ; =====
595 ; =====
596 ; =====
597 ; =====
598 ; =====
599 ; =====
600 ; =====
601 ; =====
602 ; =====
603 ; =====
604 ; =====
605 ; =====
606 ; =====
607 ; =====
608 ; =====
609 ; =====
610 ; =====
611 ; =====
612 ; =====
613 ; =====
614 ; =====
615 ; =====
616 ; =====
617 ; =====
618 ; =====
619 ; =====
620 ; =====
621 ; =====
622 ; =====
623 ; =====
624 ; =====
625 ; =====
626 ; =====
627 ; =====
628 ; =====
629 ; =====
630 ; =====
631 ; =====
632 ; =====
633 ; =====
634 ; =====
635 ; =====
636 ; =====
637 ; =====
638 ; =====
639 ; =====
640 ; =====
641 ; =====
642 ; =====
643 ; =====
644 ; =====
645 ; =====
646 ; =====
647 ; =====
648 ; =====
649 ; =====
650 ; =====
651 ; =====
652 ; =====
653 ; =====
654 ; =====
655 ; =====
656 ; =====
657 ; =====
658 ; =====
659 ; =====
660 ; =====
661 ; =====
662 ; =====
663 ; =====
664 ; =====
665 ; =====
666 ; =====
667 ; =====
668 ; =====
669 ; =====
670 ; =====
671 ; =====
672 ; =====
673 ; =====
674 ; =====
675 ; =====
676 ; =====
677 ; =====
678 ; =====
679 ; =====
680 ; =====
681 ; =====
682 ; =====
683 ; =====
684 ; =====
685 ; =====
686 ; =====
687 ; =====
688 ; =====
689 ; =====
690 ; =====
691 ; =====
692 ; =====
693 ; =====
694 ; =====
695 ; =====
696 ; =====
697 ; =====
698 ; =====
699 ; =====
700 ; =====
701 ; =====
702 ; =====
703 ; =====
704 ; =====
705 ; =====
706 ; =====
707 ; =====
708 ; =====
709 ; =====
710 ; =====
711 ; =====
712 ; =====
713 ; =====
714 ; =====
715 ; =====
716 ; =====
717 ; =====
718 ; =====
719 ; =====
720 ; =====
721 ; =====
722 ; =====
723 ; =====
724 ; =====
725 ; =====
726 ; =====
727 ; =====
728 ; =====
729 ; =====
730 ; =====
731 ; =====
732 ; =====
733 ; =====
734 ; =====
735 ; =====
736 ; =====
737 ; =====
738 ; =====
739 ; =====
740 ; =====
741 ; =====
742 ; =====
743 ; =====
744 ; =====
745 ; =====
746 ; =====
747 ; =====
748 ; =====
749 ; =====
750 ; =====
751 ; =====
752 ; =====
753 ; =====
754 ; =====
755 ; =====
756 ; =====
757 ; =====
758 ; =====
759 ; =====
760 ; =====
761 ; =====
762 ; =====
763 ; =====
764 ; =====
765 ; =====
766 ; =====
767 ; =====
768 ; =====
769 ; =====
770 ; =====
771 ; =====
772 ; =====
773 ; =====
774 ; =====
775 ; =====
776 ; =====
777 ; =====
778 ; =====
779 ; =====
780 ; =====
781 ; =====
782 ; =====
783 ; =====
784 ; =====
785 ; =====
786 ; =====
787 ; =====
788 ; =====
789 ; =====
790 ; =====
791 ; =====
792 ; =====
793 ; =====
794 ; =====
795 ; =====
796 ; =====
797 ; =====
798 ; =====
799 ; =====
800 ; =====
801 ; =====
802 ; =====
803 ; =====
804 ; =====
805 ; =====
806 ; =====
807 ; =====
808 ; =====
809 ; =====
810 ; =====
811 ; =====
812 ; =====
813 ; =====
814 ; =====
815 ; =====
816 ; =====
817 ; =====
818 ; =====
819 ; =====
820 ; =====
821 ; =====
822 ; =====
823 ; =====
824 ; =====
825 ; =====
826 ; =====
827 ; =====
828 ; =====
829 ; =====
830 ; =====
831 ; =====
832 ; =====
833 ; =====
834 ; =====
835 ; =====
836 ; =====
837 ; =====
838 ; =====
839 ; =====
840 ; =====
841 ; =====
842 ; =====
843 ; =====
844 ; =====
845 ; =====
846 ; =====
847 ; =====
848 ; =====
849 ; =====
850 ; =====
851 ; =====
852 ; =====
853 ; =====
854 ; =====
855 ; =====
856 ; =====
857 ; =====
858 ; =====
859 ; =====
860 ; =====
861 ; =====
862 ; =====
863 ; =====
864 ; =====
865 ; =====
866 ; =====
867 ; =====
868 ; =====
869 ; =====
870 ; =====
871 ; =====
872 ; =====
873 ; =====
874 ; =====
875 ; =====
876 ; =====
877 ; =====
878 ; =====
879 ; =====
880 ; =====
881 ; =====
882 ; =====
883 ; =====
884 ; =====
885 ; =====
886 ; =====
887 ; =====
888 ; =====
889 ; =====
890 ; =====
891 ; =====
892 ; =====
893 ; =====
894 ; =====
895 ; =====
896 ; =====
897 ; =====
898 ; =====
899 ; =====
900 ; =====
901 ; =====
902 ; =====
903 ; =====
904 ; =====
905 ; =====
906 ; =====
907 ; =====
908 ; =====
909 ; =====
910 ; =====
911 ; =====
912 ; =====
913 ; =====
914 ; =====
915 ; =====
916 ; =====
917 ; =====
918 ; =====
919 ; =====
920 ; =====
921 ; =====
922 ; =====
923 ; =====
924 ; =====
925 ; =====
926 ; =====
927 ; =====
928 ; =====
929 ; =====
930 ; =====
931 ; =====
932 ; =====
933 ; =====
934 ; =====
935 ; =====
936 ; =====
937 ; =====
938 ; =====
939 ; =====
940 ; =====
941 ; =====
942 ; =====
943 ; =====
944 ; =====
945 ; =====
946 ; =====
947 ; =====
948 ; =====
949 ; =====
950 ; =====
951 ; =====
952 ; =====
953 ; =====
954 ; =====
955 ; =====
956 ; =====
957 ; =====
958 ; =====
959 ; =====
960 ; =====
961 ; =====
962 ; =====
963 ; =====
964 ; =====
965 ; =====
966 ; =====
967 ; =====
968 ; =====
969 ; =====
970 ; =====
971 ; =====
972 ; =====
973 ; =====
974 ; =====
975 ; =====
976 ; =====
977 ; =====
978 ; =====
979 ; =====
980 ; =====
981 ; =====
982 ; =====
983 ; =====
984 ; =====
985 ; =====
986 ; =====
987 ; =====
988 ; =====
989 ; =====
990 ; =====
991 ; =====
992 ; =====
993 ; =====
994 ; =====
995 ; =====
996 ; =====
997 ; =====
998 ; =====
999 ; =====
1000 ; =====

```



```

487 ; Beta-torsion potential (nr=5 from Table 2.4 of Krushev)
488 ; PROPER DIHEDRALS RYCKAERT-BELLEMANS FUNCTION
489 ; i j k l type(3=RB-DIH.) CO,C1,C2,C3,C4,C5 (in kJ/mol)
490 3 4 5 6 3 -13.6461 20.6785 1.42321 -23.3575 1.17206 -8.37189
491 7 8 9 10 3 -13.6461 20.6785 1.42321 -23.3575 1.17206 -8.37189
492 11 12 13 14 3 -13.6461 20.6785 1.42321 -23.3575 1.17206 -8.37189
493 15 16 17 18 3 -13.6461 20.6785 1.42321 -23.3575 1.17206 -8.37189
494 19 20 21 22 3 -13.6461 20.6785 1.42321 -23.3575 1.17206 -8.37189
495 23 24 25 26 3 -13.6461 20.6785 1.42321 -23.3575 1.17206 -8.37189
496 27 28 29 30 3 -13.6461 20.6785 1.42321 -23.3575 1.17206 -8.37189
497 31 32 33 34 3 -13.6461 20.6785 1.42321 -23.3575 1.17206 -8.37189
498 35 36 37 38 3 -13.6461 20.6785 1.42321 -23.3575 1.17206 -8.37189
499 39 40 41 42 3 -13.6461 20.6785 1.42321 -23.3575 1.17206 -8.37189
500 43 44 45 46 3 -13.6461 20.6785 1.42321 -23.3575 1.17206 -8.37189
501 47 48 49 50 3 -13.6461 20.6785 1.42321 -23.3575 1.17206 -8.37189
502 51 52 53 54 3 -13.6461 20.6785 1.42321 -23.3575 1.17206 -8.37189
503 55 56 57 58 3 -13.6461 20.6785 1.42321 -23.3575 1.17206 -8.37189
504 59 60 61 62 3 -13.6461 20.6785 1.42321 -23.3575 1.17206 -8.37189
505 63 64 65 66 3 -13.6461 20.6785 1.42321 -23.3575 1.17206 -8.37189
506 67 68 69 70 3 -13.6461 20.6785 1.42321 -23.3575 1.17206 -8.37189
507 71 72 73 74 3 -13.6461 20.6785 1.42321 -23.3575 1.17206 -8.37189
508 75 76 77 78 3 -13.6461 20.6785 1.42321 -23.3575 1.17206 -8.37189
509 79 80 81 82 3 -13.6461 20.6785 1.42321 -23.3575 1.17206 -8.37189
510 83 84 85 86 3 -13.6461 20.6785 1.42321 -23.3575 1.17206 -8.37189
511 87 88 89 90 3 -13.6461 20.6785 1.42321 -23.3575 1.17206 -8.37189
512 91 92 93 94 3 -13.6461 20.6785 1.42321 -23.3575 1.17206 -8.37189
513 95 96 97 98 3 -13.6461 20.6785 1.42321 -23.3575 1.17206 -8.37189
514 99 100 101 102 3 -13.6461 20.6785 1.42321 -23.3575 1.17206 -8.37189
515 103 104 105 106 3 -13.6461 20.6785 1.42321 -23.3575 1.17206 -8.37189
516 107 108 109 110 3 -13.6461 20.6785 1.42321 -23.3575 1.17206 -8.37189
517 111 112 113 114 3 -13.6461 20.6785 1.42321 -23.3575 1.17206 -8.37189
518 ; =====
519 ; =====
520 ; =====
521 ; =====
522 ; =====
523 ; DOUBLE BOND TORSION: based on w.Paul potential
524 ; with separated cis and trans state
525 ; PROPER DIHEDRALS RYCKAERT-BELLEMANS FUNCTION
526 ;
527 ; i j k l type(3=RB-DIH.) CO,C1,C2,C3,C4,C5 (in kJ/mol)
528 ; =====
529 ; =====
530 ; =====
531 ; =====
532 ; =====
533 ; =====
534 ; =====
535 ; =====
536 ; =====
537 ; =====
538 ; =====
539 ; =====
540 ; =====
541 ; =====
542 ; =====
543 ; =====
544 ; =====
545 ; =====
546 ; =====
547 ; =====
548 ; =====
549 ; =====
550 ; =====
551 ; =====
552 ; =====
553 ; =====
554 ; =====
555 ; =====
556 ; =====
557 ; =====
558 ; =====
559 ; =====
560 ; =====
561 ; =====
562 ; =====
563 ; =====
564 ; =====
565 ; =====
566 ; =====
567 ; =====
568 ; =====
528 ; due to psi=phi-180 definition of gromacs
529 ; we invert sign (SGN) of odd C1 (C1,C3,C5)
530 1 2 3 4 3 100.462 -22.2441 0.420646 -115.263 -0.673409 37.2977
531 5 6 7 8 3 100.462 -22.2441 0.420646 -115.263 -0.673409 37.2977
532 9 10 11 12 3 100.462 -22.2441 0.420646 115.263 -0.673409 -37.2977
533 13 14 15 16 3 100.462 -22.2441 0.420646 -115.263 -0.673409 -37.2977
534 17 18 19 20 3 100.462 -22.2441 0.420646 115.263 -0.673409 -37.2977
535 21 22 23 24 3 100.462 -22.2441 0.420646 115.263 -0.673409 -37.2977
536 25 26 27 28 3 100.462 -22.2441 0.420646 -115.263 -0.673409 37.2977
537 29 30 31 32 3 100.462 -22.2441 0.420646 -115.263 -0.673409 37.2977
538 33 34 35 36 3 100.462 -22.2441 0.420646 -115.263 -0.673409 37.2977
539 37 38 39 40 3 100.462 -22.2441 0.420646 115.263 -0.673409 -37.2977
540 41 42 43 44 3 100.462 -22.2441 0.420646 -115.263 -0.673409 37.2977
541 45 46 47 48 3 100.462 -22.2441 0.420646 -115.263 -0.673409 37.2977
542 49 50 51 52 3 100.462 -22.2441 0.420646 -115.263 -0.673409 37.2977
543 53 54 55 56 3 100.462 -22.2441 0.420646 -115.263 -0.673409 37.2977
544 57 58 59 60 3 100.462 -22.2441 0.420646 -115.263 -0.673409 37.2977
545 61 62 63 64 3 100.462 -22.2441 0.420646 115.263 -0.673409 -37.2977
546 65 66 67 68 3 100.462 -22.2441 0.420646 -115.263 -0.673409 37.2977
547 69 70 71 72 3 100.462 -22.2441 0.420646 -115.263 -0.673409 37.2977
548 73 74 75 76 3 100.462 -22.2441 0.420646 115.263 -0.673409 -37.2977
549 77 78 79 80 3 100.462 -22.2441 0.420646 115.263 -0.673409 -37.2977
550 81 82 83 84 3 100.462 -22.2441 0.420646 115.263 -0.673409 -37.2977
551 85 86 87 88 3 100.462 -22.2441 0.420646 115.263 -0.673409 -37.2977
552 89 90 91 92 3 100.462 -22.2441 0.420646 115.263 -0.673409 -37.2977
553 93 94 95 96 3 100.462 -22.2441 0.420646 -115.263 -0.673409 37.2977
554 97 98 99 100 3 100.462 -22.2441 0.420646 115.263 -0.673409 -37.2977
555 101 102 103 104 3 100.462 -22.2441 0.420646 115.263 -0.673409 -37.2977
556 105 106 107 108 3 100.462 -22.2441 0.420646 -115.263 -0.673409 37.2977
557 109 110 111 112 3 100.462 -22.2441 0.420646 115.263 -0.673409 -37.2977
558 113 114 115 116 3 100.462 -22.2441 0.420646 -115.263 -0.673409 37.2977
559 ; 13 alpha-cis and 16 trans of total 29 states
560 ; =====
561 ; =====
562 ; =====
563 ; =====
564 ; =====
565 ; =====
566 [ molecules ]
567 ; Compound #mols
568 P1 1

```


Appendix B

Supplementary Figures - PBD inside an alumina nanopore

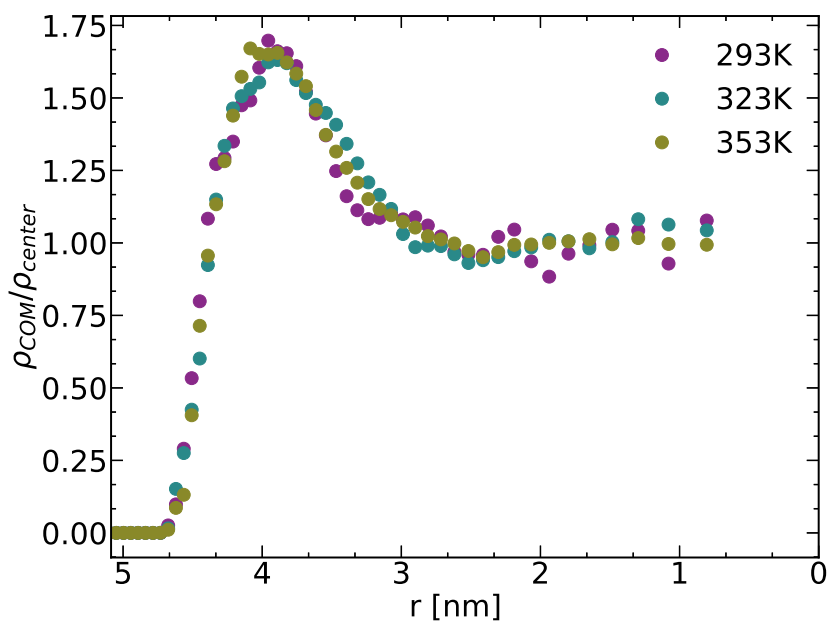


Figure B.1: The center of mass (COM) density along the radial direction for a PBD melt inside an alumina nanopore. The volume of the bins is kept constant with an initial bin size of 0.1 nm and the figure shows the data for $T = 293, 323$ and 353 K.

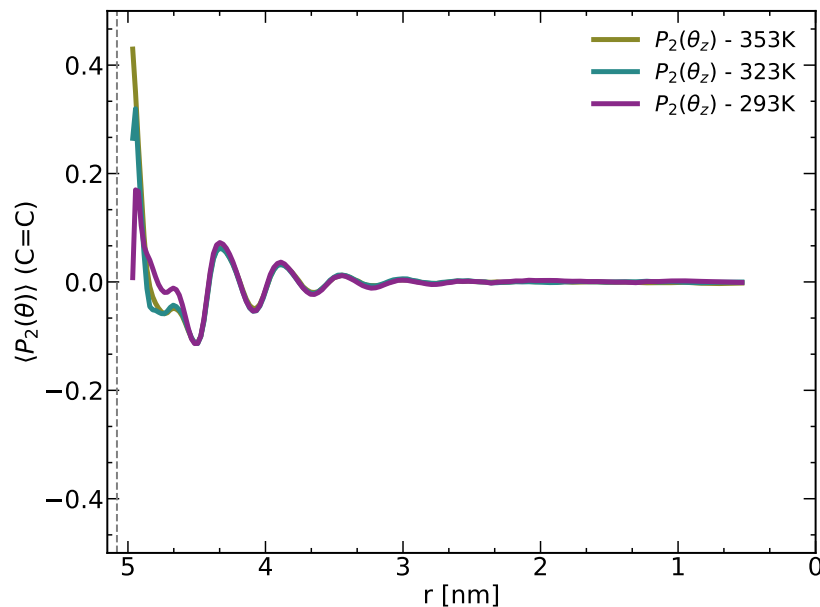


Figure B.2: The second Legendre polynomial of the angle between the double bonds and the axial direction (\hat{e}_z) of the nanopore for all three temperatures $T = 293, 323$ and 353 K. The grey dashed line is the radial position of the pore wall.

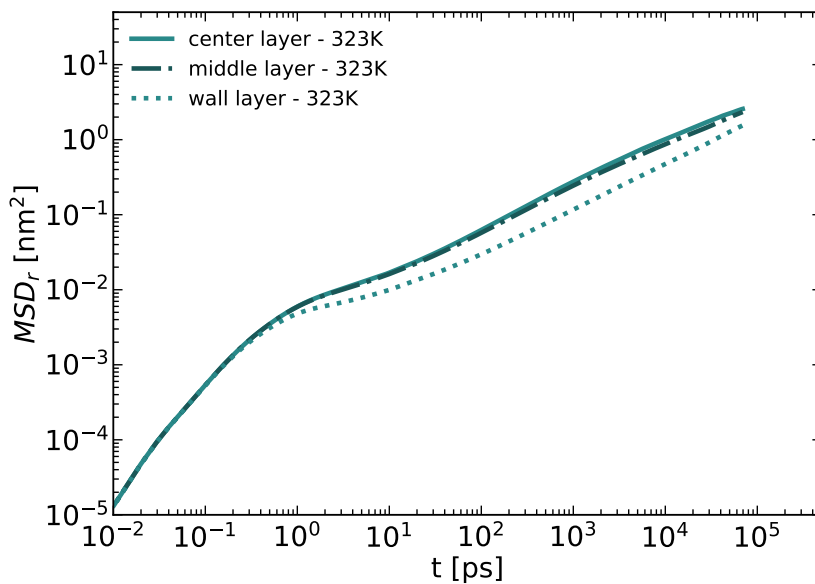


Figure B.3: The monomer MSD along the radial direction at $T = 323$ K for all three bins across the nanopore.

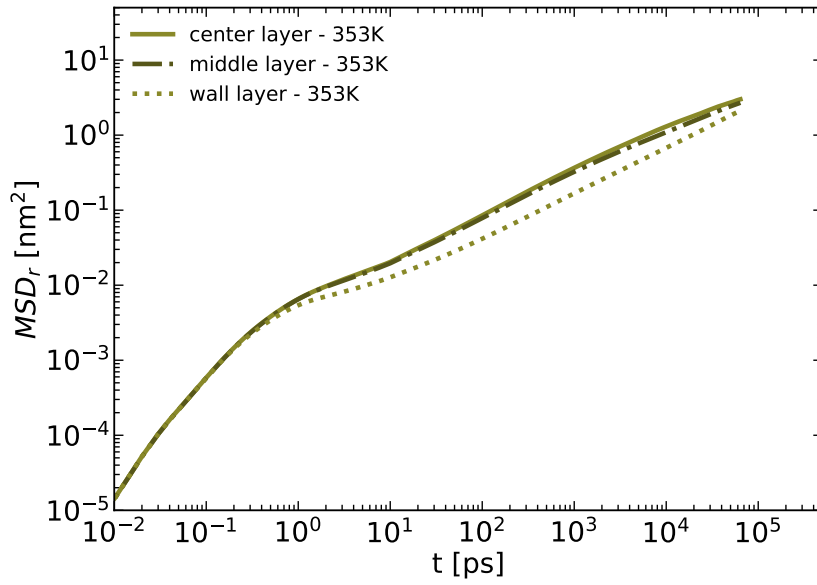


Figure B.4: The monomer MSD along the radial direction at $T = 353$ K for all three bins across the nanopore.

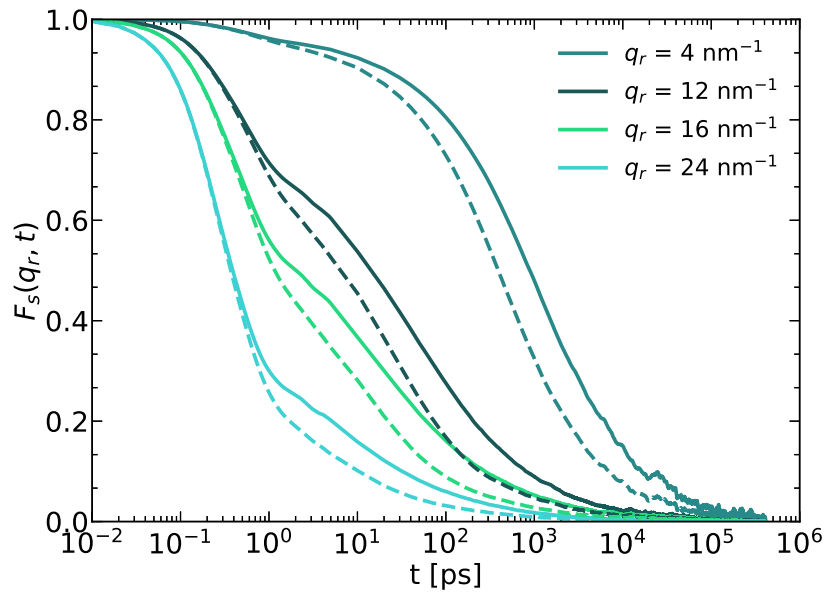


Figure B.5: The INSF at $T = 323$ K for the monomers in the wall layer (solid) and averaged over all monomers (dashed) for different values of the momentum transfer q_r .

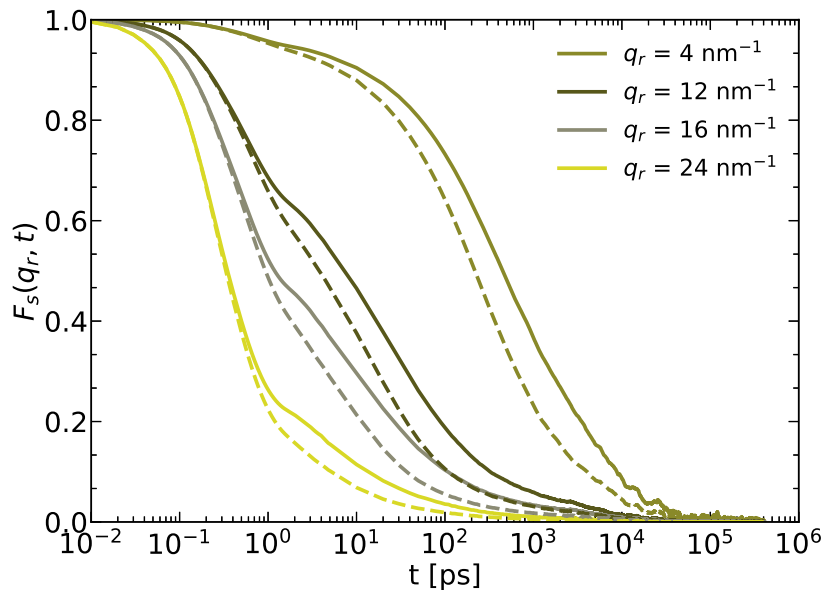


Figure B.6: The INSF at $T = 353$ K for the monomers in the wall layer (solid) and averaged over all monomers (dashed) for different values of the momentum transfer q_r .

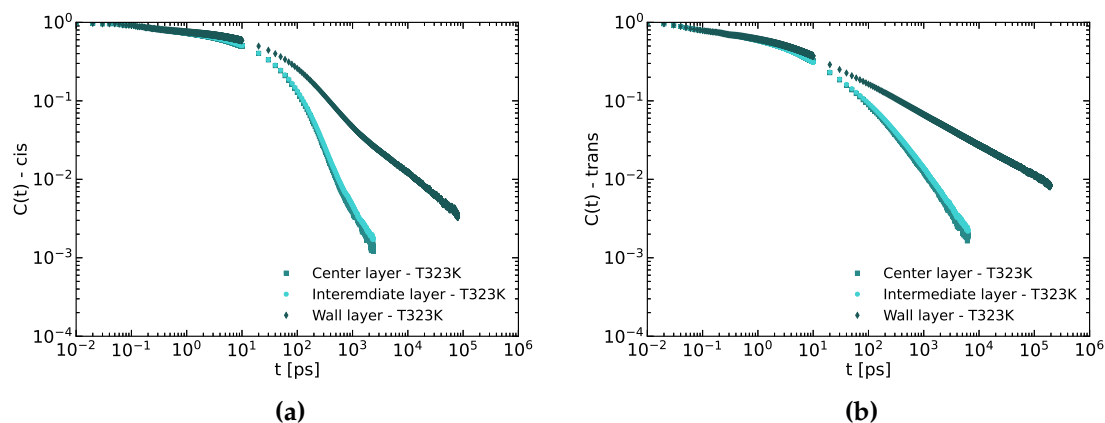


Figure B.7: The orientational autocorrelation function of CH *cis* (a) and *trans* (b) groups at $T = 323$ K for the three layers in the melt.

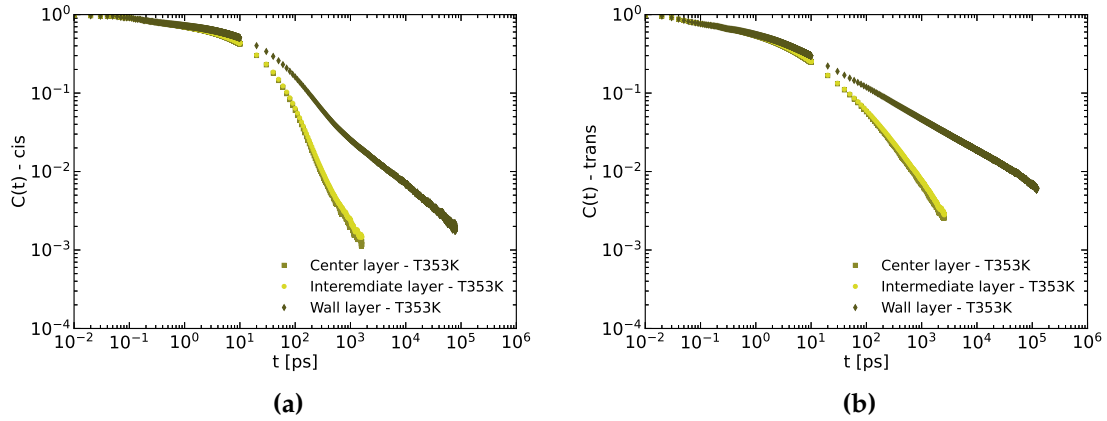


Figure B.8: The orientational autocorrelation function of CH *cis* (a) and *trans* (b) groups at $T = 353$ K for the three layers in the melt.

Table B.1: The superposition of two stretched exponentials fitting parameters for the orientational autocorrelation function of the C–H bonds for the nanopore system. The data includes the fitting parameters for all three temperatures and or both *cis* and *trans* conformers.

Temp [K]	value	cis			trans		
		L1 ^a	L2 ^b	L3 ^c	L1	L2	L3
293	A	0.344	0.357	0.339	0.451	0.787	0.767
	τ_1	2.79	2.43	51.70	8.87	13.17	15.32
	β_1	0.230	0.219	0.188	0.236	0.332	0.297
	τ_2	81.7	83.9	131.87	18.85	21.01	621.01
	β_2	0.663	0.644	0.476	0.412	0.239	0.198
323	A	0.195	0.282	0.275	0.862	0.972	0.828
	τ_1	0.35	0.83	11.89	5.95	5.87	8.42
	β_1	0.181	0.204	0.169	0.341	0.316	0.292
	τ_2	28.27	35.51	57.76	21.92	491	230.87
	β_2	0.547	0.604	0.484	0.259	0.369	0.165
353	A	0.297	0.266	0.280	0.792	0.892	0.813
	τ_1	0.63	0.39	2.91	3.36	3.38	4.09
	β_1	0.217	0.199	0.160	0.361	0.336	0.284
	τ_2	20.68	20.82	32.67	8.30	21.69	53.25
	β_2	0.636	0.616	0.519	0.259	0.271	0.159

^a L1 corresponds to the layer at the center of the pore.

^b L2 corresponds to the intermediate layer.

^c L3 corresponds to the layer closest to the pore walls.

Appendix C

Supplementary Figures - PBD surrounding an alumina nanorod

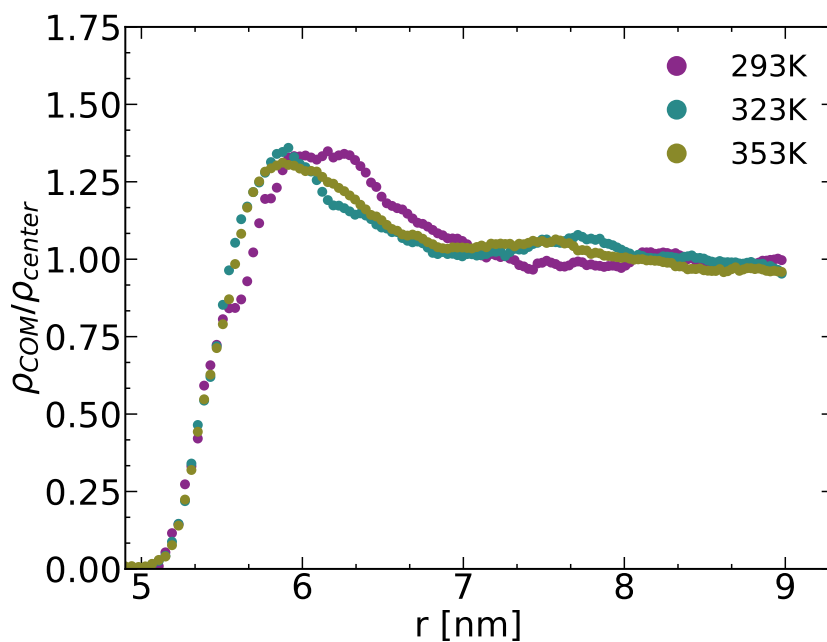


Figure C.1: The center of mass (COM) density along the radial direction for a PBD melt around an alumina nano-rod. The volume of the bins is kept constant with an initial bin size of 0.5 \AA and the figure shows the data for $T = 293, 323$ and 353 K .

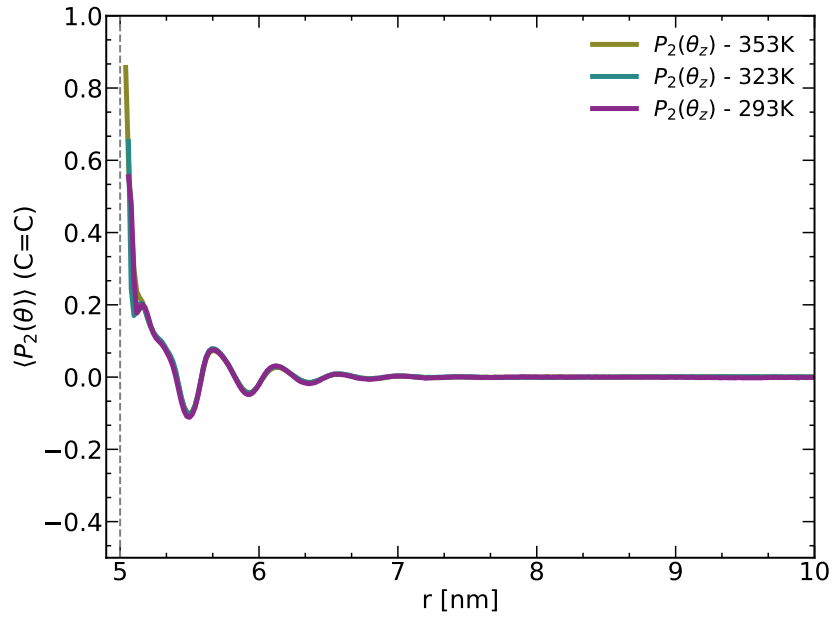


Figure C.2: The second Legendre polynomial of the angle between the double bonds and the axial direction (\hat{e}_z) for all three temperatures $T = 293, 323$ and 353 K. The grey dashed line is the radial position of the nano-rod wall.

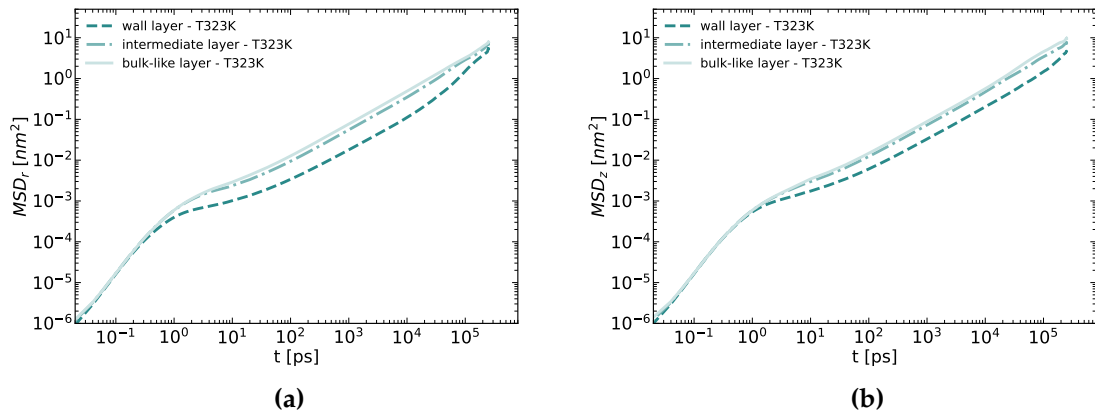


Figure C.3: Center of mass (COM) mean squared displacement in the radial **(a)** and axial **(b)** directions for the three different layers at $T = 323$ K.

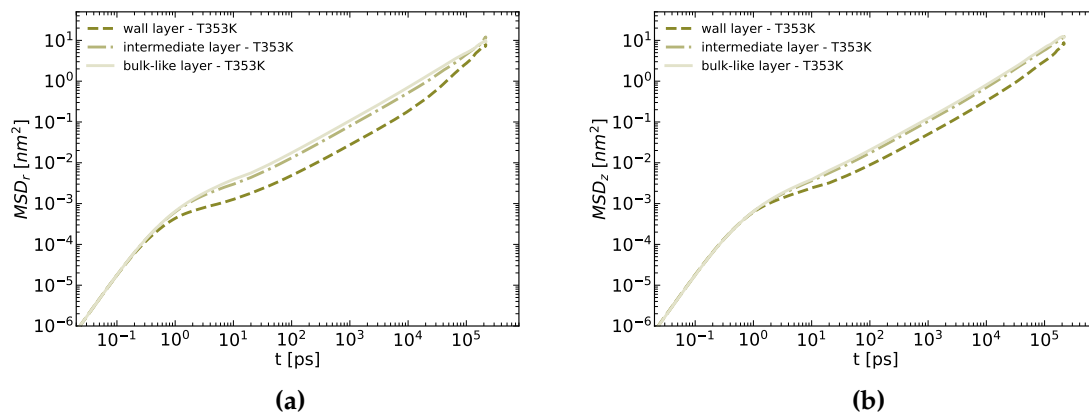


Figure C.4: Center of mass (COM) mean squared displacement in the radial (a) and axial (b) directions for the three different layers at $T = 353 \text{ K}$.

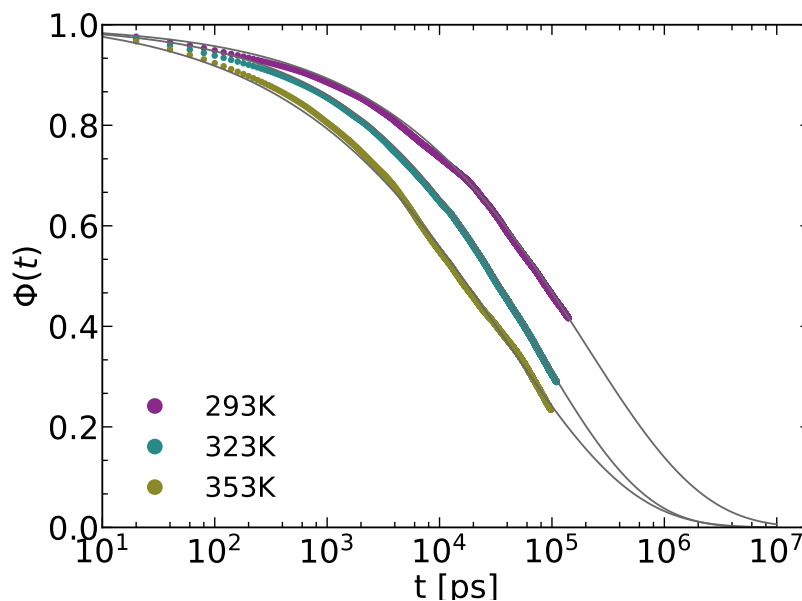


Figure C.5: The adsorption autocorrelation function $\Phi(t)$ for the monomers adsorbed to the rod wall at all three temperatures. The solid grey lines are the fits to the stretched exponential function.

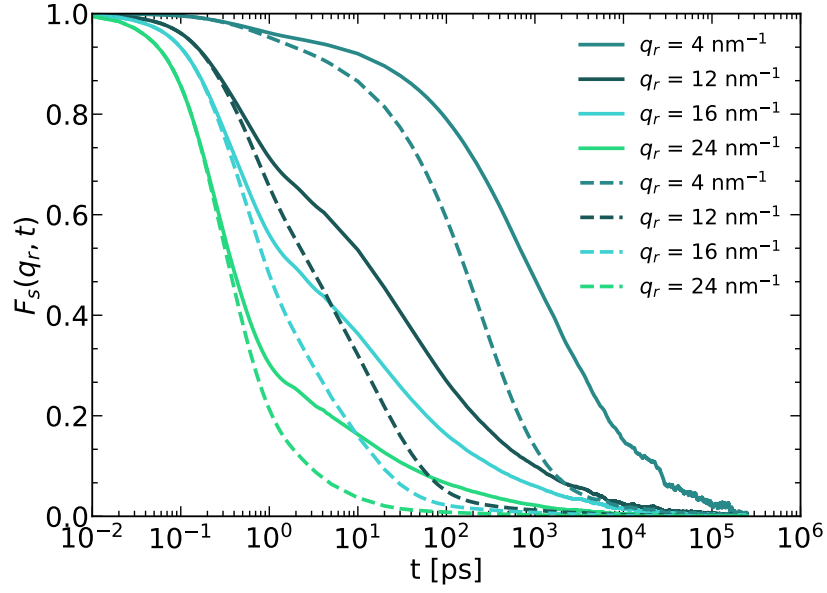


Figure C.6: The INSF at $T = 323$ K for the monomers in the wall layer (solid) and averaged over all monomers (dashed) for different values of the momentum transfer \mathbf{q}_r .

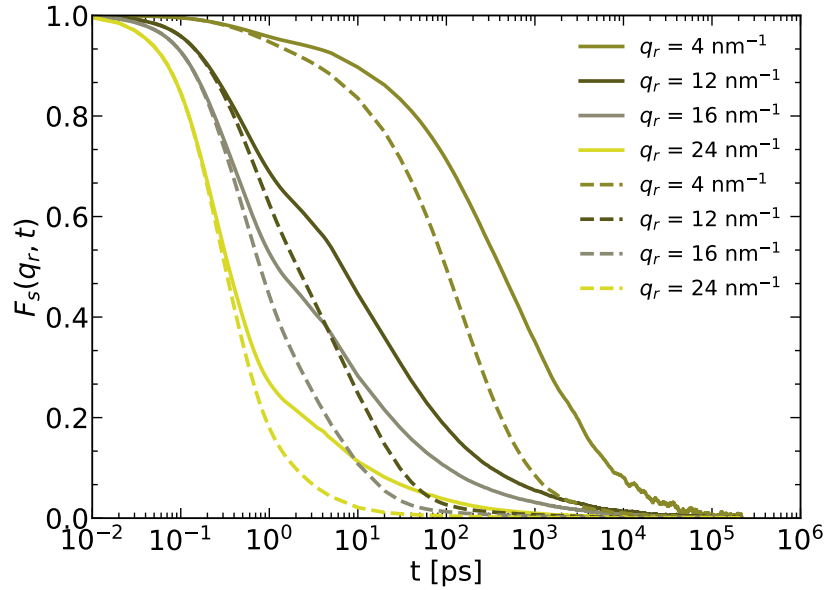


Figure C.7: The INSF at $T = 353$ K for the monomers in the wall layer (solid) and averaged over all monomers (dashed) for different values of the momentum transfer \mathbf{q}_r .

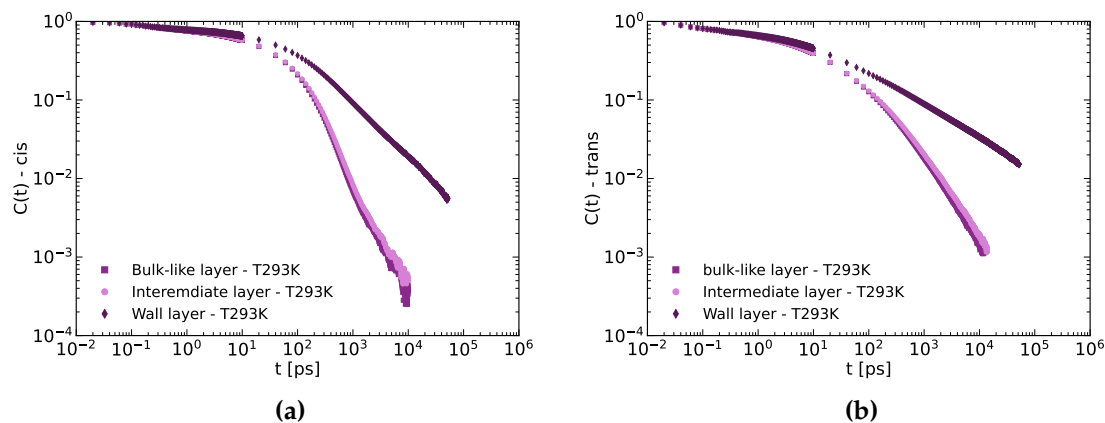


Figure C.8: The orientational autocorrelation function of CH *cis* (a) and *trans* (b) groups at $T = 293$ K for the three layers in the melt.

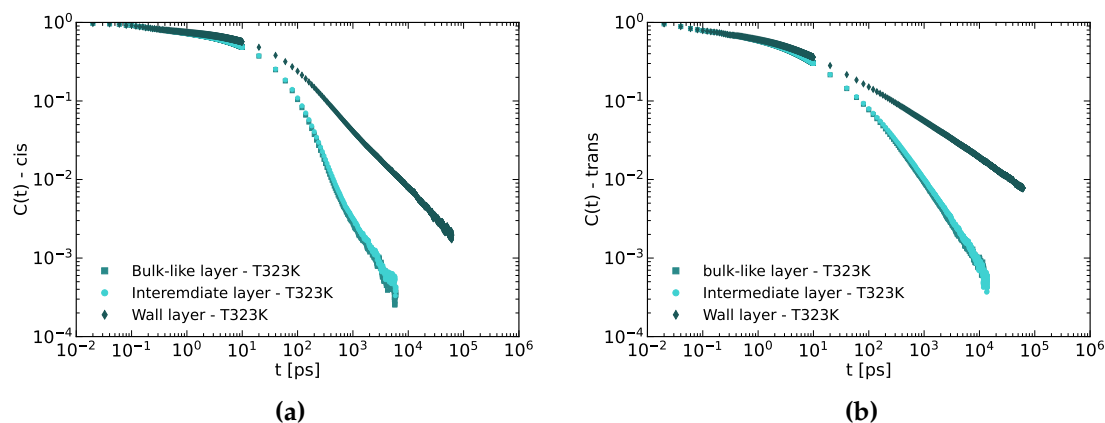


Figure C.9: The orientational autocorrelation function of CH *cis* (a) and *trans* (b) groups at $T = 323$ K for the three layers in the melt.

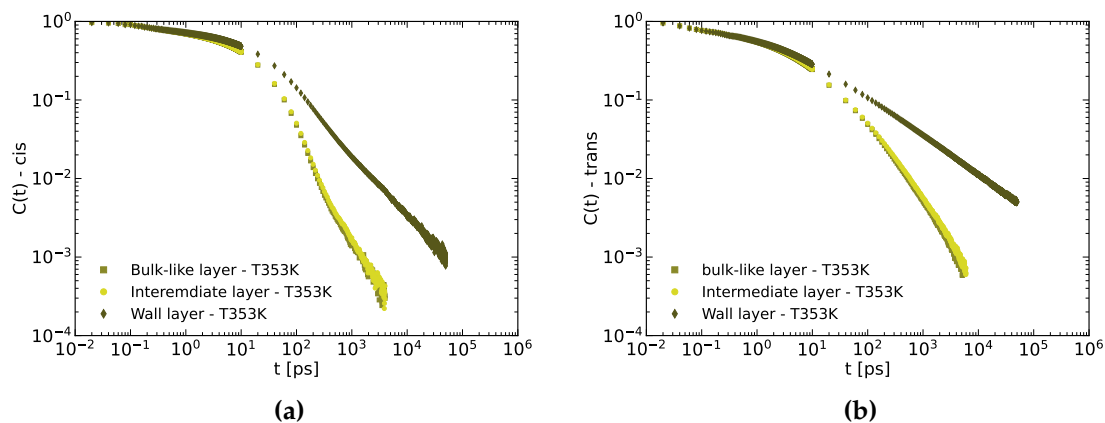


Figure C.10: The orientational autocorrelation function of CH *cis* (a) and *trans* (b) groups at $T = 353$ K for the three layers in the melt.

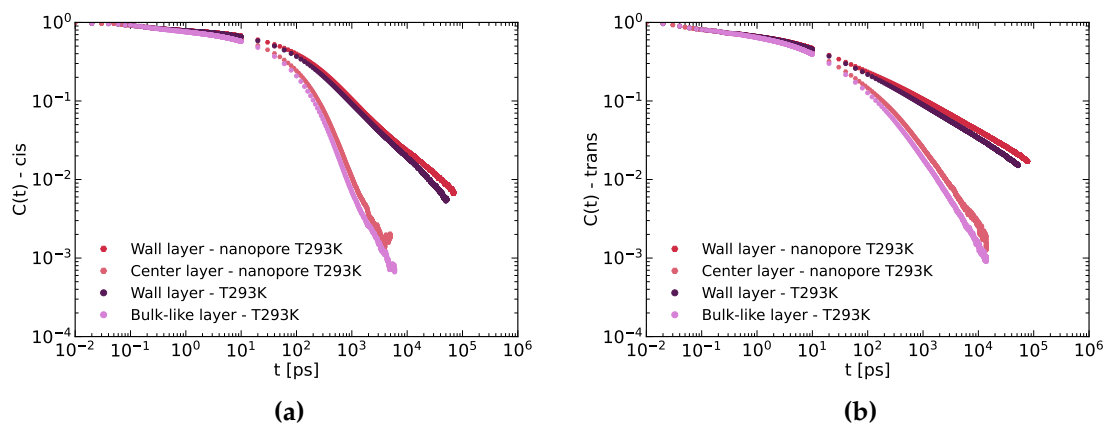


Figure C.11: The correlation function for *cis* and *trans* at $T = 293$ K for the wall and furthest layer from the wall for both the nanopore and nanorod systems.

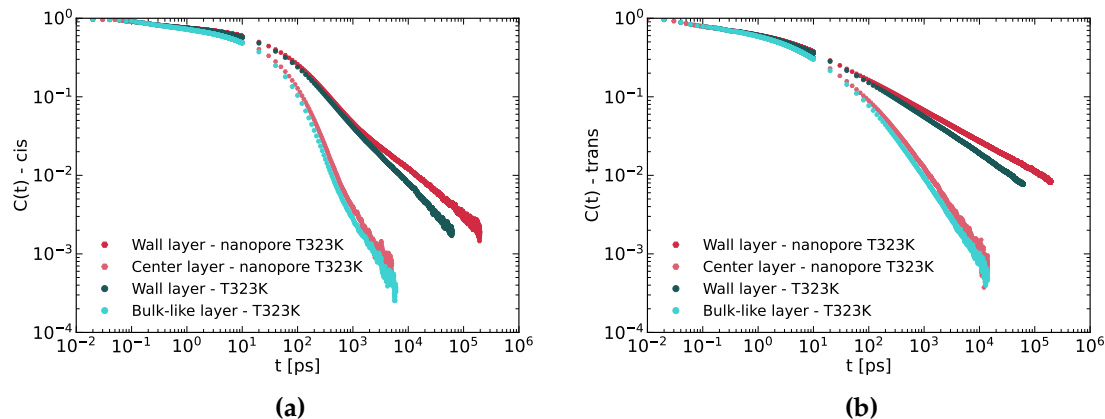


Figure C.12: The correlation function for *cis* and *trans* at $T = 323$ K for the wall and furthest layer from the wall for both the nanopore and nanorod systems.

Table C.1: The superposition of two stretched exponentials fitting parameters for the orientational autocorrelation function of the C–H bonds for the nanorod system. The data includes the fitting parameters for all three temperatures and for both *cis* and *trans* conformers.

Temp [K]	value	cis			trans		
		L1 ^a	L2 ^b	L3 ^c	L1	L2	L3
293	A	0.285	0.149	0.270	0.961	0.984	0.668
	τ_1	1.29	4.75	53.01	11.0	11.57	21.48
	β_1	0.213	0.227	0.194	0.335	0.332	0.307
	τ_2	57.67	51.67	94.33	301.27	2106	53.36
	β_2	0.607	0.565	0.402	0.344	0.497	0.162
323	A	0.273	0.217	0.846	0.866	0.888	0.799
	τ_1	0.58	0.56	35.27	5.26	5.28	7.422
	β_1	0.206	0.198	0.414	0.364	0.345	0.308
	τ_2	29.61	26.28	85.44	23.17	26.83	85.59
	β_2	0.618	0.569	0.227	0.273	0.267	0.179
353	A	0.265	0.257	0.231	0.846	0.927	0.799
	τ_1	0.364	0.437	2.67	3.35	3.38	4.24
	β_1	0.207	0.209	0.173	0.386	0.359	0.286
	τ_2	18.11	17.67	27.56	14.42	49.49	14.26
	β_2	0.633	0.616	0.483	0.286	0.322	0.161

^a L1 corresponds to the farthest away from the nanorod.

^b L2 corresponds to the intermediate layer.

^c L3 corresponds to the layer at the interface.

Bibliography

- [1] K. Binder, J. Horbach, R. Vink, and A. De Virgiliis, "Confinement effects on phase behavior of soft matter systems," *Soft Matter*, vol. 4, pp. 1555–1568, 2008.
- [2] A. Flores, F. Ania, and F. J. Baltá-Calleja, "From the glassy state to ordered polymer structures: A microhardness study," *Polymer*, vol. 50, pp. 729–746, 1 2009.
- [3] C. B. Roth, "Polymers under nanoconfinement: where are we now in understanding local property changes?," *Chem. Soc. Rev.*, vol. 50, pp. 8050–8066, 2021.
- [4] B. D. Vogt, "Mechanical and viscoelastic properties of confined amorphous polymers," *Journal of Polymer Science, Part B: Polymer Physics*, vol. 56, pp. 9–30, 1 2018.
- [5] A. Milchev, "Single-polymer dynamics under constraints: scaling theory and computer experiment," *Journal of Physics: Condensed Matter*, vol. 23, p. 103101, 2 2011.
- [6] S. Napolitano, E. Glynos, and N. B. Tito, "Glass transition of polymers in bulk, confined geometries, and near interfaces," *Reports on Progress in Physics*, vol. 80, p. 036602, 1 2017.
- [7] M.-C. Ma and Y.-L. Guo, "Physical properties of polymers under soft and hard nanoconfinement: A review," *Chinese J. Polym. Sci.*, vol. 2020, pp. 565–578.
- [8] E. A. Rössler, S. Stapf, and N. Fatkullin, "Recent NMR investigations on molecular dynamics of polymer melts in bulk and in confinement," *Current Opinion in Colloid and Interface Science*, vol. 18, pp. 173–182, 2013.

- [9] Q. Jiang and M. D. Ward, "Crystallization under nanoscale confinement," *Chem. Soc. Rev.*, vol. 43, p. 2066, 2066.
- [10] K. Chrissopoulou and S. H. Anastasiadis, "Effects of nanoscopic-confinement on polymer dynamics," *Soft Matter*, vol. 11, pp. 3746–3766, 2015.
- [11] B.-Y. Ha and Y. Jung, "Polymers under confinement: single polymers, how they interact, and as model chromosomes," *Soft Matter*, vol. 11, pp. 2333–2352, 2015.
- [12] S. Alexandris, G. Sakellariou, M. Steinhart, and G. Floudas, "Dynamics of unentangled cis-1,4-polyisoprene confined to nanoporous alumina," *Macromolecules*, vol. 47, no. 12, pp. 3895–3900, 2014.
- [13] M. Krutyeva, J. Martin, A. Arbe, J. Colmenero, C. Mijangos, G. J. Schneider, T. Unruh, Y. Su, and D. Richter, "Neutron scattering study of the dynamics of a polymer melt under nanoscopic confinement," *The Journal of Chemical Physics*, vol. 131, no. 17, p. 174901, 2009.
- [14] D. Hudzinsky, A. V. Lyulin, A. R. C. Baljon, N. K. Balabaev, and M. A. J. Michels, "Effects of strong confinement on the glass-transition temperature in simulated atactic polystyrene films," *Macromolecules*, vol. 44, no. 7, pp. 2299–2310, 2011.
- [15] J. A. Forrest, K. Dalnoki-Veress, J. R. Stevens, and J. R. Dutcher, "Effect of free surfaces on the glass transition temperature of thin polymer films," *Phys. Rev. Lett.*, vol. 77, pp. 2002–2005, Sep 1996.
- [16] D. Richter and M. Kruteva, "Polymer dynamics under confinement," *Soft Matter*, vol. 15, pp. 7316–7349, 2019.
- [17] R. Horstmann, L. Hecht, S. Kloth, and M. Vogel, "Structural and dynamical properties of liquids in confinements: A review of molecular dynamics simulation studies," *Langmuir*, vol. 38, no. 21, pp. 6506–6522, 2022. PMID: 35580166.
- [18] J. Kirk and P. Ilg, "Chain dynamics in polymer melts at flat surfaces," *Macromolecules*, vol. 50, pp. 3703–3718, May 2017.

- [19] B. Frank, A. P. Gast, T. P. Russell, H. R. Brown, and C. Hawker, "Polymer mobility in thin films," *Macromolecules*, vol. 29, no. 20, pp. 6531–6534, 1996.
- [20] I. Bitsanis and G. Hadziioannou, "Molecular dynamics simulations of the structure and dynamics of confined polymer melts," *The Journal of Chemical Physics*, vol. 92, no. 6, pp. 3827–3847, 1990.
- [21] J. Sarabadani, A. Milchev, and T. A. Vilgis, "Structure and dynamics of polymer melt confined between two solid surfaces: A molecular dynamics study," *The Journal of Chemical Physics*, vol. 141, no. 4, p. 044907, 2014.
- [22] L. Yelash, P. Virnau, K. Binder, and W. Paul, "Three-step decay of time correlations at polymer-solid interfaces," *EPL*, vol. 98, p. 28006, 2012.
- [23] M. Solar and W. Paul, "Chain relaxation in thin polymer films: turning a dielectric type-B polymer into a type-A one," *Soft Matter*, vol. 13, no. 8, pp. 1646–1653, 2017.
- [24] M. Solar, K. Binder, and W. Paul, "Relaxation processes and glass transition of confined polymer melts: A molecular dynamics simulation of 1,4-polybutadiene between graphite walls," *The Journal of Chemical Physics*, vol. 146, no. 20, p. 203308, 2017.
- [25] K. A. Smith, M. Vladkov, and J.-L. Barrat, "Polymer melt near a solid surface: a molecular dynamics study of chain conformations and desorption dynamics," *Macromolecules*, vol. 38, pp. 571–580, Jan 2005.
- [26] M. Vogel, "Rotational and conformational dynamics of a model polymer melt at solid interfaces," *Macromolecules*, vol. 42, no. 24, pp. 9498–9505, 2009.
- [27] A. Karatrantos, R. J. Composto, K. I. Winey, and N. Clarke, "Structure and conformations of polymer/swcnt nanocomposites," *Macromolecules*, vol. 44, no. 24, pp. 9830–9838, 2011.
- [28] Y. Li, M. Kröger, and W. K. Liu, "Nanoparticle effect on the dynamics of polymer chains and their entanglement network," *Physical Review Letters*, vol. 109, no. 11, p. 118001, 2012.
- [29] D. Brown, P. Mele, S. Marceau, and N. Albérola, "A molecular dynamics study of a model nanoparticle embedded in a polymer matrix," *Macromolecules*, vol. 36, no. 4, pp. 1395–1406, 2003.

- [30] Y. Termonia, "Monte-carlo modeling of dense polymer melts near nanoparticles," *Polymer*, vol. 50, no. 4, pp. 1062–1066, 2009.
- [31] G. G. Vogiatzis and D. N. Theodorou, "Structure of polymer layers grafted to nanoparticles in silica–polystyrene nanocomposites," *Macromolecules*, vol. 46, no. 11, pp. 4670–4683, 2013.
- [32] S. E. Harton, S. K. Kumar, H. Yang, T. Koga, K. Hicks, H. Lee, J. Mijovic, M. Liu, R. S. Vallery, and D. W. Gidley, "Immobilized polymer layers on spherical nanoparticles," *Macromolecules*, vol. 43, no. 7, pp. 3415–3421, 2010.
- [33] A. Tuteja, P. M. Duxbury, and M. E. Mackay, "Polymer chain swelling induced by dispersed nanoparticles," *Phys. Rev. Lett.*, vol. 100, p. 077801, Feb 2008.
- [34] S. Ok, M. Steinhart, A. Şerbescu, C. Franz, F. Vaca Chávez, and K. Saalwächter, "Confinement effects on chain dynamics and local chain order in entangled polymer melts," *Macromolecules*, vol. 43, no. 10, pp. 4429–4434, 2010. PMID: 20502536.
- [35] M. Hofmann, A. Herrmann, S. Ok, C. Franz, D. Kruk, K. Saalwächter, M. Steinhart, and E. A. Rössler, "Polymer dynamics of polybutadiene in nanoscopic confinement as revealed by field cycling ^1H NMR," *Macromolecules*, vol. 44, no. 11, pp. 4017–4021, 2011.
- [36] K. Shin, S. Obukhov, J.-T. Chen, J. Huh, Y. Hwang, S. Mok, P. Dobriyal, P. Thiyagarajan, and T. P. Russell, "Enhanced mobility of confined polymers," *Nature Materials*, vol. 6, pp. 961–965, Dec 2007.
- [37] L. Noirez, C. Stillings, J.-F. Bardeau, M. Steinhart, S. Schlitt, J. H. Wendorff, and G. Pépy, "What happens to polymer chains confined in rigid cylindrical inorganic (aao) nanopores," *Macromolecules*, vol. 46, no. 12, pp. 4932–4936, 2013.
- [38] A. Kusmin, S. Gruener, A. Henschel, O. Holderer, J. Allgaier, D. Richter, and P. Huber, "Evidence of a sticky boundary layer in nanochannels: A neutron spin echo study of n-hexatriacontane and poly(ethylene oxide) confined in porous silicon," *The Journal of Physical Chemistry Letters*, vol. 1, no. 20, pp. 3116–3121, 2010.

- [39] W.-S. Tung, R. J. Composto, R. A. Riggleman, and K. I. Winey, "Local polymer dynamics and diffusion in cylindrical nanoconfinement," *Macromolecules*, vol. 48, no. 7, pp. 2324–2332, 2015.
- [40] K. Lagrené, J.-M. Zanotti, M. Daoud, B. Farago, and P. Judeinstein, "Large-scale dynamics of a single polymer chain under severe confinement," *Phys. Rev. E*, vol. 81, p. 060801, Jun 2010.
- [41] J. Martín, M. Krutyeva, M. Monkenbusch, A. Arbe, J. Allgaier, A. Radulescu, P. Falus, J. Maiz, C. Mijangos, J. Colmenero, and D. Richter, "Direct observation of confined single chain dynamics by neutron scattering," *Phys. Rev. Lett.*, vol. 104, p. 197801, May 2010.
- [42] M. Krutyeva, A. Wischniewski, M. Monkenbusch, L. Willner, J. Maiz, C. Mijangos, A. Arbe, J. Colmenero, A. Radulescu, O. Holderer, M. Ohl, and D. Richter, "Effect of nanoconfinement on polymer dynamics: Surface layers and interphases," *Phys. Rev. Lett.*, vol. 110, p. 108303, Mar 2013.
- [43] M. Solar, L. Yelash, P. Virnau, K. Binder, and W. Paul, "Polymer dynamics in a polymer-solid interphase: Molecular dynamics simulations of 1,4-polybutadiene at a graphite surface," *Soft Materials*, vol. 12, no. sup1, pp. S80–S89, 2014.
- [44] M. Solar and W. Paul, "Dielectric α -relaxation of 1,4-polybutadiene confined between graphite walls," *The European Physical Journal E*, vol. 38, p. 37, May 2015.
- [45] L. Yelash, P. Virnau, K. Binder, and W. Paul, "Slow process in confined polymer melts: Layer exchange dynamics at a polymer solid interface," *Phys. Rev. E*, vol. 82, p. 050801, Nov 2010.
- [46] R. Khare, J. J. de Pablo, and A. Yethiraj, "Rheology of confined polymer melts," *Macromolecules*, vol. 29, no. 24, pp. 7910–7918, 1996.
- [47] I. G. Elliott, D. E. Mulder, P. T. Träskelin, J. R. Ell, T. E. Patten, T. L. Kuhl, and R. Faller, "Confined polymer systems: synergies between simulations and neutron scattering experiments," *Soft Matter*, vol. 5, pp. 4612–4622, 2009.

- [48] T. Aoyagi, J.-i. Takimoto, and M. Doi, "Molecular dynamics study of polymer melt confined between walls," *The Journal of Chemical Physics*, vol. 115, no. 1, pp. 552–559, 2001.
- [49] C. Franz, F. Lange, Y. Golitsyn, B. Hartmann-Azanza, M. Steinhart, M. Krutyeva, and K. Saalwächter, "Chain dynamics and segmental orientation in polymer melts confined to nanochannels," *Macromolecules*, vol. 49, no. 1, pp. 244–256, 2016.
- [50] J. F. Pressly, R. A. Riggleman, and K. I. Winey, "Polymer diffusion is fastest at intermediate levels of cylindrical confinement," *Macromolecules*, vol. 51, no. 23, pp. 9789–9797, 2018.
- [51] J. F. Pressly, R. A. Riggleman, and K. I. Winey, "Increased polymer diffusivity in thin-film confinement," *Macromolecules*, vol. 52, no. 16, pp. 6116–6125, 2019.
- [52] A. Silberberg, "Distribution of conformations and chain ends near the surface of a melt of linear flexible macromolecules," *Journal of Colloid and Interface Science*, vol. 90, pp. 86–91, 1982.
- [53] D. M. Sussman, W.-S. Tung, K. I. Winey, K. S. Schweizer, and R. A. Riggleman, "Entanglement reduction and anisotropic chain and primitive path conformations in polymer melts under thin film and cylindrical confinement," *Macromolecules*, vol. 47, pp. 6462–6472, 2014.
- [54] N.-K. Lee, J. Farago, H. Meyer, J. P. Wittmer, J. Baschnagel, S. P. Obukhov, and A. Johner, "Non-ideality of polymer melts confined to nanotubes," *EPL (Europhysics Letters)*, vol. 93, p. 48002, 2 2011.
- [55] F. Brochard and P. de Gennes, "Conformations de polymères fondus dans des pores très petits," *J. Physique Lett.*, vol. 40, pp. 399–401, 1979.
- [56] P. Huber, "Soft matter in hard confinement: phase transition thermodynamics, structure, texture, diffusion and flow in nanoporous media," *Journal of Physics: Condensed Matter*, vol. 27, p. 103102, feb 2015.
- [57] S. Y. Kim, H. W. Meyer, K. Saalwächter, and C. F. Zukoski, "Polymer dynamics in peg-silica nanocomposites: Effects of polymer molecular weight, temperature and solvent dilution," *Macromolecules*, vol. 45, no. 10, pp. 4225–4237, 2012.

- [58] M. Krutyeva, S. Pasini, M. Monkenbusch, J. Allgaier, J. Maiz, C. Mijangos, B. Hartmann-Azanza, M. Steinhart, N. Jalarvo, and D. Richter, "Polymer dynamics under cylindrical confinement featuring a locally repulsive surface: A quasielastic neutron scattering study," *The Journal of Chemical Physics*, vol. 146, no. 20, p. 203306, 2017.
- [59] R. Pérez Aparicio, A. Arbe, J. Colmenero, B. Frick, L. Willner, D. Richter, and L. J. Fetters, "Quasielastic neutron scattering study on the effect of blending on the dynamics of head-to-head poly(propylene) and poly(ethylene propylene)," *Macromolecules*, vol. 39, no. 3, pp. 1060–1072, 2006.
- [60] F. Varnik, J. Baschnagel, and K. Binder, "Reduction of the glass transition temperature in polymer films: A molecular-dynamics study," *Phys. Rev. E*, vol. 65, p. 021507, Jan 2002.
- [61] A. R. C. Baljon, S. Williams, N. K. Balabaev, F. Paans, D. Hudzinsky, and A. V. Lyulin, "Simulated glass transition in free-standing thin polystyrene films," *Journal of Polymer Science Part B: Polymer Physics*, vol. 48, no. 11, pp. 1160–1167, 2010.
- [62] A. Schönhals, H. Goering, C. Schick, B. Frick, and R. Zorn, "Polymers in nanoconfinement: What can be learned from relaxation and scattering experiments?," *Journal of Non-Crystalline Solids*, vol. 351, no. 33, pp. 2668–2677, 2005. Proceedings of 3rd International Conference on Broadband Dielectric Spectroscopy and its Applications.
- [63] A. Kusmin, S. Gruener, A. Henschel, N. de Souza, J. Allgaier, D. Richter, and P. Huber, "Polymer dynamics in nanochannels of porous silicon: A neutron spin echo study," *Macromolecules*, vol. 43, no. 19, pp. 8162–8169, 2010.
- [64] S. K. Kumar, B. C. Benicewicz, R. A. Vaia, and K. I. Winey, "50th anniversary perspective: Are polymer nanocomposites practical for applications?," *Macromolecules*, vol. 50, no. 3, pp. 714–731, 2017.
- [65] F. W. Starr, T. B. Schröder, and S. C. Glotzer, "Effects of a nanoscopic filler on the structure and dynamics of a simulated polymer melt and the relationship to ultrathin films," *Phys. Rev. E*, vol. 64, p. 021802, Jul 2001.

- [66] F. W. Starr, T. B. Schröder, and S. C. Glotzer, "Molecular dynamics simulation of a polymer melt with a nanoscopic particle," *Macromolecules*, vol. 35, no. 11, pp. 4481–4492, 2002.
- [67] C.-Y. Li, J.-H. Huang, H. Li, and M.-B. Luo, "Study on the interfacial properties of polymers around a nanoparticle," *RSC Adv.*, vol. 10, pp. 28075–28082, 2020.
- [68] C.-Y. Li, M.-B. Luo, H. Li, and W.-P. Cao, "Simulation study on the conformational properties of an adsorbed polymer on a nanoparticle," *Colloid and Polymer Science*, vol. 295, pp. 2251–2260, Dec 2017.
- [69] A. Y. Liu, H. Emamy, J. F. Douglas, and F. W. Starr, "Effects of chain length on the structure and dynamics of semidilute nanoparticle–polymer composites," *Macromolecules*, vol. 54, no. 7, pp. 3041–3051, 2021.
- [70] X.-W. Huang, Y. Peng, and J.-H. Huang, "Universal behaviors of polymer conformations in crowded environment," *Colloid and Polymer Science*, vol. 296, pp. 689–696, Apr 2018.
- [71] Y. Li, M. Kröger, and W. K. Liu, "Dynamic structure of unentangled polymer chains in the vicinity of non-attractive nanoparticles," *Soft Matter*, vol. 10, pp. 1723–1737, 2014.
- [72] V. Sorichetti, V. Hugouvieux, and W. Kob, "Structure and dynamics of a polymer–nanoparticle composite: Effect of nanoparticle size and volume fraction," *Macromolecules*, vol. 51, no. 14, pp. 5375–5391, 2018.
- [73] A. Nakatani, W. Chen, R. Schmidt, G. Gordon, and C. Han, "Chain dimensions in polysilicate-filled poly(dimethyl siloxane)," *Polymer*, vol. 42, no. 8, pp. 3713–3722, 2001.
- [74] M. K. Crawford, R. J. Smalley, G. Cohen, B. Hogan, B. Wood, S. K. Kumar, Y. B. Melnichenko, L. He, W. Guise, and B. Hammouda, "Chain conformation in polymer nanocomposites with uniformly dispersed nanoparticles," *Phys. Rev. Lett.*, vol. 110, p. 196001, May 2013.
- [75] M. Füllbrandt, P. J. Purohit, and A. Schönhals, "Combined ftir and dielectric investigation of poly(vinyl acetate) adsorbed on silica particles," *Macromolecules*, vol. 46, no. 11, pp. 4626–4632, 2013.

- [76] B. Carroll, S. Cheng, and A. P. Sokolov, "Analyzing the interfacial layer properties in polymer nanocomposites by broadband dielectric spectroscopy," *Macromolecules*, vol. 50, no. 16, pp. 6149–6163, 2017.
- [77] S. Gong, Q. Chen, J. F. Moll, S. K. Kumar, and R. H. Colby, "Segmental dynamics of polymer melts with spherical nanoparticles," *ACS Macro Letters*, vol. 3, no. 8, pp. 773–777, 2014.
- [78] A. P. Holt, P. J. Griffin, V. Bocharova, A. L. Agapov, A. E. Imel, M. D. Dadmun, J. R. Sangoro, and A. P. Sokolov, "Dynamics at the polymer/nanoparticle interface in poly(2-vinylpyridine)/silica nanocomposites," *Macromolecules*, vol. 47, no. 5, pp. 1837–1843, 2014.
- [79] S. M. Oh, M. Abbasi, T. J. Shin, K. Saalwächter, and S. Y. Kim, "Initial solvent-driven nonequilibrium effect on structure, properties, and dynamics of polymer nanocomposites," *Phys. Rev. Lett.*, vol. 123, p. 167801, Oct 2019.
- [80] C. B. Roth and J. R. Dutcher, "Glass transition and chain mobility in thin polymer films," *Journal of Electroanalytical Chemistry*, vol. 584, no. 1, pp. 13–22, 2005. International Symposium on Material Processing for Nanostructured Devices 2003.
- [81] J. L. Keddie, R. A. L. Jones, and R. A. Cory, "Size-dependent depression of the glass transition temperature in polymer films," *Europhysics Letters (EPL)*, vol. 27, pp. 59–64, jul 1994.
- [82] J. L. Keddie, R. A. L. Jones, and R. A. Cory, "Interface and surface effects on the glass-transition temperature in thin polymer films," *Faraday Discuss.*, vol. 98, pp. 219–230, 1994.
- [83] R. D. Priestley, C. J. Ellison, L. J. Broadbelt, and J. M. Torkelson, "Structural relaxation of polymer glasses at surfaces, interfaces, and in between," *Science*, vol. 309, no. 5733, pp. 456–459, 2005.
- [84] J. E. Pye and C. B. Roth, "Two simultaneous mechanisms causing glass transition temperature reductions in high molecular weight freestanding polymer films as measured by transmission ellipsometry," *Phys. Rev. Lett.*, vol. 107, p. 235701, Nov 2011.

- [85] O. Bäumchen, J. D. McGraw, J. A. Forrest, and K. Dalnoki-Veress, "Reduced glass transition temperatures in thin polymer films: Surface effect or artifact?," *Phys. Rev. Lett.*, vol. 109, p. 055701, Aug 2012.
- [86] V. M. Boucher, D. Cangialosi, H. Yin, A. Schönhals, A. Alegría, and J. Colmenero, " T_g depression and invariant segmental dynamics in polystyrene thin films," *Soft Matter*, vol. 8, pp. 5119–5122, 2012.
- [87] S. Peter, H. Meyer, J. Baschnagel, and R. Seemann, "Slow dynamics and glass transition in simulated free-standing polymer films: a possible relation between global and local glass transition temperatures," *Journal of Physics: Condensed Matter*, vol. 19, p. 205119, apr 2007.
- [88] F. Varnik, J. Baschnagel, and K. Binder, "Static and dynamic properties of supercooled thin polymer films," *The European Physical Journal E*, vol. 8, pp. 175–192, May 2002.
- [89] G. Vernadsky, "Rise of science in russia 1700-1917," *The Russian Review*, vol. 28, no. 1, pp. 37–52, 1969.
- [90] J. Mark, *Polymer Data Handbook*. Oxford University Press, 1999.
- [91] G. D. Smith, W. Paul, M. Monkenbusch, L. Willner, D. Richter, X. H. Qiu, and M. D. Ediger, "Molecular dynamics of a 1,4-polybutadiene melt. comparison of experiment and simulation," *Macromolecules*, vol. 32, no. 26, pp. 8857–8865, 1999.
- [92] G. D. Smith, O. Borodin, D. Bedrov, W. Paul, X. Qiu, and M. D. Ediger, " ^{13}C NMR spin-lattice relaxation and conformational dynamics in a 1,4-polybutadiene melt," *Macromolecules*, vol. 34, no. 15, pp. 5192–5199, 2001.
- [93] H. P. Hsieh, R. R. Bhave, and H. L. Fleming, "Microporous alumina membranes," *Journal of Membrane Science*, vol. 39, pp. 221–241, 1988.
- [94] J. A. McCammon, B. R. Gelin, and M. Karplus, "Dynamics of folded proteins," *Nature*, vol. 267, pp. 585–590, Jun 1977.
- [95] W. G. Hoover, "Canonical dynamics: Equilibrium phase-space distributions," *Phys. Rev. A*, vol. 31, pp. 1695–1697, Mar 1985.

- [96] S. Nosé, "A unified formulation of the constant temperature molecular dynamics methods," *The Journal of Chemical Physics*, vol. 81, no. 1, pp. 511–519, 1984.
- [97] G. D. Smith and W. Paul, "United atom force field for molecular dynamics simulations of 1,4-polybutadiene based on quantum chemistry calculations on model molecules," *The Journal of Physical Chemistry A*, vol. 102, no. 7, pp. 1200–1208, 1998.
- [98] G. D. Smith, W. Paul, M. Monkenbusch, and D. Richter, "On the non-gaussianity of chain motion in unentangled polymer melts," *The Journal of Chemical Physics*, vol. 114, no. 9, pp. 4285–4288, 2001.
- [99] W. Paul, D. Bedrov, and G. D. Smith, "Glass transition in 1,4-polybutadiene: Mode-coupling theory analysis of molecular dynamics simulations using a chemically realistic model," *Phys. Rev. E*, vol. 74, p. 021501, Aug 2006.
- [100] W. Paul and G. D. Smith, "Structure and dynamics of amorphous polymers: computer simulations compared to experiment and theory," *Reports on Progress in Physics*, vol. 67, pp. 1117–1185, 6 2004.
- [101] C. Chen, P. Depa, V. G. Sakai, J. K. Maranas, J. W. Lynn, I. Peral, and J. R. Copley, "A comparison of united atom, explicit atom, and coarse-grained simulation models for poly (ethylene oxide)," *The Journal of chemical physics*, vol. 124, no. 23, p. 234901, 2006.
- [102] P. J. Flory, "Foundations of rotational isomeric state theory and general methods for generating configurational averages," *Macromolecules*, vol. 7, no. 3, pp. 381–392, 1974.
- [103] J. E. Jones and S. Chapman, "On the determination of molecular fields. —ii. from the equation of state of a gas," *Proceedings of the Royal Society of London. Series A, Containing Papers of a Mathematical and Physical Character*, vol. 106, pp. 463–477, Oct 1924.
- [104] H. Berendsen, D. van der Spoel, and R. van Drunen, "Gromacs: A message-passing parallel molecular dynamics implementation," *Computer Physics Communications*, vol. 91, no. 1, pp. 43–56, 1995.

- [105] D. Van Der Spoel, E. Lindahl, B. Hess, G. Groenhof, A. E. Mark, and H. J. C. Berendsen, "Gromacs: Fast, flexible, and free," *Journal of Computational Chemistry*, vol. 26, no. 16, pp. 1701–1718, 2005.
- [106] B. Hess, C. Kutzner, D. van der Spoel, and E. Lindahl, "Gromacs 4: Algorithms for highly efficient, load-balanced, and scalable molecular simulation," *Journal of Chemical Theory and Computation*, vol. 4, no. 3, pp. 435–447, 2008. PMID: 26620784.
- [107] G. D. Smith, O. Borodin, and W. Paul, "A molecular-dynamics simulation study of dielectric relaxation in a 1,4-polybutadiene melt," *The Journal of Chemical Physics*, vol. 117, no. 22, pp. 10350–10359, 2002.
- [108] T. Gkourmpis and G. R. Mitchell, "Three dimensional picture of the local structure of 1,4-polybutadiene from a complete atomistic model and neutron scattering data," *Macromolecules*, vol. 44, pp. 3140–3148, 2011.
- [109] F. Demydiuk, M. Solar, H. Meyer, O. Benzerara, W. Paul, and J. Baschnagel, "Role of torsional potential in chain conformation, thermodynamics, and glass formation of simulated polybutadiene melts," *Journal of Chemical Physics*, vol. 156, 6 2022.
- [110] P. de Sainte Claire, K. C. Hass, W. F. Schneider, and W. L. Hase, "Simulations of hydrocarbon adsorption and subsequent water penetration on an aluminum oxide surface," *The Journal of Chemical Physics*, vol. 106, no. 17, pp. 7331–7342, 1997.
- [111] C. Li and P. Choi, "Molecular dynamics study of the adsorption behavior of normal alkanes on a relaxed α -al₂o₃ (0001) surface," *The Journal of Physical Chemistry C*, vol. 111, no. 4, pp. 1747–1753, 2007.
- [112] L. Tannoury, M. Solar, and W. Paul, "Structure and dynamics of a 1,4-polybutadiene melt in an alumina nanopore: A molecular dynamics simulation," *The Journal of Chemical Physics*, vol. 157, no. 12, p. 124901, 2022.
- [113] M. Solar, E. U. Mapesa, F. Kremer, K. Binder, and W. Paul, "The dielectric α -relaxation in polymer films: A comparison between experiments and atomistic simulations," *EPL (Europhysics Letters)*, vol. 104, p. 66004, dec 2013.

- [114] L. J. Fetters, D. J. Lohse, D. Richter, T. A. Witten, and A. Zirkel, "Connection between polymer molecular weight, density, chain dimensions, and melt viscoelastic properties," *Macromolecules*, vol. 27, no. 17, pp. 4639–4647, 1994.
- [115] T. S. Gulmen and W. Thompson, "Model silica pores with controllable surface chemistry for molecular dynamics simulatinos," *MRS Proceedings*, vol. 899, pp. 0899–N06–05, 2005.
- [116] A. A. Milischuk and B. M. Ladanyi, "Structure and dynamics of water confined in silica nanopores," *The Journal of Chemical Physics*, vol. 135, no. 17, p. 174709, 2011.
- [117] A. des sciences (France) and C. national de la recherche scientifique (France), *Comptes rendus hebdomadaires des séances de l'Académie des sciences.*, vol. t.126:no.1-13 (1898). Paris :publiés avec le concours du Centre national de la recherche scientifique par MM. les secrétaires perpétuels :, 1898.
- [118] H. A. Lorentz, "Ueber die anwendung des satzes vom virial in der kinetischen theorie der gase," *Annalen der Physik*, vol. 248, no. 1, pp. 127–136, 1881.
- [119] M. D. Hanwell, D. E. Curtis, D. C. Lonie, T. Vandermeersch, E. Zurek, and G. R. Hutchison, "Avogadro: an advanced semantic chemical editor, visualization, and analysis platform," *Journal of Cheminformatics*, vol. 4, p. 17, Aug 2012.
- [120] J. Liu, Y. Wu, J. Shen, Y. Gao, L. Zhang, and D. Cao, "Polymer–nanoparticle interfacial behavior revisited: A molecular dynamics study," *Phys. Chem. Chem. Phys.*, vol. 13, pp. 13058–13069, 2011.
- [121] Schrödinger, LLC, "The PyMOL molecular graphics system, version 2.5." February 2022.
- [122] H. Arkin and W. Janke, "Gyration tensor based analysis of the shapes of polymer chains in an attractive spherical cage," *The Journal of Chemical Physics*, vol. 138, no. 5, p. 054904, 2013.
- [123] W. Kuhn and F. Griin, "Kolloi'd zeitschrift," 1942.
- [124] K. Šolc, "Shape of a random-flight chain," *The Journal of Chemical Physics*, vol. 55, no. 1, pp. 335–344, 1971.

- [125] M. Doi and H. Nakajima, "Theory of the shape relaxation of a rouse chain," *Chemical Physics*, vol. 6, no. 1, pp. 124–129, 1974.
- [126] S. Kar and M. L. Greenfield, "Sizes and shapes of simulated amorphous cis- and trans-1,4-polybutadiene," *Polymer*, vol. 62, pp. 129–138, 2015.
- [127] J.-M. Y. Carrillo and B. G. Sumpter, "Structure and dynamics of confined flexible and unentangled polymer melts in highly adsorbing cylindrical pores," *The Journal of Chemical Physics*, vol. 141, no. 7, p. 074904, 2014.
- [128] A.-C. Genix, V. Bocharova, A. Kisliuk, B. Carroll, S. Zhao, J. Oberdisse, and A. P. Sokolov, "Enhancing the mechanical properties of glassy nanocomposites by tuning polymer molecular weight," *ACS Applied Materials & Interfaces*, vol. 10, no. 39, pp. 33601–33610, 2018. PMID: 30203957.
- [129] Q. Chen, S. Gong, J. Moll, D. Zhao, S. K. Kumar, and R. H. Colby, "Mechanical reinforcement of polymer nanocomposites from percolation of a nanoparticle network," *ACS Macro Letters*, vol. 4, no. 4, pp. 398–402, 2015. PMID: 35596328.
- [130] S. Yang and P. Akcora, "Deformation of chemically heterogeneous interfacial layers of polymer nanocomposites," *ACS Macro Letters*, vol. 8, no. 12, pp. 1635–1641, 2019. PMID: 35619398.
- [131] H. Eslami, M. Rahimi, and F. Müller-Plathe, "Molecular dynamics simulation of a silica nanoparticle in oligomeric poly(methyl methacrylate): A model system for studying the interphase thickness in a polymer–nanocomposite via different properties," *Macromolecules*, vol. 46, no. 21, pp. 8680–8692, 2013.
- [132] A. Gooneie, "Local structural fingerprints of nanoparticle-bound polymer layers," *J. Phys. Chem. B*, vol. 125, pp. 937–949, 2021.
- [133] A. J. Power, H. Papananou, A. N. Rissanou, M. Labardi, K. Chrissopoulou, V. Harmandaris, and S. H. Anastasiadis, "Dynamics of polymer chains in poly(ethylene oxide)/silica nanocomposites via a combined computational and experimental approach," *The Journal of Physical Chemistry B*, vol. 126, pp. 7745–7760, 10 2022.
- [134] A. Moghimikheirabadi, M. Krö, A. V. Karatrantos, and B. Conformations, "Insights from modeling into structure, entanglements, and dynamics in

- attractive polymer nanocomposites," *Cite this: Soft Matter*, vol. 17, p. 6362, 2021.
- [135] J. Colmenero and A. Arbe, "Recent progress on polymer dynamics by neutron scattering: From simple polymers to complex materials," *Journal of Polymer Science Part B: Polymer Physics*, vol. 51, no. 2, pp. 87–113, 2013.
- [136] M. Krutyeva, A. Wischniewski, M. Monkenbusch, L. Willner, J. Maiz, C. Mijangos, A. Arbe, J. Colmenero, A. Radulescu, O. Holderer, M. Ohl, and D. Richter, "Effect of nanoconfinement on polymer dynamics: Surface layers and interphases," *Phys. Rev. Lett.*, vol. 110, p. 108303, Mar 2013.
- [137] N. Fatkullin, R. Kimmich, E. Fischer, C. Mattea, U. Beginn, and M. Kroutieva, "The confined-to-bulk dynamics transition of polymer melts in nanoscopic pores of solid matrices with varying pore diameter," *New Journal of Physics*, vol. 6, pp. 46–46, apr 2004.
- [138] P. E. Rouse, "A theory of the linear viscoelastic properties of dilute solutions of coiling polymers," *The Journal of Chemical Physics*, vol. 21, no. 7, pp. 1272–1280, 1953.
- [139] A. Papon, H. Montes, M. Hanafi, F. Lequeux, L. Guy, and K. Saalwächter, "Glass-transition temperature gradient in nanocomposites: Evidence from nuclear magnetic resonance and differential scanning calorimetry," *Phys. Rev. Lett.*, vol. 108, p. 65702, 2 2012.
- [140] J.-L. Barrat, J. Baschnagel, and A. Lyulin, "Molecular dynamics simulations of glassy polymers," *Soft Matter*, vol. 6, pp. 3430–3446, 2010.
- [141] S. Peter, H. Meyer, and J. Baschnagel, "Thickness-dependent reduction of the glass-transition temperature in thin polymer films with a free surface," *Journal of Polymer Science Part B: Polymer Physics*, vol. 44, no. 20, pp. 2951–2967, 2006.
- [142] P. Scheidler, W. Kob, and K. Binder, "The relaxation dynamics of a supercooled liquid confined by rough walls," *The Journal of Physical Chemistry B*, vol. 108, no. 21, pp. 6673–6686, 2004.
- [143] F. Varnik, J. Baschnagel, K. Binder, and M. Mareschal, "Confinement effects on the slow dynamics of a supercooled polymer melt: Rouse modes and

- the incoherent scattering function," *The European Physical Journal E*, vol. 12, pp. 167–171, Sep 2003.
- [144] P. Scheidler, W. Kob, and K. Binder, "Cooperative motion and growing length scales in supercooled confined liquids," *Europhysics Letters (EPL)*, vol. 59, pp. 701–707, sep 2002.
- [145] R. Zorn, D. Richter, B. Frick, and B. Farago, "Neutron scattering experiments on the glass transition of polymers," *Physica A: Statistical Mechanics and its Applications*, vol. 201, no. 1, pp. 52–66, 1993.
- [146] C. Bennemann, J. Baschnagel, and W. Paul, "Molecular-dynamics simulation of a glassy polymer melt: Incoherent scattering function," *The European Physical Journal B - Condensed Matter and Complex Systems*, vol. 10, pp. 323–334, May 1999.
- [147] W. Paul, D. Y. Yoon, and G. D. Smith, "An optimized united atom model for simulations of polymethylene melts," *The Journal of Chemical Physics*, vol. 103, no. 4, pp. 1702–1709, 1995.
- [148] G. D. Smith, D. Y. Yoon, W. Zhu, and M. D. Ediger, "Comparison of equilibrium and dynamic properties of polymethylene melts of n-c44h90 chains from simulations and experiments," *Macromolecules*, vol. 27, no. 20, pp. 5563–5569, 1994.
- [149] W. Paul, G. D. Smith, and D. Y. Yoon, "Static and dynamic properties of a n-c100h202 melt from molecular dynamics simulations," *Macromolecules*, vol. 30, no. 25, pp. 7772–7780, 1997.
- [150] N. E. Moe and M. D. Ediger, "Computer simulations of polyisoprene local dynamics in vacuum, solution, and the melt: Are conformational transitions always important?," *Macromolecules*, vol. 29, no. 16, pp. 5484–5492, 1996.
- [151] D. J. Gisser, S. Glowinkowski, and M. D. Ediger, "Local dynamics of polyisoprene in toluene," *Macromolecules*, vol. 24, no. 15, pp. 4270–4277, 1991.
- [152] A. Ghanbari, T. V. M. Nodoro, F. Leroy, M. Rahimi, M. C. Böhm, and F. Müller-Plathe, "Interphase structure in silica–polystyrene nanocomposites: A coarse-grained molecular dynamics study," *Macromolecules*, vol. 45, no. 1, pp. 572–584, 2012.

- [153] T. V. M. Nodoro, E. Voyiatzis, A. Ghanbari, D. N. Theodorou, M. C. Böhm, and F. Müller-Plathe, "Interface of grafted and ungrafted silica nanoparticles with a polystyrene matrix: Atomistic molecular dynamics simulations," *Macromolecules*, vol. 44, no. 7, pp. 2316–2327, 2011.
- [154] A. L. Frischknecht, E. S. McGarrity, and M. E. Mackay, "Expanded chain dimensions in polymer melts with nanoparticle fillers," *The Journal of Chemical Physics*, vol. 132, no. 20, p. 204901, 2010.
- [155] L. Khounlavong and V. Ganesan, "Influence of interfacial layers upon the barrier properties of polymer nanocomposites," *The Journal of Chemical Physics*, vol. 130, no. 10, p. 104901, 2009.
- [156] V. Ganesan, L. Khounlavong, and V. Pryamitsyn, "Equilibrium characteristics of semiflexible polymer solutions near probe particles," *Phys. Rev. E*, vol. 78, p. 051804, Nov 2008.
- [157] G. J. Fleer, A. M. Skvortsov, and R. Tuinier, "Mean-field equation for the depletion thickness," *Macromolecules*, vol. 36, no. 20, pp. 7857–7872, 2003.
- [158] A. Kloczkowski, M. Sharaf, and J. Mark, "Computer simulations on filled elastomeric materials," *Chemical Engineering Science*, vol. 49, no. 17, pp. 2889–2897, 1994.
- [159] M. Vacatello, "Monte carlo simulations of polymer melts filled with solid nanoparticles," *Macromolecules*, vol. 34, no. 6, pp. 1946–1952, 2001.
- [160] G. D. Smith, D. Bedrov, L. Li, and O. Bytner, "A molecular dynamics simulation study of the viscoelastic properties of polymer nanocomposites," *The Journal of Chemical Physics*, vol. 117, no. 20, pp. 9478–9489, 2002.
- [161] J. S. Smith, D. Bedrov, and G. D. Smith, "A molecular dynamics simulation study of nanoparticle interactions in a model polymer-nanoparticle composite," *Composites Science and Technology*, vol. 63, no. 11, pp. 1599–1605, 2003. Modeling and Characterization of Nanostructured Materials.
- [162] M. Vacatello, "Predicting the molecular arrangements in polymer-based nanocomposites," *Macromolecular Theory and Simulations*, vol. 12, no. 1, pp. 86–91, 2003.

- [163] P. J. Dionne, R. Ozisik, and C. R. Picu, "Structure and dynamics of polyethylene nanocomposites," *Macromolecules*, vol. 38, no. 22, pp. 9351–9358, 2005.
- [164] M. Goswami and B. G. Sumpter, "Effect of polymer-filler interaction strengths on the thermodynamic and dynamic properties of polymer nanocomposites," *The Journal of Chemical Physics*, vol. 130, no. 13, p. 134910, 2009.
- [165] M. Ozmusul and R. Picu, "Structure of polymers in the vicinity of convex impenetrable surfaces: the athermal case," *Polymer*, vol. 43, no. 17, pp. 4657–4665, 2002.
- [166] M. Vacatello, "Chain dimensions in filled polymers: An intriguing problem," *Macromolecules*, vol. 35, no. 21, pp. 8191–8193, 2002.
- [167] M. Goswami and B. G. Sumpter, "Anomalous chain diffusion in polymer nanocomposites for varying polymer-filler interaction strengths," *Phys. Rev. E*, vol. 81, p. 041801, Apr 2010.
- [168] L. Khounlavong, V. Pryamitsyn, and V. Ganesan, "Many-body interactions and coarse-grained simulations of structure of nanoparticle-polymer melt mixtures," *The Journal of Chemical Physics*, vol. 133, no. 14, p. 144904, 2010.
- [169] D. Brown, V. Marcadon, P. Mélé, and N. D. Albérola, "Effect of filler particle size on the properties of model nanocomposites," *Macromolecules*, vol. 41, no. 4, pp. 1499–1511, 2008.
- [170] D. Barbier, D. Brown, A.-C. Grillet, and S. Neyertz, "Interface between end-functionalized peo oligomers and a silica nanoparticle studied by molecular dynamics simulations," *Macromolecules*, vol. 37, no. 12, pp. 4695–4710, 2004.
- [171] A. N. Rissanou, H. Papananou, V. S. Petrakis, M. Doxastakis, K. S. Andrikopoulos, G. A. Voyiatzis, K. Chrissopoulou, V. Harmandaris, and S. H. Anastasiadis, "Structural and conformational properties of poly(ethylene oxide)/silica nanocomposites: Effect of confinement," *Macromolecules*, vol. 50, no. 16, pp. 6273–6284, 2017.
- [172] C. S. Ezquerro, J. M. G. Aznar, and M. Lasपालas, "Prediction of the structure and mechanical properties of polycaprolactone–silica nanocomposites and

the interphase region by molecular dynamics simulations: the effect of pegylation," *Soft Matter*, vol. 18, pp. 2800–2813, 2022.

- [173] A. Karatrantos, N. Clarke, R. J. Composto, and K. I. Winey, "Polymer conformations in polymer nanocomposites containing spherical nanoparticles," *Soft Matter*, vol. 11, pp. 382–388, 2015.

Curriculum Vitae

Personal Information:

Name: Lama Tannoury
Date of Birth: 21.10.1992
Place of Birth: Beirut, Lebanon
Citizenship: Lebanese

Education:

2018 - 2021 Member of the *International School for Functional Polymers - AGRIPOLY*

since 2018 **Ph.D studies**, Martin Luther University Halle-Wittenberg

- Title: Structure and dynamics of a 1,4-Polybutadiene melt in confinement: A molecular dynamics study
- Supervisor: Prof. Dr. Wolfgang Paul

2013 - 2017 **Master of Science in Physics**, American University of Beirut

- Title: Dynamic origins of entropic force: thermodynamic theory vs. molecular dynamics simulations
- Supervisor: Prof. Dr. Leonid Klushin

2010 - 2013 **Bachelor of Science in Physics**, American University of Beirut

Signature: _____

Date: _____

List of Publications

- **L. Tannoury**, M. Solar, and W. Paul, "Structure and dynamics of a 1,4-polybutadiene melt in an alumina nanopore: A molecular dynamics simulation," *The Journal of Chemical Physics*, vol. 157, no. 12, p. 124901, 2022

Acknowledgments

I extend my gratitude to all those who contributed to the realization of this thesis and provided valuable support along the way.

I am deeply grateful to my advisor, Prof. Dr. Wolfgang Paul for his invaluable guidance and mentorship throughout my PhD journey. He played a pivotal role in shaping me into an independent scientist, fostering critical thinking and developing a strong research foundation. I am thankful for his support in granting me the autonomy to find my own way to successfully complete this thesis.

I would also like to express my sincere appreciation to Dr. Mathieu Solar for his assistance throughout my PhD. During the early stages of my program he generously dedicated his time to teach me the essentials. His ongoing willingness and support in answering questions and providing the necessary data has been immensely helpful.

Within the Paul group, I had several insightful discussions with Dr. Viktor Ivanov, which have enriched my knowledge on the topic. Dr. Timur Shakirov was also a primary source of information and advice. Timur, our group and office guru, is a source of knowledge and new ideas. The contributions of both have encouraged me to examine my research from multiple perspectives.

Recognition is also due to my other current office mates, Christian Lauer, Michael Beyer, Kai-Hendrik Henk, Evgeniia Filimonova (honorary office resident) and Philipp Tesch for their patience and tolerance amidst my numerous discussions and rants. It has been a privilege to share this space with you, and I am grateful for the support and camaraderie we have built.

I would also like to thank the remaining and former members of the group, Prof. Steffen Trimper, Dr. Benno Werlich, Dr. Eunsang Lee, Dr. Arne Böker and Dr. Jeanette Köppe who warmly welcomed me to the group and to Halle upon my arrival.

My project was funded by the International School for Functional Polymers -

AGRIPOLY. A special recognition goes to the coordinators who have diligently taken care of the administrative aspects.

Finally, I would like to dedicate a heartfelt acknowledgement to my parents, family and friends without whom this endeavor would have been impossible. To my mother and father, thank you for everything you have done and continue to do. Your unconditional love has been a constant source of comfort and I am grateful for the countless sacrifices you have made to ensure my education and well-being.

I would like to thank my sister Hiba and my brother-in-law Tarek for their unwavering support. More than ten years ago, you were my inspiration to embark on this enriching journey. For that I am forever grateful.

To my sister Sana and brother-in-law Jeff, thank you for everything you've done. For the long video calls, morning coffees, long political conversations and for being there whenever I needed support. Sana, thank you for always being honest and for sharing the load.

To my friends, in Halle and all around the world, you may not know it but you have provided me with the strength to overcome obstacles. In no particular order and I am sorry if I miss anyone, Kafa Alameh, Amine Wahada, Maxime Phalempin, Ali Rida Khalifeh, Alessandro Fumarola, James Taylor, Annika Schwarz, Felix Teske, Rodrique Badr, Kshitij Shinde, Farina Genzen, and Karo Zawistowska. Over the course of the past five years, my life has undergone substantial transformations, and each one of you has played an important role in helping me navigate them. Thank you all for being there and for creating some of my fondest memories. You have made this journey all the more meaningful.

Declaration

I hereby declare that the work presented in this thesis is my own and has been written under the supervision of, Prof. Dr. Wolfgang Paul. I did not use any outside support except for the quoted literature and other sources mentioned in the manuscript.

Signature

